UNIVERSITY OF CALIFORNIA,
IRVINE

Photochemistry of limonene secondary organic aerosol studied with chemical ionization mass spectrometry

DISSERTATION

submitted in partial satisfaction of the requirements
for the degree of

DOCTOR OF PHILOSOPHY

in Chemistry

by

Xiang Pan

Dissertation Committee:
Professor Sergey A. Nizkorodov, Chair
Professor Vladimir Mandelshtam
Professor Craig Martens

2009

This page intentionally left blank

The dissertation of Xiang Pan
is approved and is acceptable in quality and form for
publication on microfilm and in digital formats:

_____

_____

_____
Committee Chair

University of California, Irvine
2009

DEDICATION

To my parents, Donggen Pan and Meifang Guo,
who always support me.

Table of Contents

List of Figures

List of Tables

ACKNOWLEDGEMENTS

I would like to thank my graduate advisor, Professor Sergey Nizkorodov. Without his support and guidance, I couldn't finish my PhD research. He made me understand that scientific research needs not only knowledge and ideas, but also courage and patience. I want to thank Dr. Ao Lin, who gave a lot of very useful help on research in my first several years in this lab. I also want to thank Dr. Joelle Underwood and Dr. Jiahua Xing, who gave me a lot of help during and after our cooperation. All help from previous group members including Dr. Jiho Park, Dr. Tony Gomez, Dr. Ahmad Alshawa, Dr. Maggie Walser, Dr. Steve Mang and present group members including David Bones, Chris Harmon, Adam Bateman and Tran Nguyen is appreciated.

My friends Yun Dong, Lian Wang, Xiang Luo, Hua Zhang encouraged me during frustrating research time. A special thank to my friend Ling Lin and her family. Ling is always next to me in the past several years no matter what happens.

Thank my parents, Meifang Guo and Donggen Pan, for their endless support. They could not pursue their own dreams when they were young because of the bad economic situation. But they never gave it up and passed it to me. Although they never know anything about chemistry or physics, they do know that people can do nothing without science knowledge. Without their support and encouragement, I could not achieve anything.

CURRICULUM VITAE

Contact information

Email address: xpan@uci.edu

EDUCATION

Current: Ph.D. in Chemistry, University of California, Irvine (UCI), 2009. (GPA: 3.9/4.0)

B.S. Department of Chemical Physics, University of Science and Technology of China (USTC), June 2002. (GPA: 3.5/4.0)

Conference Posters and Presentations

1. X. Pan, JH Xing, J.S. Underwood and S.A Nizkorodov *"Photodegradation of SOA prepared by oxidation of d-limonene by ozone and NO_3"*. 2008 AGU Meeting, Dec 2008 (poster)
2. X. Pan**,** JH Xing, and S.A. Nizkorodov "*CIMS study of photochemistry of SOA generated from limonene oxidation*". 2008 AirUCI Meeting, February 2008 (contributed talk)
3. X. Pan, J.S. Underwood, and S.A. Nizkorodov "*Probing the photochemistry of monoterpene-derived secondary organic aerosols with chemical ionization mass spectrometry*". 26th Annual AAAR Conference, September 2007 (talk)
4. X. Pan, J.S. Underwood, T. Do, and S.A. Nizkorodov "*Mass-spectrometric characterization of products of photochemical aging of terpene SOA particles*". 24th Informal Symposium on Kinetics and Photochemical Processes in the

Atmosphere, February 2007 (poster)

5. X. Pan, A. Lin, J.S. Underwood, and S.A. Nizkorodov "*Ozonolysis of organic particles studied with chemical ionization aerosol particle mass spectrometry*". 24th Annual AAAR Conference, October 2005 (contributed talk)
6. X. Pan, A. Lin, and S.A. Nizkorodov "*Effect of particle size on rates of photodegradation of atmospheric toxins adsorbed on soot aerosol particles*". UC Toxic Substances Research & Teaching Program Conference, April 2005 (poster)

Publications

1. X. Pan, JH Xing, J.S. Underwood, S.A. Mang and S.A. Nizkorodov,"*Photodegradation of Secondary Organic Aerosol Generated from Limonene Oxidation by Ozone Studied with Chemical Ionization Mass Spectrometry*". (2009) accepted by Atm. Chem. Phys..
2. JH Xing, X. Pan, S.A. Mang, and S.A. Nizkorodov,"*Photodegradation of Secondary Organic Aerosol Generated from Limonene Oxidation by NO_3*". (2009) in preparation.
3. S.A. Mang, M.L. Walser, X. Pan, JH. Xing, A.P. Bateman, J.S. Underwood, A.L. Gomez, J. Park, and S.A. Nizkorodov "*Photochemistry of secondary organic aerosol formed from oxidation of monoterpenes*".In "Atmospheric Aerosols: Characterization, Chemistry, and Modeling (ACS Symposium Series)"Valsaraj, K. T., Kommalapati, R. R., Eds., (2009) published.

ABSTRACT OF THE DISSERTATION

Photochemistry of limonene secondary organic aerosol studied with chemical ionization mass spectrometry

By

Xiang Pan

Doctor of Philosophy in Chemistry

University of California, Irvine, 2009

Professor Sergey A. Nizkorodov, Chair

Limonene is one of the most abundant monoterpenes in the atmosphere. Limonene easily reacts with gas-phase oxidants in air such as NO_3, ozone and OH. Secondary organic aerosol (SOA) is formed when low vapor pressure products condense into particles. Chemicals in SOA particles can undergo further reactions with oxidants and with solar radiation that significantly change SOA composition over the course of several days. The goal of this work was to characterize radiation induced reaction in SOA.

To perform experiments, we have designed and constructed an Atmospheric Pressure Chemical Ionization Mass Spectrometer (APCIMS) coupled to a photochemical cell containing SOA samples. In APCIMS, $(H_2O)_nH_3O^+$ clusters are generated in a ^{63}Ni source and react with gaseous organic analytes. Most organic chemicals are not fragmented by the ionization process.

We have focused our attention on limonene SOA prepared in two different ways. The first type of SOA is produced by oxidation of limonene by ozone; and the second type of SOA is formed by the NO_3-induced oxidation of limonene. They model the SOA formed under daytime and nighttime conditions, respectively. Ozone initiated oxidation is the most important chemical sink for limonene both indoors, where it is used for cleaning purposes, and outdoors. Terpenes are primarily oxidized by reactions with NO_3 at night time.

We generated limonene SOA under different ozone and limonene concentrations. The resulting SOA samples were exposed to wavelength-tunable radiation in the UV-Visible range between 270 nm and 630 nm. The results show that the photodegradation rates strongly depend on radiation wavelengths. Gas phase photodegradation products such as acetone, formaldehyde, acetaldehyde, and acetic acid were shown to have different production rates for SOA formed in different concentration conditions. Even for SOA prepared under the lowest concentrations, the SOA photodegradation was efficient. The conclusion is that exposure of SOA to solar radiation causes significant chemical aging in SOA species.

Chapter I

General introduction to atmospheric aerosols

1.1 Atmospheric Aerosols

Aerosols are solid or liquid particles suspended in gases. The typical particle size in an atmospheric aerosol is from 0.002 μm to 100 μm. Aerosol particles can remain suspended from several seconds to one year depending on their size and meteorological conditions [1].

Important properties of aerosol include particle size and average chemical composition. Roughly speaking, the particle size could be divided into four ranges including PM_{10} (Particulate Matter, ≤10 μm in aerodynamic diameter), $PM_{2.5}$ (≤2.5 μm in aerodynamic diameter), PM_1 (≤1 μm in aerodynamic diameter) and ultrafine (≤100 nm in aerodynamic diameter) as adopted by the Environmental Protection Agency 1997 [1]. Here aerodyniamic diameter means the diameter of a standard-density (1 g/cm^3) sphere having the same gravitational settling velocity as the particle being measured [2]. The size of particles affects their atmospheric lifetime, health effects, optical properties, and cloud nucleation potential [3]. The chemical composition of aerosols can be very different depending on the sources. It can be divided into inorganic compounds including crustal materials, black carbon, sulfates, and nitrates and organic compounds, which usually account for 20% to 50% mass of ambient aerosol [4]. The sources of aerosol particles can be anthropogenic or biogenic. For example, sulfate particles usually are anthropogenic, while biogenic Secondary Organic Aerosol (SOA) particles are formed from monoterpene emissions.

1.2 Aerosols and climate change

Increasing attention is paid to the global climate change by scientists and also the public. Although there are arguments about the minor details, there is no doubt that human activities are affecting and changing the global and regional climates. Land use change and energy dependence on fossil fuel result in increasing greenhouse gas emission rate, which pushes the global temperature up. According to the Intergovernmental Panel on Climate Change (IPCC), the average temperature is now 0.75 degree higher than it was in 1850 globally; eleven out of twelve hottest years between 1850 and 2005 happened in 1990's and 2000's. IPCC predicts that 0.2 degree per decade temperature rising rate would happen in the next two decade globally. The regional climate is also changing. The temperature change is not unique globally; some areas are affected by the climate change more than others. The 2007 IPCC report states that "widespread changes in precipitation amounts, ocean salinity, wind patterns and aspects of extreme weather including droughts, heavy precipitation, heat waves and the intensity of tropical cyclones" are happening (IPCC report, 2007).

In the meanwhile, climate change is also changing almost every aspect of our life, including transportation, food, drinking water and health. More frequent nature disasters force people to move. IPCC suggested there would be 150 million environmental refugees in 2050.

The importance of climate change requires better understanding of the roles of different trace species in atmosphere. The most famous "stars" in the eyes of the public are greenhouse gases including CO_2, CH_4 and N_2O, which convert infrared radiation energy into thermal energy [3]. 184 countries have ratified Kyoto Protocol, which aims at

achieving stabilization of greenhouse gas concentrations in the atmosphere (United Nations Framework Convention on Climate Change, UNFCCC). The effect of the other trace species in atmosphere receives less attention from the public. But that does not mean they are not important in climate change.

Radiative forcing, which is used to quantify this effect, is defined as follows: "The radiative forcing of the surface-troposphere system due to the perturbation in or the introduction of an agent (say, a change in greenhouse gas concentrations) is the change in net (down minus up) irradiance (solar plus long-wave; in Wm^{-2}) at the tropopause after allowing for stratospheric temperatures to readjust to radiative equilibrium, but with surface and tropospheric temperatures and state held fixed at the unperturbed values" (IPCC report, 2007). In the following figure, the major components having positive radiative forcing are greenhouse gases including CO_2, CH_4, N_2O, halocarbons and O_3; land use change and aerosol generally make negative contribute to the radiative forcing.

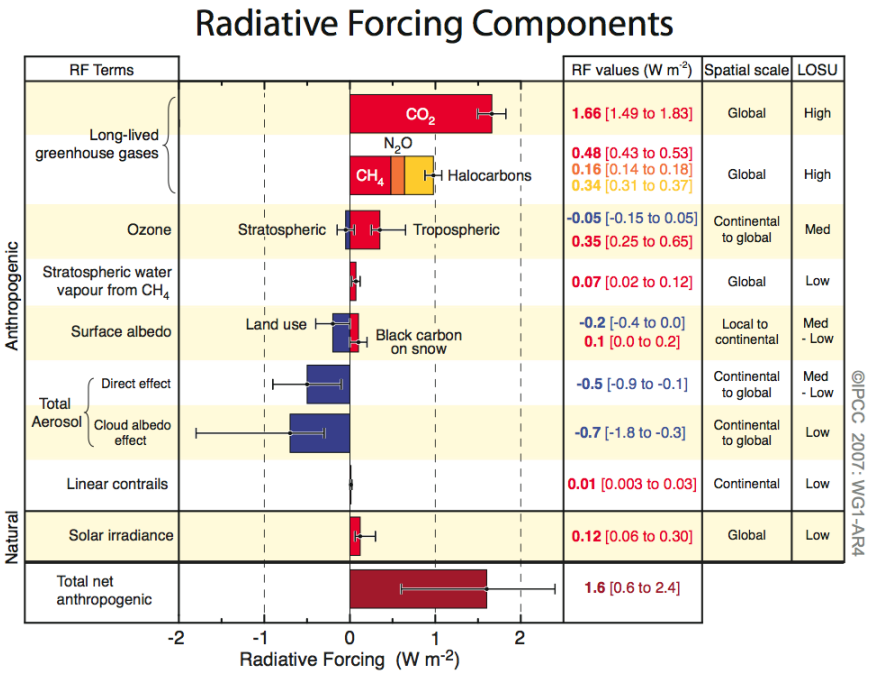

Figure 1.1 Radiative forcing components estimated by IPCC (IPCC report, 2007)

The uncertainty in the effects of aerosols on climate is much larger than it is for the greenhouse gases. Since the effect of aerosol on radiative forcing is comparable to the effect of greenhouse gases and it is difficult to quantify the contribution of aerosol due to its relative short and irregular lifetime [5], more understanding of aerosol chemistry and physics is necessary.

The ways aerosols affect climate change are different from what greenhouse gases do. The effects of aerosol on climate change can be direct and indirect (IPCC report, 2007). Atmospheric aerosol can modify the radiative balance of atmosphere by scattering or absorbing solar radiation. Except for black carbon particles, most organic aerosol particles cool the earth's atmosphere; this effect is especially important for fine particles whose sizes are close to visible light wavelengths. Atmospheric aerosol can also indirectly modify the microphysical properties of clouds, such as the cloud droplet lifetime, number concentration, and water content. Several different indirect effect have been investigated (IPCC, 2001) [6-8].

Aerosol particles are relatively short-lived in the troposphere, so the effect is the greatest in the daytime and during the summer. The aerosol particles' optical properties depend on particle size and composition. Furthermore, many aerosol phenomena depend on aerosol concentrations nonlinearly. For example, aerosol interactions with clouds follow nonlinear relation with aerosol concentration, size and composition. All of these factors make aerosol effects rather complicated [9].

1.3 Aerosols and human health

Aerosol science history is closely related to air pollution history. In 1273, coal

burning was prohibited in London because of serious particulate air pollution and foul smell [2]. Modern research provides better understanding of the relationship between aerosol and human health. Mortality was associated with the levels of fine particles in selected six cities in the US [10]. The PM_{10} level increase of 10 μg m^3 caused an estimated 0.4% increase in the rate of death in six western European cities [11] and an estimated 0.5% increase of the rate of death in twenty cities in the US [12]. Diseases, particularly respiratory diseases, were found to correlate with levels of particulate air pollution. Fore example, 4%, 6% and 8% increased risk of all-cause, cardiopulmonary and lung cancer mortality, respectively, were associated with PM_{10} increase of per 10 $\mu g/m^3$ [13]. Fine particles cause roughly 50,000 premature deaths each year in the United States alone [14]. Despite this alarming statistics, scientists still do not know what chemicals in PM are responsible for its detrimental health effects.

The damage caused by the aerosol particles depends on the chemical composition and the area of the respiratory system where they deposit. There is strong evidence showing that $PM_{2.5}$ are more hazardous than PM_{10} (World Health Organization (WHO) report, 2003). Large particles are stopped in the noses, but small particles can go into the lungs and stay there for a varying time depending on physicochemical properties, their location within the lung and the type of clearance mechanism involved [1]. Those particles have effects on human's respiratory system [15]. The smallest particles can even penetrate into blood vessels and cause cardiovascular diseases. Research on rats showed that ultra-fine particles (<100 nm) can even translocate to liver and brain [16]. Chemical composition of particles is also important for particle health effects. PM components such as certain metals and certain aromatic organic compounds were shown to contribute to

the health effects of PM (WHO report, 2003).

1.4 Aerosol formation from biogenic Volatile Organic Compounds (VOC)

Aerosols are classified into primary aerosol and secondary aerosol depending on the mechanism of their introduction in the atmosphere. Primary aerosols are injected into atmosphere directly from some processes on land and water. For example, black soot particles are formed in combustion and are emitted into atmosphere directly. Secondary aerosols are formed from gas-to-liquid or gas-to-solid phase changes in atmosphere. The major chemical processes supplying condensable chemicals for secondary organic aerosol (SOA) in the troposphere include oxidation of volatile organic chemicals by O_3, OH and NO_3.

In some areas, particles may contain organic matter in high percentage. For example, organic matter accounts for 20 to 50% of total fine aerosol mass at continental midlatitudes [17] and could reach to 90% in tropical forest areas in both dry and wet seasons [18]. SOA productions rate is estimated to be comparable to that of biogenic and anthropogenic sulfate aerosol [18]. That means a large portion of atmospheric aerosols come from volatile organic compounds (VOC) in atmosphere.

Biogenic VOC emissions are an order of magnitude greater than anthropogenic VOC emissions on a global scale [19]. The total global emission of biogenic VOC was estimated to be 1150 Tg carbon per year [20] and the total global emission of anthropogenic VOC has been estimated less than 100Tg carbon per year [21].

The major source of biogenic hydrocarbons is vegetation. For example, trees contribute 98% of total natural non-methane VOC in North America [22, 23]. The most

important type of non-methane VOC is the terpene family, which includes isoprene (C_5H_8), monoterpenes ($C_{10}H_{16}$), and sesquiterpenes ($C_{15}H_{24}$). This family accounts for over 50% of biogenic VOC emissions [20]. Organic components in aerosols greatly affect the formation, growth, and removal of ambient aerosols (IPCC report, 2007).

1.5 Aerosol aging

During the time particles stay in the air, aerosols are continuously modified in the atmosphere by chemical reactions with O_3, O_2, NO_3, halogen atoms and OH [24-26]. This modification is frequently referred to as "aging". Photochemistry is also an important aging mechanism for organic aerosols [27, 28]. Aerosol aging could modify the physicochemical properties of aerosol dramatically. Aging-induced changes in hygroscopicity of aerosol, the particle size, chemical composition, volatility, and optical properties likely affect the impacts of aerosols on climate and health. For example, SOA particles formed by ozonolysis of common biogenic compounds including limonene, alpha-pinene become less active as cloud condensation nuclei (CCN) as they age [29].

1.6 Thesis Objectives

The main objective of this work is to study of the mechanism of photochemical aging of organic aerosol particles formed by oxidation of terpene, particularly limonene, by oxidants such as ozone and NO_3. Chapter II is the literature review of previous limonene SOA research. Chapter III introduces the photochemistry of O_3 derived limonene SOA and Chapter IV introduces the photochemistry of NO_3 derived limonene

SOA. In order to achieve the objective of this work, we had to build an instrument based on chemical ionization mass spectrometry. With this instrument, gas phase products from photodegradation of aerosol can be sensitively detected. The development of this instrument is introduced in Chapter V and the understanding of the kinetics in the home-build ionizer is introduced Chapter VI.

Chapter II

Literature review

2.1 Terpenes and monoterpenes

As mentioned in Chapter I, organic matter accounts for 20% to 50% mass in fine aerosol particles in atmosphere. In the Amazon Basin, the organic mass fraction can be as high as 80% [17]. The source of SOA, which accounts for up to 90% of organic particles in atmosphere, is volatile organic compounds (VOC). On a global scale, the largest sources of VOC are biogenic in nature. Biogenic VOC include various alkanes, alkenes, carbonyls, alcohols, esters, ethers and acids. Once emitted, these VOCs are oxidized into oxygenated VOCs on a time scale ranging from minutes to months. A certain fraction of oxidation products has sufficiently low volatility to condense into SOA. Isoprenoids including isoprene and terpenes are the most prominent compounds among the biogenic VOCs. The total non-methane VOC flux is about 84 Tg of carbon in North America, of which 35% is isoprene and 25% are 19 other terpenoid compounds [23].

Terpenes can be viewed as molecules "constructed" from the C_5H_8 isoprene units. There are several different kinds of terpenoids including monoterpenes ($C_{10}H_{16}$), sesquiterpenes ($C_{15}H_{24}$), and their numerous oxygenated derivatives. More than 5000 terpenes have been identified structurally [30]. Terpene reactions may contribute up to 50% of the total organic aerosol in Northern Europe [31].

Monoterpenes ($C_{10}H_{16}$) account for 11% of biogenic hydrocarbons on a global scale [20]. They can be linear molecules such as myrcene, trans-beta-ocimene or cyclic molecules such as alpha pinene, beta pinene or limonene. Figure 2.1 shows the fourteen dominant monoterpenes found in over 160 tree species [30]. Monoterpenes are major fraction of 'terpenic oils' or 'essential oils'. Unlike isoprene, monoterpenes can be stored in secretory organs of plants such as conifers, lamiaceae, apiaceae *et al.* The emission rates of monoterpenes are different for different plants. For example, the monoterpene emission of California sagebrush is 47 $\mu g \bullet g^{-1} hr^{-1}$, while big sagebrush which is in same family has an emission rate of less than 0.2 $\mu g \bullet g^{-1} hr^{-1}$ at standard conditions [32, 33]. Temperature is the most important factor affecting the emission; the emission rates of monoterpene from slash pines increase with temperature exponentially [34, 35]. Sunlight also affects monoterpene emission from plants [36, 37]. The monoterpene concentrations in atmosphere vary from ppt to several ppb [20, 38].

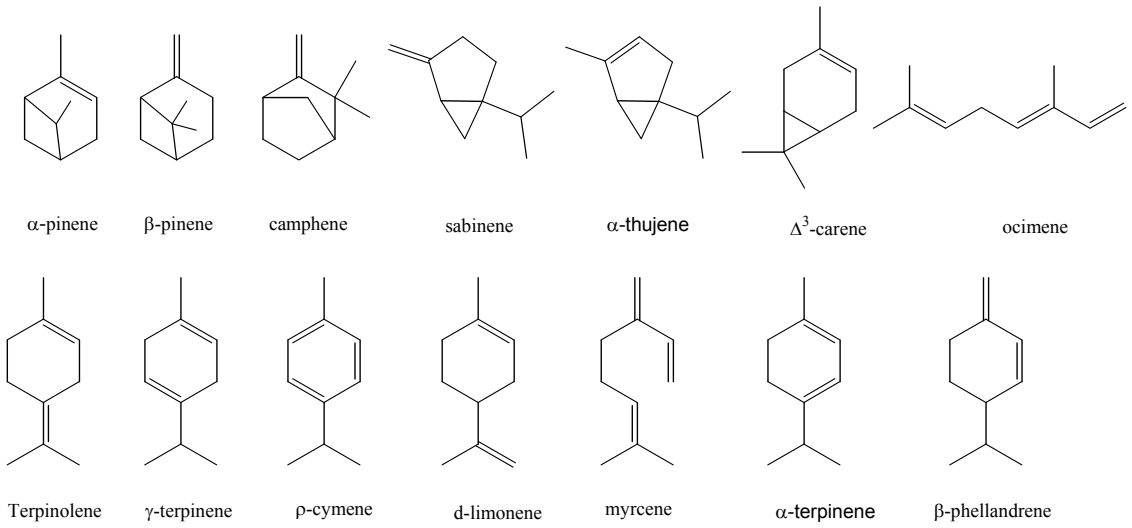

Figure 2.1 Fourteen dominant monoterpenes

One important question for atmospheric chemistry research is the fate of emitted VOCs in atmosphere. The processes could be physical such like wet and dry deposition or chemical such like photolysis and reaction with oxidants. The most important sink for monoterpenes is to oxidize into SOA precursors. As early as 1960, Went observed a blue haze on distant mountains and suggested that it was formed by particles from oxidation by O_3 of terpenes emitted from pine trees [39]. Monoterpenes can react with O_3, OH or NO_3 and produce semi-volatile or non-volatile products, which condense and form SOA.

The reaction rate constants between monoterpene and oxidants were investigated by several research groups. The lifetimes might be very different for different monoterpenes due to very different reaction rate constants and oxidant concentrations in atmosphere. For example, the life time of α-pinene for reaction with NO_3 is only 11 minutes, but it is 4.6 hours for reaction with O_3 under typical NO_3 and O_3 concentrations [40]. However there is more monoterpene in the atmosphere during the day time, making both processes important.

The mechanism of reaction between monoterpene and oxidants is similar to the mechanisms of reaction between alkene and oxidants, but it is more complex [41]. Two general reaction mechanisms are involved in the oxidation. The first one is the addition to C=C bonds by OH radicals, NO_3 radicals and O_3; the second mechanism is the H-abstraction from C-H bonds by OH and NO_3 radicals. The former one usually dominates over the latter one for OH and NO_3 radicals; O_3 only reacts via the addition mechanism [40]. The addition of O_3 to C=C bonds leads to the formation of a carbonyl and a biradical (Criegee intermediate) by a well known mechanism named Criegee

mechanism after Professor Rudolf Criegee, who had worked on ozonolysis mechanism since 1949 [42]. The produced radicals can have further reactions: (a) they can stabilize into thermalized Criegee intermediate by collision; (b) dialkyl- and syn-monoalkyl-substituted Criegee intermediates can isomerize to a hydroperoxide followed by decomposition to OH radical plus a alkyl radical; (c) rearrange to an ester followed by decomposition [27, 40, 41]. The addition to C=C bonds by OH and NO_3 leads to the formation of hydroxyl- or nitro-substituted alkyl radicals respectively [40, 41]. The formed β-hydroxyalkyl or β-nitratoalkyl radicals from OH reaction or NO_3 radicals can have three possible reaction pathways, including decomposition, isomerisation and reaction with oxygen molecule. For radicals derived from monoterpenes, the most important pathway is isomerization [40, 41].

The oxidation of monoterpenes usually forms semivolatile or nonvolatile products, which can form aerosols by condensation onto pre-existing particles. The aerosol yield is defined as the fraction of the reacted organics (ROG) mass that is eventually converted into aerosol. $Y=m_{aerosol}/m_{ROG}$. [43]. The aerosol yields are different for different monoterpenes. For example, at room temperature and low humidity conditions, α-pinene SOA mass yield is 41-67% [43] [44]; β-pinene SOA mass yield is 17-32% [43] [44]. SOA from reactions of monoterpenes with ozone, the aerosol yield generally decrease in the following order: polyunsaturated monoterpenes such as limonene > cyclic monounsaturated monoterpenes such as α-pinene > acyclic monoterpenes such as ocimene [43]. The UV radiation level, temperature, presence of seed particles, and elevated relative humidity strongly affect the aerosol yields [45-48].

The aging of monoterpene SOA is caused by further oxidation by OH radical, NO_3 radical, O_3 and UV light. The aging processes can have several generations, which also affect the final SOA aerosol yield. In the first generation, monoterpene SOA yields range from 0.03 to 1.0 [49]. With further reaction, carbon-carbon bond cleavage will produce lighter, more volatile products, but oxygenation will tend to produce polar, less volatile products and increase the absolute aerosol mass [49]. The effective yield of aerosol of aerosol products from monoterpenes will approach unity within a few generations [49, 50].

Although O_3, H_2O, O_2 can absorb part of the solar light, sunlight above 290 nm still reaches the earth surface [3]. The existence of sunlight especially UV light (< 400 nm) makes photochemistry an important player in atmosphere chemistry. Photochemical processes induced by UV radiation affect SOA formation and aging [27, 46, 51, 52].

2.2 Limonene

Limonene ($C_{10}H_{16}$) is one of the most abundant monoterpenes in the atmosphere [30]. Biogenic sources produce only R-enantiomer of limonene or D-limonene (CAS 5989-27-5); it will be referred as simply “limonene” in this thesis. The molecular weight of limonene is 136.24 g/mole; the melting point is -95.2 °C and the boiling point is 176 °C. Limonene is the major component in pine and citrus oils [53].

The major biogenic sources of limonene are conifers and crops. Limonene accounts for 1-10% of most pinus species monoterpene composition. In abies,

liquidambar, picea and tsuga, it goes up to 10% to 30% of monoterpene composition [30]. 30% of emission from Australia eucalyptus is limonene [54]. Limonene accounts for 10% to 20% of total terpene emissions in the northeastern US, lake states region, Rocky Mountains and Alaska [30]. Limonene represents one of the four highest terpenes (alpha-pinene, beta-pinene, sabinene, and limonene) emitted in North America [55]. These four terpenes accounts for 40%-80% of the overall global terpene emission excluding isoprene [56]. It was estimated that limonene accounts for 16.4% mass of overall monoterpene emissions [56]. The high potential to produce SOA from limonene makes it one of the most important biogenic monoterpenes. Limonene SOA accounts for up to 20% terpene SOA, although limonene emission is only 5% of terpene in some place depending on vegetative species distribution [31, 57].

Limonene is also an important compound in indoor chemistry. Most people spend greater than 90% of their time indoors [58]. It is estimated that exposure to air pollutants indoors may actually be higher than that from the outdoor exposure [59]. Limonene frequently exists in indoor environments because it is used to add orange fragrance to various cleaning products or used as a green solvent. It is released in the indoor air after cleaning carpets, countertops, and other surfaces with limonene-containing products. It also could come from wood flooring and furnishings [59, 60]. The limonene concentrations are 5-10 ppb in the indoor environments [53, 61]. In indoor environments, oxidants like O_3 exist at lower concentrations compared to the outdoor air but it is sufficient to effectively oxidize limonene and other terpenes. O_3 concentration could be 20% to 80% of outdoor O_3 concentration depending on ventilation rate [58]. The reaction between limonene and indoor ozone has been a focus of attention because it can generate

irritating products. The resulting aerosol from the indoor oxidation of limonene has potential health risk [62]. It was found that the mixture of limonene and ozone caused reduction of the respiratory rate of >30% in mouse bioassay, which is used to quantifies airway irritation and 230% increase of time of brake [53, 62]. Limonene also can be chemopreventive and therapeutic efficacy in rodents and reduce mammary carcinomas [63].

2.3 Limonene oxidation and limonene SOA

2.3.1 Oxidation rates of limonene by OH, NO_3 and O_3

The two double bonds in limonene can easily react with oxidants in atmosphere. The lifetime of gas phase limonene in atmosphere was estimated to be 40-80 minutes during daytime and 5-20 minutes at night under typical conditions [38]. The rate constants for the reactions of limonene with OH, NO_3 , and O_3 are 17.1×10^{-11} cm^3 $molecule^{-1}s^{-1}$, 1.22×10^{-11} cm^3 $molecule^{-1}s^{-1}$, and 2.1×10^{-16} cm^3 $molecule^{-1}s^{-1}$, respectively, at 296K and atmospheric pressure [43, 64]. The lifetimes of limonene for reaction with OH radical, O_3 and NO_3 are 49 minutes, 2 hours and 5 minutes under typical atmospheric conditions with [OH] = 2×10^6 molecule cm^{-3}, [O_3] = 7×10^{11} molecule cm^{-3}, [NO_3] = 2.5×10^8 molecule cm^{-3} [40]. The production rate of SOA from limonene is Rate = [limonene]/lifetime. Because limonene emissions are higher during the day, ozone oxidation usually dominates the SOA production rate.

2.3.2 O_3 oxidation

Ozone initiated oxidation is one of the most chemical important sinks for limonene both outdoors and indoors. Ozone concentration in troposphere varies from 20 ppb to several hundred ppb in extreme cases. The double bonds in limonene react with O_3 via Criegee mechanism. In the Criegee mechanism, ozone attacks the double bond and forms a very unstable intermediate, named primary ozonide (POZ) as shown in figure 2.2 below. It decomposes into a biradical (Criegee intermediate) and a carbonyl. The subsequent fate of the Criegee intermediate depends on its molecular structure and also on its environment [65]. But for the most part, Criegee intermediates are very reactive; they can undergo unimolecular reactions or react with other chemicals such as H_2O, aldehydes, ketones, alcohols, and others.

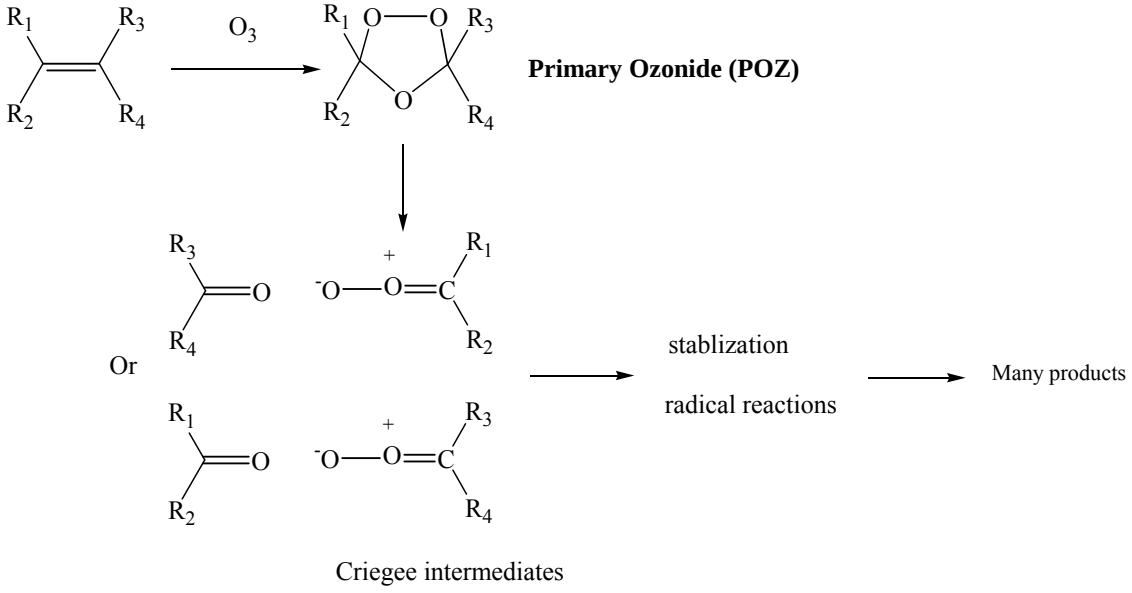

Figure 2.2 Ozonolysis of limonene by Criegee mechanism

The reported O_3+limonene reaction rate constant is 2.1×10^{-16} cm^3 $molecule^{-1}s^{-1}$ at 296K [64], 2.0×10^{-16} cm^3 $molecule^{-1}s^{-1}$ at 298K [43] or $2.95\times10^{-15}exp(-783/T)$ cm^3 $molecule^{-1}s^{-1}$ at other temperatures [66]. The difference between these rate constants is small (10%) at room temperature.

Gas-phase ozonolysis of limonene has been studied extensively to characterize the chemical composition of condensable and volatile products of limonene oxidation. In the initial attack by O_3, both of the internal double bond and the external double bond are reactive. The reaction probability ratio is 85:15 for internal double bond: external double bond [67]. The four Criegee intermediates (CIs) produced from the primary ozonides have further reactions. 35% of them form stable Criegee biradicals. The CIs formed from ozone oxidized internal double bond react with H_2O to form limonoaldehyde, which is the most dominant gas phase product [68]. Some other important products are listed in Figure 2.3.

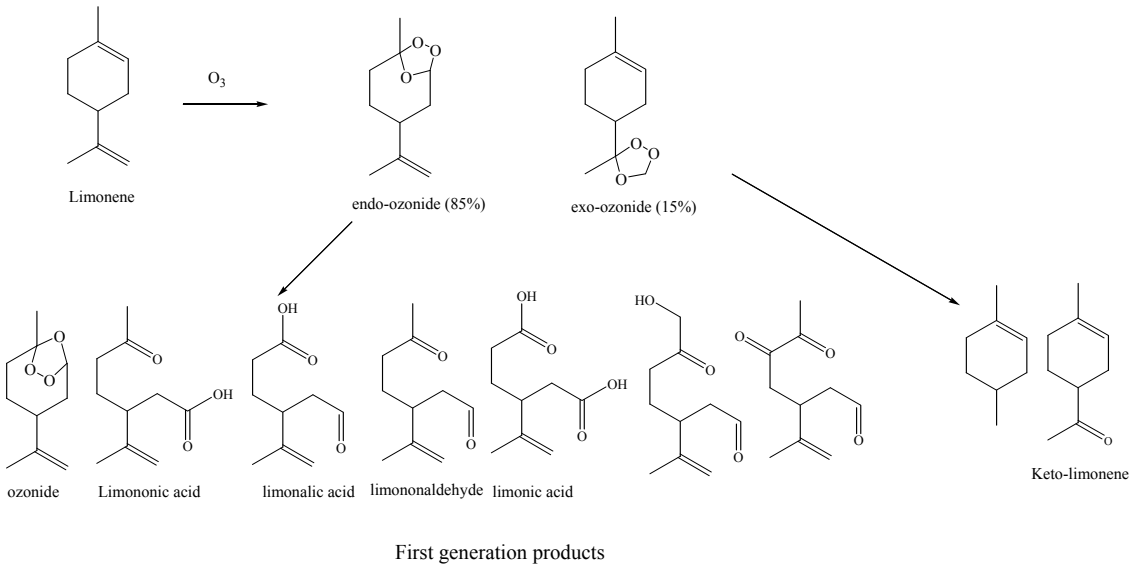

Figure 2.3 Known limonene ozonolysis products

All the products are the first generation products. They all have one more double bond which can be attacked by another O_3 or other oxidants and form the second generation products. For example, limononaldehyde react with ozone at a rate of $(8.3 \pm 2.2) \times 10^{-18}$ cm^3 $molecule^{-1}s^{-1}$ [41]. The second generation products can react still further and form third generation products. These reactions between different generations of ozonolysis products with oxidants result in a huge array of products [67, 69-78].

2.3.3 NO_3 radical reaction

The mechanism of the reaction between limonene and NO_3 has not been investigated extensively. The mechanism should be very similar to the general mechanism of the reactions between alkenes and NO_3. NO_3 radical favors the attack on the endocyclic double bond in limonene even more selectively than OH radical and ozone do [55]. Part of the possible reaction mechanism is shown in figure 2.4 which is modified from similar reaction mechanism in ref. 54. The major product of the reaction is endolim (shown in Figure 2.4). The endolim yield was reported in two separate studies as 28.8% [55] and 69% [79].

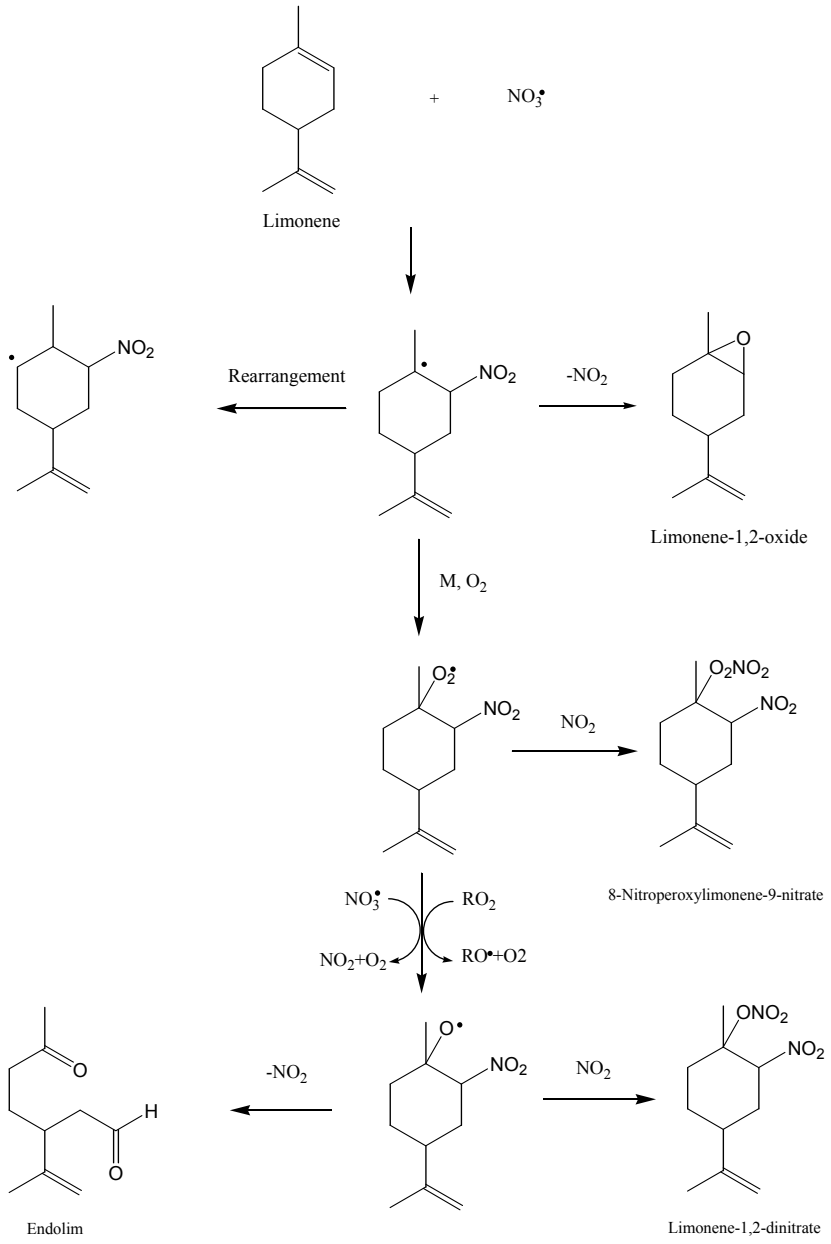

Figure 2.4 Possible mechanism of limonene reaction with NO_3 radical (adapted from Ref [55])

2.3.4 Photoaging of limonene SOA

Our group previously observed emission of multiple VOCs from limonene SOA exposed to UV radiation in the actinic region. We demonstrated that formaldehyde and

formic acid are produced by photolysis of exocyclic secondary ozonides derived from limonene [27]. The emission of CO, CH_4, small alkenes, alcohols, and carbonyls was attributed to Norrish photocleavage of various carbonyls in limonene SOA [52]. We measured the action spectra for the emission of CO and formic acid as a function of irradiation wavelength, and compared these spectra with the absorption spectrum of limonene SOA. Based on these observations, we concluded that carbonyl and peroxy functional groups in SOA are photodegraded on time scales that can be as short as several hours under realistic atmospheric conditions [52].

Chapter III

Photochemistry of O_3 derived limonene SOA

3.1 Introduction

In the lower atmosphere, O_3 is formed by reaction between O_2 and O atom which arises from the photodissociation of NO_2 [3]. The relatively high concentration of O_3 in atmosphere makes it one of the most important oxidants for VOCs both in daytime and at nighttime. The previous research on the reaction between O_3 and limonene was introduced in previous chapter. This chapter will introduce the photochemistry of limonene/O_3 SOA and discuss the SOA photochemistry research done in our lab.

3.2 Experimental

3.2.1 SOA sample preparation

SOA was generated by a dark reaction between limonene vapor and ozone in zero-air at room temperature and ambient pressure. Home-made Teflon FEP bags with black covers were used as reaction chambers. They were filled to a desired volume with dry air from Parker model 75-52 FTIR purge gas generator. Ozone was generated from ultrahigh purity (UHP) oxygen by a commercial ozone generator (Ozonetech OZ2SS) and added to the chamber until a desired concentration was reached. A home-build ozone photometer continuously measured the ozone concentration in the chamber. The reaction was initiated by a microsyringe injection of a small volume of liquid limonene via a

septum port in the chamber. Limonene quickly evaporated, and reacted with ozone in the gas-phase. Limonene was purchased from Acros Organics (97% stated purity) and used without additional purification.

In order to assess the effect of concentrations of limonene and ozone on the resulting SOA photochemistry, the initial concentrations were varied by three orders of magnitude. Typical conditions are presented in Table 1 for high (~300 ppm), intermediate (~1 ppm), and low (~0.1 ppm) initial ozone mixing ratios. To avoid cross-contamination, two separate chambers were used for low/intermediate and high concentration experiments. An SMPS (scanning mobility particle sizer) was used to monitor the particle formation in selected experiments.

Case	High	Intermediate	Low
Initial ozone mixing ratio (ppm)	300	1.0	0.10
Reactant added	L	L	1:19 L:cyclohexane
Volume added (μL)	5	1	2
Chamber volume (L)	220	360	360
Initial limonene mixing ratio (ppm)	3.4	0.41	0.021
Particles collected for (min)*	3	10	30
Flow through the filter (SLM)	2	1.5	2

Table 3.1 Three experimental conditions used for SOA preparation

Figure 3.1 below shows a typical time dependence of ozone and particle concentrations in the reaction chamber for the intermediate concentration case. Following the injection of 1 μL of limonene, the ozone mixing ratio decreased 50% in 10 minutes resulting in a prompt particle growth. The particle number concentration was 8×10^5 cm^{-3} and mean particle size was ~100 nm after 10 minutes of reaction. After one hour, the number concentration decreased to 3×10^5 cm^{-3} while the mean size of particles increased to ~220 nm suggesting that particles were coagulating. Particle collection typically

started a 30 minutes after the addition of limonene.

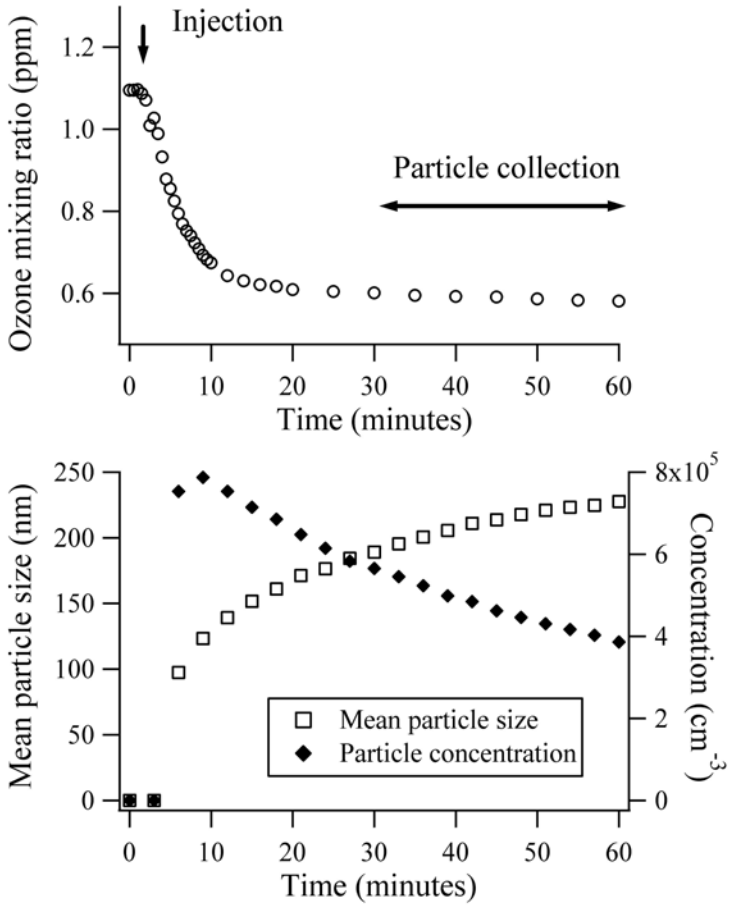

Figure 3.1 Ozone concentration and aerosol formation during limonene+ozone reaction

SOA material was collected on six identical quartz-fiber filters using a home-built six-way filter holder and an oil-free pump (GAST 1023). Explicit SMPS measurements showed that particles were collected with better than 95% efficiency. The collection time and pump flow rate were 3 min @ 2 SLM (standard liters per minute), 10 min @ 1.5 SLM, and 30 min @ 2 SLM for ozone concentrations of 300 pm, 1 ppm, and 0.1 ppm, respectively. The weight of collected SOA material was measured with Sartorius ME5-F filter balance with 1 μg readability and/or estimated from the SMPS data. Typically, each

filter contained about 10, 30, and 50 μg of SOA material for low, intermediate, and high concentration experiments, respectively. All filtered samples were stored under a flow of dry nitrogen in darkness, and used within 10 hours of their preparation.

Particles were also collected by impaction on 2.5 cm CaF_2 windows in order to record UV/vis absorption spectra of SOA material with Shimadzu UV-2450 dual-beam spectrophotometer. A relatively uniform film of SOA material was prepared by compressing the collected particles between two CaF_2 windows and gently heating them. Details of this procedure and representative absorption spectra of limonene SOA material were described by [52].

3.2.2 Experiment setup

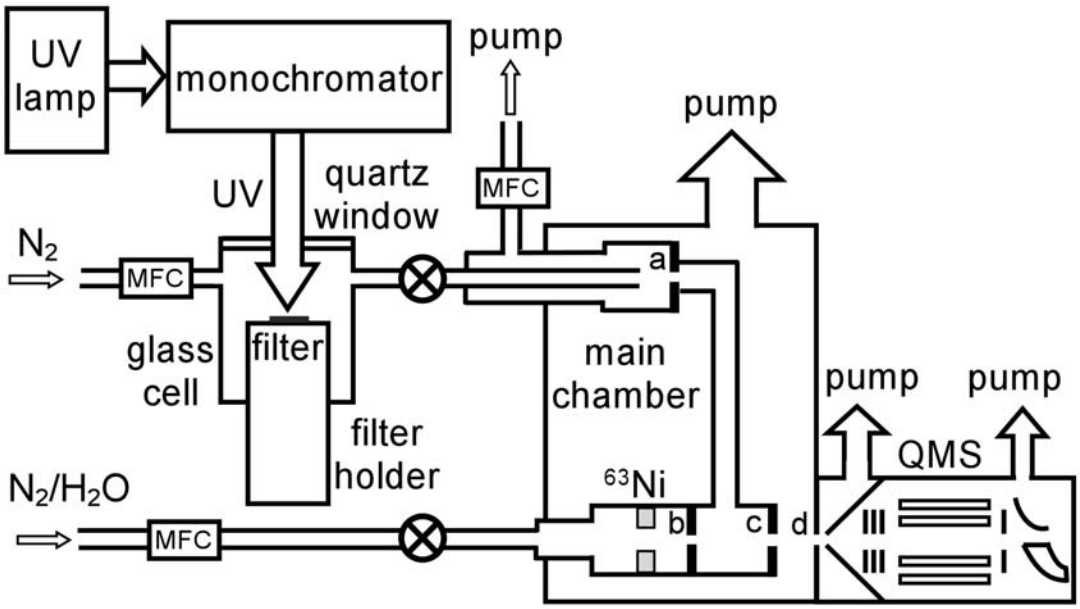

Figure 3.2 Experimental apparatus constructed for this study. A more detailed description of this instrument will be given in sections V and VI

Figure 3.2 shows a diagram of the experimental setup designed to measure the relative yields of gas-phase products formed in SOA photodegradation as a function of the irradiation wavelength (a more complete description of this instrument will be given in sections V and VI). A filter loaded with SOA was placed inside a 14 cm^3 glass flow cell equipped with a 2 cm quartz window. A combination of a 150W Xe-lamp (Oriel) and a 1/8-m monochromator (Spectra-Physics) was used to generate a desired wavelength of radiation from 270 nm to 650 nm. The slits of the monochromator were fully open resulting in ~10 nm wavelength resolution (FWHM). Quartz lens was used to collimate the radiation on the filter. The radiation power was measured with a calibrated power monitor (Coherent PS19Q) and ranged from 0.050-0.45 mW and 0.40-2.6 mW in high and low/intermediate concentration experiments, respectively

Gas-phase products of photolysis were detected by the CIMS apparatus shown in Fig. 3.2. UHP N_2 flow passed over the irradiated filter sample and entered 50 cm long, 0.06 cm ∅ stainless steal tube, which was concentrically inserted into 0.40 cm ∅ tube (symbol ∅ refers to the inner tube diameter). At the end of the outer tube, a small fraction of the flow exited through a 50 μm pinhole (labeled "a" in Fig. 3.2), while the excess flow was pumped away through a mass flow controller. For high and intermediate concentration experiments ($O_3 \geq 1$ ppm), the sample flow and pump flow were set to 200 sccm (standard cubic centimeters per minute) and 180 sccm, respectively, resulting in ~0.05 s travel from the SOA holder to pinhole "a". To increase the sensitivity in low concentration experiments (0.1 ppm ozone), the sample and pump flows were reduced to 50 and 30 sccm, respectively, resulting in sample residence time of 0.2 s. The pressure in the photolysis cell was kept at 700 Torr resulting in ~20 sccm flow through the pinhole.

The instrument was operated in a proton-transfer mode [80], using protonated water clusters $(H_2O)_nH^+$ as reagents. UHP N_2 carried trace amounts of H_2O vapor into a 1.0 cm ∅ stainless steel tube terminated with a 100 μm pinhole (labeled "b" in Fig. 3.2). The N_2 flow was 20-40 sccm and the pressure in the tube was typically in the range of 250-460 Torr. Protonated water clusters were generated by exposing the gas flow to β-particles emitted by a 15 mCi ^{63}Ni ring-source (Isotope Products Laboratories), which was mounted near the tube exit. The most abundant ions were $(H_2O)_4H^+$ and $(H_2O)_3H^+$, with some $(H_2O)_2H^+$ and $(H_2O)_5H^+$ also present. Free hydronium ion H_3O^+ was normally not observed. The ions passed through the 100 μm pinhole and entered the ionization volume, where the proton transfer reactions with analyte molecules took place.

The ion and sample flows were mixed together in a short cylindrical tube (6 cm long; 1.0 cm ∅) equipped with a 270 μm pinhole at the end (pinhole "c" in Fig. 3.2). Inside this ionization volume, protons transferred from water ions to analyte molecules with higher proton affinity (PA). The pressure in the tube was in the range of 40-80 Torr, and ion residence time was ~0.4 s. The resulting ions exited the pinhole into the main chamber of the CIMS instrument kept at 0.3-0.4 Torr by a mechanical pump/booster combination (Edwards Vacuum E2M80/EH500).

After traversing the main chamber for 2-5 mm, ions entered the second differentially pumped chamber through a 500 μm pinhole (labeled "d" in Fig. 3.2). The ions entered the third differentially pumped chamber containing an ABB Extrel quadrupole mass spectrometer (QMS) through a 2 mm conical skimmer. The skimmer, pinhole "c", and pinhole "d" were all concentrically aligned with respect to the entrance into an ABB Extrel axial molecular beam ionizer assembly mounted at the QMS entrance.

The ionizing current was turned off, and the ion source was merely used to transmit the ions into the QMS. The QMS had four 19 mm diameter rods driven at 1.2 MHz by a 300W power supply. The ions were detected in single ion counting mode with a conversion dynode multiplier and pulse amplifier. The QMS and its electronics were controlled by a computer using Merlin Automation software.

3.2.3 SOA photodegradation measurements

For each filter placed in the photolysis cell, several mass spectra were collected in the absence of irradiation in order to measure the background ion counts. After the UV radiation source was turned on, 15-45 additional mass spectra were collected. Each mass spectrum represented an average of 440 QMS microscans and took 2 min to acquire. The range was 10-400 *m/z* in order to include monomeric and dimeric products of limonene oxidation and their possible volatile photodegradation products. The mass resolution was ~1 *m/z*.

A separate SOA filter was used for each irradiation wavelength. With six identical filter samples, photodegradation at six irradiation wavelengths could be examined for a given SOA batch. One of the irradiation wavelengths was always 270 nm for normalization purposes. In order to minimize possible aging effects due to slow reactions between SOA constituents, we finished photolysis of all collected samples as quickly as possible. It usually took 5-10 hours to complete one set of filters, including loading the filters, recording the background mass-spectra, irradiating the filters until the intensity of photoproduct peaks reached a stable level, and purging the system in preparation for the next filter sample.

3.3 Results

3.3.1 CIMS spectra of SOA photodegradation products

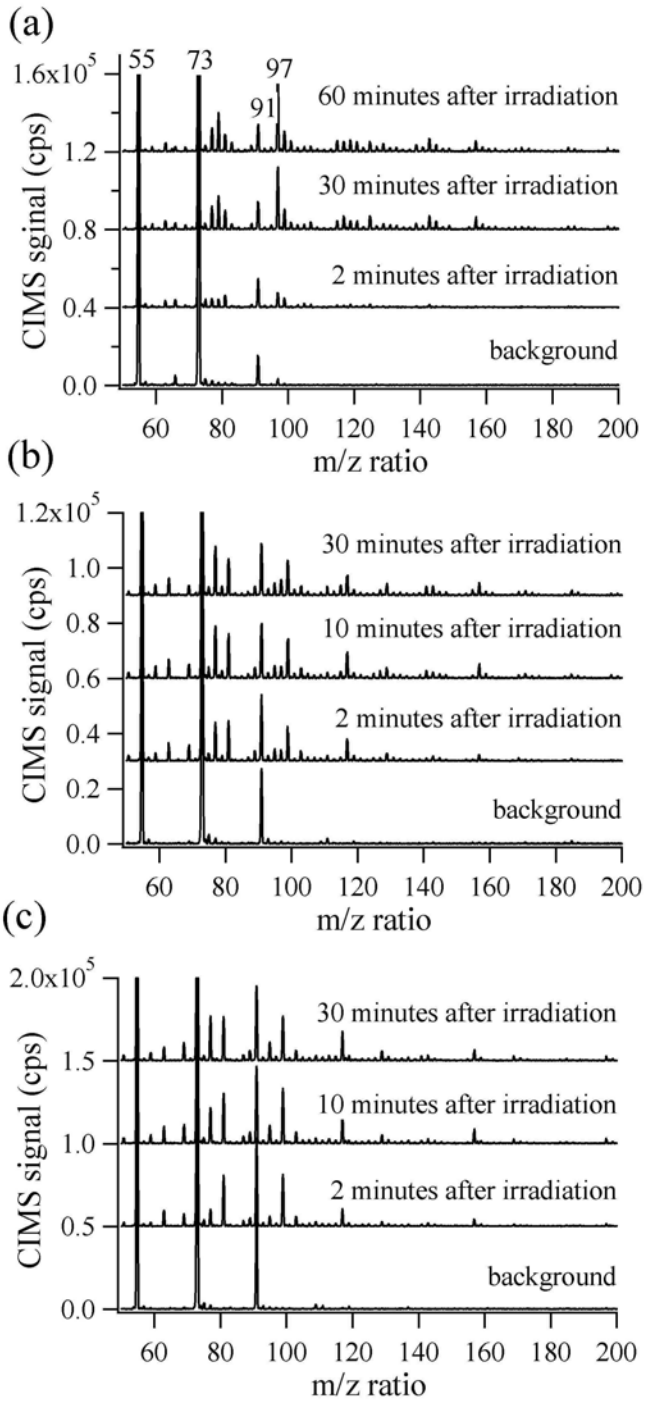

Figure 3.3 Mass spectra of photolysis products of limonene SOA generated under different conditions

Optical extinction coefficients of SOA constituents generally decrease with wavelength in the near UV range [52], whereas the intensity of Xe-lamp emission increases with wavelength. As a result of these two competing effects, there was an optimal irradiation wavelength (~290 nm), which produced the largest amount of volatile SOA photodegradation products. Figure 3.3 shows selected mass spectra observed before and during the 290 nm irradiation of SOA filters from low, intermediate, and high ozone concentration experiments.

In the absence of radiation, the observed mass spectrum typically contained only peaks at 55, 73, and 91 *m/z* attributable to ion clusters $(H_2O)_nH^+$, with n=3, 4, and 5, respectively. If the SOA filters were not sufficiently purged with dry nitrogen prior to their placement in the photolysis cell, additional ions were often observed in the background spectrum. In that case, purging continued until only $(H_2O)_nH^+$ ions remained. Irradiation of the filter resulted in the appearance of many additional peaks in the spectrum from photodegradation of SOA material. We explicitly verified that the observed VOCs were produced photochemically, and not as a result of a radiative heating of the sample (irradiation increased the filter temperature by less than 2°C). Intentional heating of the sample to ~100°C produced a completely different pattern of peaks in the mass spectrum (Fig. 3.4) that was very similar to the CIMS mass spectra of vaporized limonene SOA particles reported in Ref. [81].

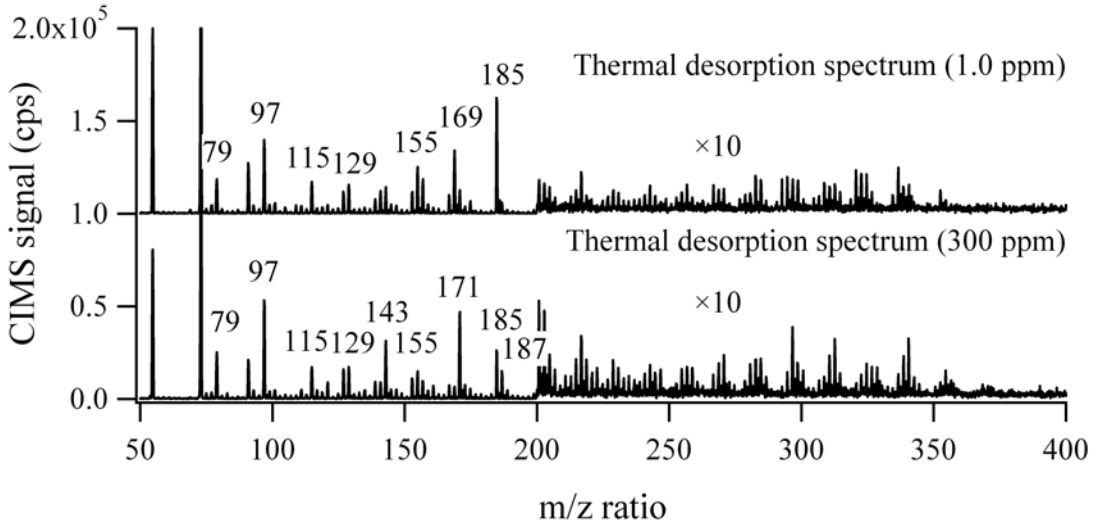

Figure 3.4 Thermal desorption mass-spectra of limonene SOA

The expected photodegradation products should contain only C, H and O atoms, and only oxygenated species, i.e., alcohols, carbonyls, carboxylic acids, and possibly peroxides, should be detectable by this CIMS instrument. The mass spectra in Fig. 3.3 contain families of peaks separated by 18 *m/z* suggesting that each neutral product M produced several ions $MH^+ \cdot (H_2O)_n$ with a range of n values. Dimeric ions $M_2H^+ \cdot (H_2O)_n$ were also detectable in the mass spectrum. Most peaks below 120 *m/z* could be assigned (Table 3.2) to CH_3OH, HC(O)OH, $CH_3C(O)H$, $CH_3C(O)OH$ and a C3-carbonyl ($CH_3C(O)CH_3$ or $CH_3CH_2C(O)H$). Peaks at higher *m/z* values, e.g., 141, 143, 157, 169, and 197 *m/z* could not be assigned with certainty.

Photoproduct	MH^+	$MH^+ \cdot H_2O$	$MH^+ \cdot (H_2O)_2$	$MH^+ \cdot (H_2O)_3$	$MH^+ \cdot (H_2O)_4$	M_2H^+	$M_2H^+ \cdot H_2O$	Yield (0.1 ppm)	Yield (1 ppm)	Yield (300 ppm)
CH_3OH	n/o	51	69	87	105	n/o	n/o	0.37-0.44	0.30-0.35	0.20-0.30
HC(O)OH	47	65	83	101	119	n/o	n/o	0.024-0.067	0.09-0.13	0.36-0.7
$CH_3C(O)H$	45	63	81	99	117	89	107	1	1	1
$CH_3C(O)OH$	61	79	97	115	133	n/o	n/o	0.027-0.05	0.20-0.45	2.2-3.8
$CH_3C(O)CH_3$*	59	77	95	113	131	117	135	0.40-0.51	0.52-0.67	0.41-0.51

Table 3.2 Identified peaks and their yield under different experiment conditions

The mass spectra of photodegradation products for SOA produced at different ozone concentrations were somewhat different (Fig. 3.3). The high ozone concentration SOA had more unidentified peaks at higher *m/z* values, and the observed products were more oxygenated. For example, the peaks attributable to $CH_3C(O)OH$ were enhanced relative to $CH_3C(O)H$ peaks in the high concentration experiments. The relative yield of acetone was also enhanced at high O_3. Finally, the high concentration SOA samples required less UV intensity to generate an observable signal, presumable because of the larger amount of SOA material collected on the filters.

3.3.2 Action spectra of SOA photodegradation products

To investigate the wavelength dependence of the relative yields of SOA photodegradation products, mass spectra were recorded at different irradiation wavelengths for identical SOA samples. Figure 3.5 compares mass spectra observed after 30 minutes of irradiation at six different wavelengths for a 1 ppm ozone experiment. For all irradiation wavelengths a similar distribution of the major product peaks was observed, although the overall intensities changed. This implies that there is no significant change in the photodegradation mechanisms over the studied wavelength range.

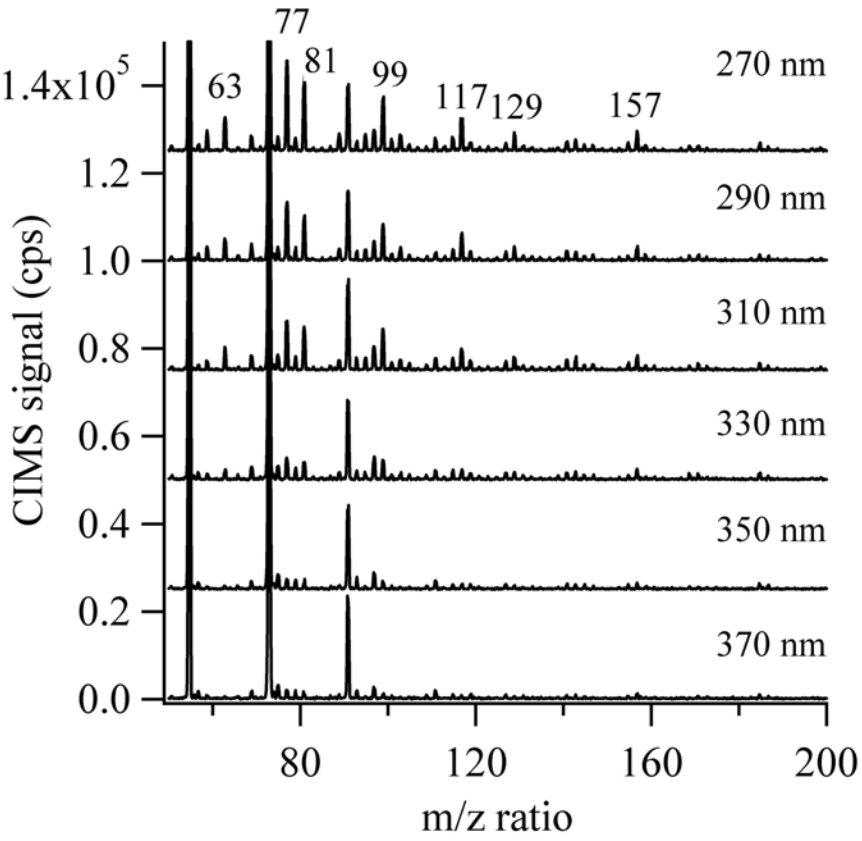

Figure 3.5 Mass spectra of photolysis products of limonene SOA exposed to different light radiation wavelengths

For each set of SOA filters, the experiments were conducted under conditions wherein the total ion current (*TIC*) was constant over the course of the measurements, and equal to the sum of all $(H_2O)_nH^+$ ion intensities prior to irradiation:

$$TIC = \left(\sum_n (H_2O)_n H^+ \right)_{initial} = \text{constant} \qquad (1)$$

The total product ion current (*PIC*) was calculated by summing ion intensities from all detectable photodegradation products, or equivalently, by subtracting the $(H_2O)_nH^+$ ion intensities from the overall ion current.

$$PIC = \sum \text{products} = TIC - \left(\sum_{n} (H_2O)_n H^+ \right) \qquad (2)$$

We verified that both methods in equation (2) gave identical results within experimental uncertainties, although summing the products resulted in higher signal-to-noise ratios for *TIC* because of the low background ion signals in the absence of irradiation.

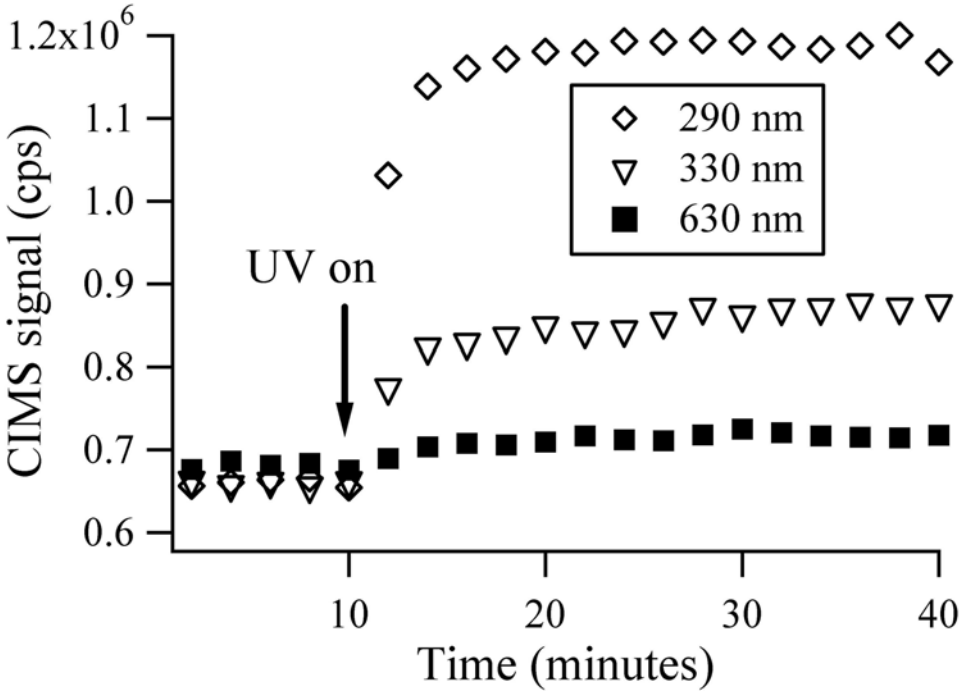

Figure 3.6 The observed PIC signal vs. photolysis time

Figure 3.6 shows a typical time dependence of *PIC* for SOA samples irradiated at three selected wavelengths. The observed photoproducts did not appear instantaneously but instead reached a steady-state level on time scales of 5-20 min for samples prepared at different O_3 concentrations. This time was significantly longer than the time required for molecules to travel through the CIMS inlet lines (< 0.4 s), and the residence time in the ionization region (~ 1 s). The rate with which the signal reached a steady-state

appeared to be limited by the transfer of the photodegradation products from the SOA material into the gas phase. Indeed, it took considerably longer for SOA samples prepared under high ozone concentration conditions to reach a steady-state because they had more SOA material deposited on the filters.

We constructed the action spectra by normalizing the observed peak intensities by the wavelength-dependent flux of photons incident on the filter.

$$Y_i(\lambda) = \frac{Intensity_i(\lambda)}{\lambda \times power(\lambda) \times TIC} \qquad (3)$$

$Intensity_i(\lambda)$ is the observed CIMS signal due to a specific product for the specified irradiation wavelength, and $Y_i(\lambda)$ is the wavelength-dependent relative yield of this product. The wavelength appearing in the denominator is necessary to convert the measured radiation power (in watts) into the relative photon flux (photons per second). The total relative yield of photodegradation products was defined in a similar way:

$$Y_{total}(\lambda) = \frac{PIC(\lambda)}{\lambda \times power(\lambda) \times TIC} \qquad (4)$$

The yields defined in equations (3) and (4) do not take into the account different sensitivities of the CIMS instrument to different VOCs. Therefore, in the absence of proper calibration, the values of Y_i cannot be used to directly compare absolute yields of different photodegradation products. However, they are still useful in comparing the yields for one and the same product at different irradiation wavelengths.

To facilitate comparison of experiments done on different sets of SOA samples, the yields were further normalized to the respective yield measured at 270 nm, for example:

$$Y_{total}^{normalized}(\lambda) = \frac{Y_{total}(\lambda)}{Y_{total}(270\ \text{nm})} \qquad (5)$$

Figure 3.7 shows the resulting action spectrum for the normalized total product yield. The shape of the action spectrum appears to be remarkably insensitive of the initial ozone concentration. Furthermore, the photodegradation action spectra closely mimic the absorption spectrum of the SOA sample.

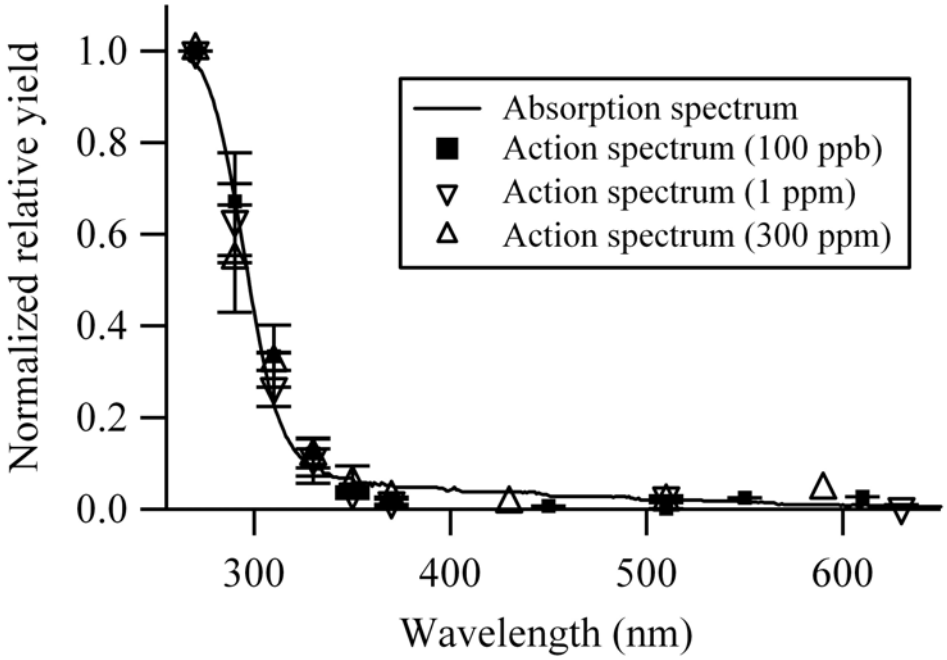

Figure 3.7 Action spectra vs absorption spectrum of limonene SOA

3.3.3 Effect of SOA aging on photodegradation

In the process of conducting these measurements, we noticed that measured values of Y_{total} were slowly decreasing with time as the filters were stored in darkness under dry nitrogen. One aging experiment was done to quantify the rate with which this reduction in photodegradation efficiency took place. High concentration limonene SOA particles were stored under N_2 flow (100 sccm) in darkness. At certain time intervals, one

of the filters was retrieved from the storage environment, and its Y_{total} measured at 310 nm. Figure 3.8 shows the resulting dependence of Y_{total}(310 nm) on storage time. The product signal decreased by 50% in about 50 hours. Most of the decrease was likely due to a slow volatilization of material from the filter. However, slow polymerization reactions between SOA constituents observed by [52] may also have contributed to the reduced photodegradation rate.

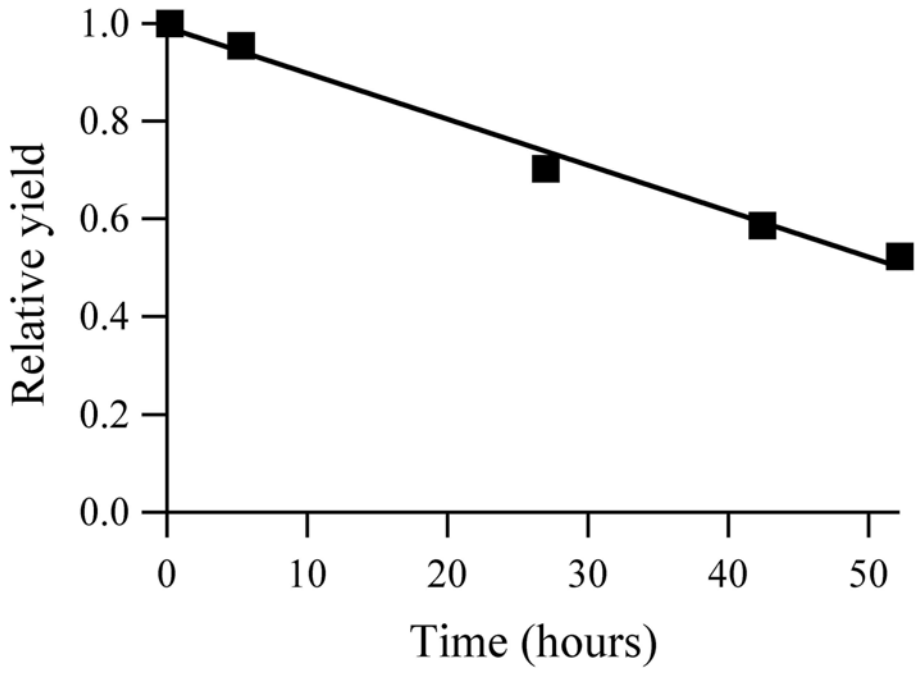

Figure 3.8 Photodegradation signal decrease with aging and/or evaporation of SOA sample

3.4 Discussion

3.4.1 Comparison of the CIMS and CRDS techniques

Refs. [27] and [52] previously studied photodegradation of limonene SOA prepared under the conditions of ozone and limonene concentrations corresponding to the

"high" case in Table 3.1. They used an infrared cavity ring-down spectroscopy (CRDS) instrument to detect volatile products of the photodegradation. The detection limit of the CRDS instrument is of the order of 10^{10} molec/cm^3 for molecules with reasonably strong rotationally resolved bands in the mid-IR range (e.g., CH_4, CO, CH_2O, HC(O)OH, CO_2). With the typical CRDS operational pressure of 100 Torr, this translates into 3 ppb effective detection limit for the mixing ratio. In contrast, the estimated detection limit for the new CIMS instrument is 0.01 ppb, which makes it possible to do experiments with considerably smaller quantities of SOA material. This work is the first report of photodegradation of limonene SOA prepared under more realistic atmospheric conditions ("low" case in Table 3.1).

The CRDS and CIMS approaches provide complimentary information: CIMS works best for molecules with high proton affinities, whereas CRDS works best for small molecules with narrow IR absorption features. Because of this selectivity certain SOA photodegradation products can only be detected with one of these approaches. For example, [52] reported an action spectrum for the release of CO resulting from Norrish type I splitting of carbonyls in the limonene SOA material. As the CIMS instrument is relatively insensitive to CO, no direct comparison is possible in this case. Ref. [27] reported an action spectrum for the release of formic acid during photolysis of limonene SOA measured as a function of the irradiation wavelength. Formic acid is also one of the major products detected by the CIMS instrument. Figure 3.9 demonstrates that the action spectra for the formic acid release independently obtained by these two methods are in near perfect agreement, a very satisfying cross-validation result.

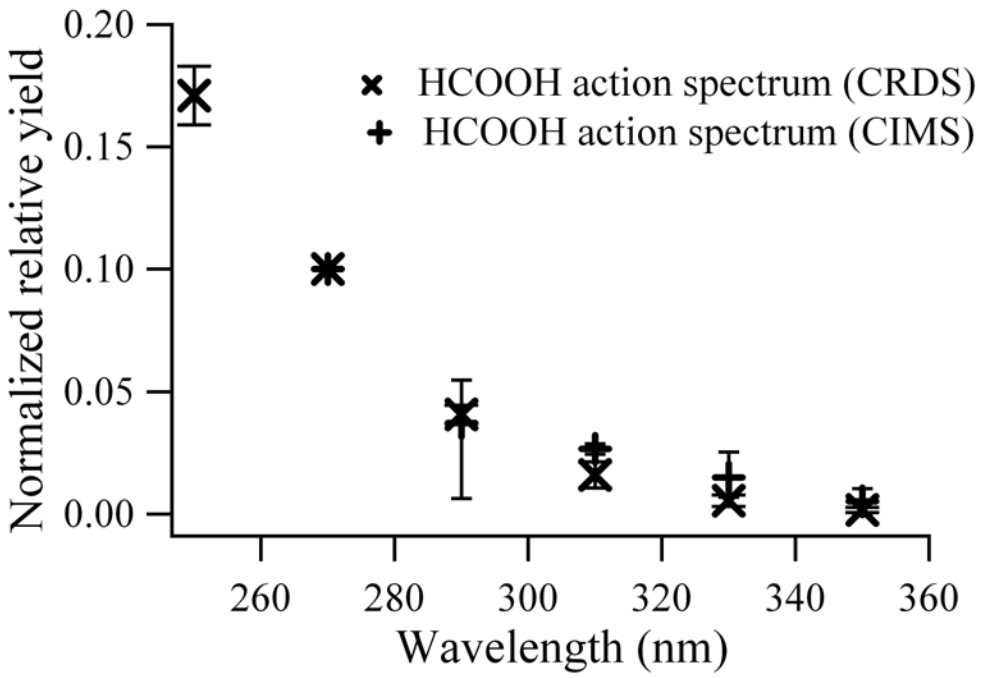

Figure 3.9 A comparison between HC(O)OH action spectrum obtained from CRDS and CIMS techniques

3.4.2 Effect of reactant concentrations on the action spectra

Although there are some differences between the distributions of volatile SOA photodegradation products (Table 3.2), the wavelength dependence of the overall photodegradation rate appears to be remarkably insensitive to the concentrations of ozone and limonene used in SOA preparation. Figure 3.7 demonstrates that the action spectra observed under the conditions of high, intermediate, and low reactant concentrations are identical within the experimental uncertainties. Furthermore, all action spectra have the same shape as the absorption spectrum of a freshly-prepared SOA material, which is also known to have insignificant dependence on the reactants' concentrations [52].

To understand the origins of the low degree of sensitivity of the photochemical properties of limonene SOA material to the concentrations of reactants, we have to consider the mechanism of limonene oxidation by ozone. The first step in this process is

concerted cycloaddition of ozone to the endocyclic double bond in limonene [51, 82, 83]. This splits the limonene's cyclohexene ring and produces two highly reactive Criegee Intermediates (CI*), which can isomerize into stable products, for example limononic acid or 7OH-limonaldehyde, decompose by expelling OH or O-atom, or react with H-donors such as alcohols or carboxylic acids to form organic peroxides (Fig. 3.10). Subsequent cross-reactions between alkylperoxy (RO_2) by-products of the CI* decomposition produce a number of additional stable and free radical species:

$$RO_2 + RO_2 \rightarrow \text{alcohol} + \text{carbonyl} + O_2$$

$$\rightarrow RO + RO + O_2$$

$$RO_2 + HO_2 \rightarrow ROOH + O_2$$

Decomposition, isomerization, and H-abstraction reactions involving alkoxy radicals (RO) lead to a "product explosion", with hundreds of chemically distinct species condensing in the limonene SOA matrix [78]. To complicate the matters, the first generation products undergo further oxidation and cross-reactions after condensing in the particle phase.

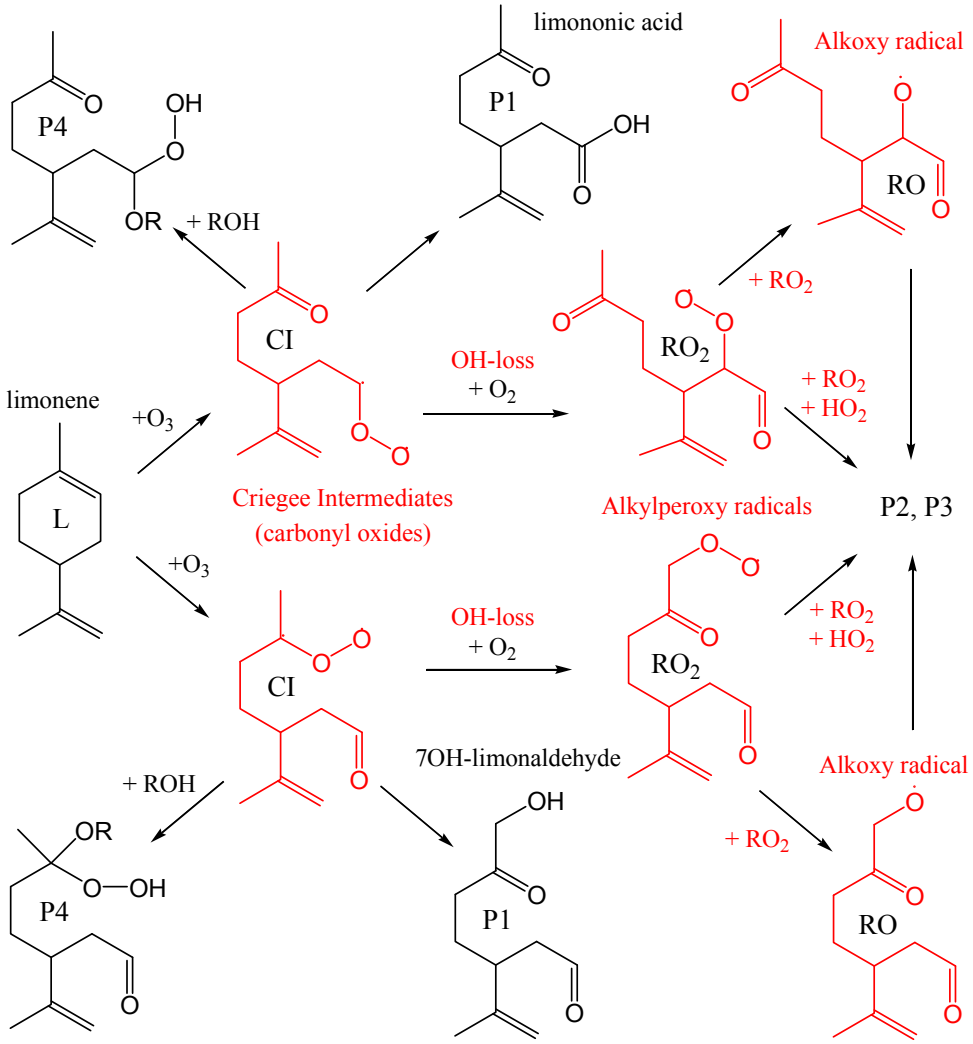

Figure 3.10 Simplified limonene ozonolysis mechanism

Detailed kinetic modeling of this chemistry is challenging but we can get some insight into the mechanism from a simplified kinetic model presented in Table 3.3. This model assumes that the majority of CI* species undergo OH-loss (~60%), with the resulting free radical being instantaneously converted into an alkylperoxy species (reaction 1a). A significant fraction (~20%) of CI* is collisionally stabilized (reaction 1b); the remaining (~20%) CI* isomerizes into first generation products grouped into category "P1" (reaction 1c). These branching ratios are consistent with the commonly assumed

yields of OH and SCI in the ozonolysis of monoterpenes [68, 83]. Similarly to the approach of Refs. [67] and [84], all RO_2 species are lumped together in this model in order to make it kinetically tractable. The chosen rate constant and branching ratios for the RO_2 cross-reactions (2a and 2b) is appropriate for large secondary RO_2 species with additional oxygen atoms in the chains attached to the –COO group [3]. The alcohols and carbonyls formed by the RO_2 cross-reactions are grouped into product category "P2". The RO species, which are also lumped together, are assumed to be capable of efficient isomerization by H-shift, with subsequent O_2 attachment regenerating RO_2 (reaction 3; detailed examples of these isomerization reactions can be found in Ref. [78]). Reaction 4 between RO and O_2 offers a pathway to HO_2 and generates additional products in the P2 category. Additional RO_2 species can be generated from reaction (5) of OH with limonene or with any of the stable products occurring with near gas-kinetic rates. HO_2 can also be produced from reaction (6) between OH and O_3 [85]. Reactions (7) between RO_2 and HO_2 radicals are known to be fast and they generally produce organic peroxides [3], which are lumped together under "P3" category. Finally, the stabilized Criegee Intermediate (SCI) is assumed to undergo a slow reaction (8) with products P1-P3 forming alkoxyhydroperoxides (Fig. 3.10), which are lumped into product group "P4". Several termination (9, 10, 12, 13) and propagation (11) reactions are also included in the mechanism to prevent an unrealistic build-up of free radicals.

Reaction		Rate constant	Yield
1a.	$O_3 + L \rightarrow CI^* (+O_2) \rightarrow RO_2 + OH$ (decomposition)	2×10^{-16}	0.6
1b.	$O_3 + L \rightarrow CI^* \rightarrow SCI$ (collisional stabilization)	2×10^{-16}	0.2
1c.	$O_3 + L \rightarrow CI^* \rightarrow P1$ (isomerization)	2×10^{-16}	0.2
2a.	$RO_2 + RO_2 \rightarrow P2 + P2 + O_2$ (stable products)	1×10^{-13}	0.5
2b.	$RO_2 + RO_2 \rightarrow RO + RO + O_2$ (alkoxy channel)	1×10^{-13}	0.5
3.	$RO \rightarrow$ isomerization $(+O_2) \rightarrow RO_2$	1×10^{5}	
4.	$RO + O_2 \rightarrow P2 + HO_2$	8×10^{-15}	

5.	OH + L, P1, P2, P3 or P4 (+O_2) → RO_2	5×10^{-11}
6.	OH + O_3 → HO_2 + O_2	7.3×10^{-14}
7.	HO_2 + RO_2 → P3	1×10^{-11}
8.	SCI + P1, P2 or P3 → P4	1×10^{-14}
9.	OH + HO_2 → H_2O + O_2	1.1×10^{-10}
10.	HO_2 + HO_2 → H_2O_2 + O_2	1.9×10^{-12}
11.	HO_2 + O_3 → OH + 2 O_2	1.9×10^{-15}
12.	OH → wall loss	1×10^{-1}
13.	HO_2, RO_2 or SCI → wall loss	5×10^{-3}

Table 3.3 Reactions and Reaction rate constants involved in the approximate mechanism of SOA formation

We can make approximate associations between the groups P1-P4 and actual chemical functional groups in the product molecules. P1-type products are likely to contain either two carbonyls or one carbonyl and one carboxyl functional group (examples are given in Figure 3.10). The first carbonyl moiety comes from the initial splitting of the endocyclic double bond, whereas the second functional group results from the unimolecular isomerization of CI*. P2-type products are likely to contain at least two carbonyls or one carbonyl + hydroxyl moieties because RO_2 cross reactions are known to result in an alcohol/carbonyl pair [3]. P3-type products are expected to be dominated by organic peroxides ROOH. Alkoxyhydroperoxidic P4-type products have dimeric structures $R_1R'_1C(OOH)OR_2$ in a sense that they contain leftovers of two limonene molecules; efficient formation of such dimers have been observed by [76] and [86] during early stages of α-pinene ozonolysis. In addition to the –OO– peroxy group, both P3 and P4 should contain carbonyl function groups from the initial splitting of the endocyclic double bond.

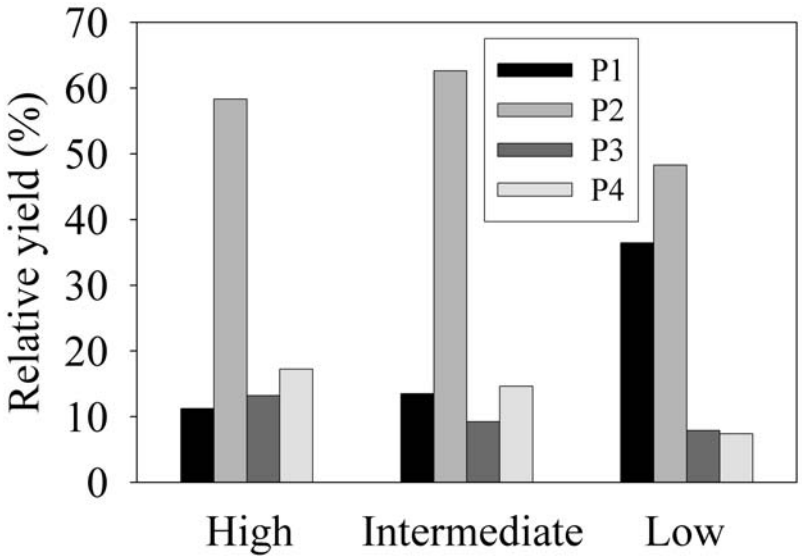

Figure 3.11 Distribution of products P1-P4 resulting from kinetic simulations

Kinetic simulations of this simplified mechanism with the initial concentrations of ozone and limonene from Table 3.1 resulted in the product distribution shown in Fig. 3.11. Despite the fact that ozone and limonene concentrations change by 2-3 orders of magnitude in our experiments, the final distribution appears to be dominated by the P2 products from RO_2+RO_2 reactions in all cases. In the high and intermediate cases, the yield of P2 products is close to the initial yield of OH (and RO_2) in the CI* decomposition. In the low case, the loss of RO_2, HO_2 and SCI by reaction (13) starts to compete with formation of products P2-P4, and the yield of direct CI* isomerization products P1 increases. According to this model, only P1-type products should remain in the low concentration limit; all four types of products should be present in the high concentration limit.

We believe that our experimental conditions correspond to the high concentration

regime, wherein the majority of products are generated via the RO_2 cross-reactions (2). This assumption is supported by: (1) the strikingly large number of peaks in the high-resolution limonene SOA mass spectrum attributed to RO chemistry [78]; (2) the insensitivity of the high-resolution SOA mass spectrum to ozone concentration [78]; (3) the lack of dependence of the observed action spectra of limonene SOA material on the reactant concentrations. With the expected order of product yields (P2 > P1 ~ P3 ~ P4), the carbonyl group should be the most important functional group with photochemical activity in the actinic region of the solar spectrum. The fraction of oxygen sitting in the –OO– peroxy groups should also be significant. As discussed in [52] the absorption spectrum of limonene SOA material in the vicinity of 300 nm can indeed be modeled as a composition of overlapping $n\rightarrow\pi^*$ bands of carbonyls and $n\rightarrow\sigma^*$ bands of peroxides.

3.4.3 Effect of reactant concentrations on the photodegradation products

The distribution of gaseous products of limonene SOA photodegradation does depend on the concentrations of reactants used in the SOA synthesis (Table 3.2). The degree of oxidation in the observed products appears to increases at higher ozone concentrations. For example, $CH_3C(O)OH$ and $CH_3C(O)H$ represent the most easily detectable photoproducts under the "high" and "low" conditions, respectively. This behavior can be linked to the chemistry of the less reactive exocyclic double bond in limonene. While it is likely to survive the initial attack by ozone, it may still be oxidized by the excess ozone after the first generation products P1-P2 condense in the aerosol phase [87]. SOA prepared under low concentration conditions still contains a number of molecules with intact exocyclic double bounds [67, 78]. For example, peaks at 169 *m/z*

and 185 *m/z* in the SOA thermal desorption mass spectrum (Fig. 3.4) likely correspond to protonated limononaldehyde and limononic acid, respectively, both of which still have this double bond. As the ozone concentration increases, the peaks at 169 and 185 *m/z* become smaller, whereas peaks at 171 and 187 *m/z* grow in as a result of the following reaction:

$$>C{=}CH_2 \;+\; O_3 \;\rightarrow\; >C{=}O \;+\; CH_2OO \qquad (\Delta m/z = +2)$$

$$CH_2OO \;+\; RC(O)OH \;\rightarrow\; HOOCH_2OC(O)R$$

The second reaction corresponds to scavenging of the Criegee intermediate CH_2OO by carboxylic acid groups within the SOA matrix [88]. The increase in the oxygen content of SOA caused by these and other oxidative processes is expected to increase the oxygen content in the SOA photodegradation products.

3.4.4 Atmospheric relevance

Several recent aerosol chamber studies underscored the importance of measuring SOA yields and characterizing SOA chemical composition at low loadings of organic material [89-91] and with careful control of NO_x levels [46, 51, 92-94]. Although the lowest concentrations of reactants used in this study approach typical atmospheric values, the SOA formation still appears to be dominated by the RO_2+RO_2 and RO_2+HO_2 reactions under our NO_x-free conditions. In a more realistic atmospheric environment, RO_2 radicals will instead react with atmospheric NO when both $(k_{RO_2+NO}\times[NO])/(k_{RO_2+HO_2}\times[HO_2])$ and $(k_{RO_2+NO}\times[NO])/(k_{RO_2+RO_2}\times[RO_2])$ exceed 1. With representative rate constants, $k_{RO_2+NO} \sim 10^{-11}$ cm^3 molec^{-1} s^{-1}, $k_{RO_2+RO_2} \sim 10^{-13}$ cm^3 molec^{-1} s^{-1}, $k_{RO_2+HO_2} \sim 10^{-11}$ cm^3 molec^{-1} s^{-1} [40], and with typical peak concentrations in remote

areas, $[HO_2+RO_2]$ = 10^8-10^9 molec cm^{-3}, [NO] = 10^8-10^{10} molec cm^{-3} [3], the involvement of NO can be ignored only under unusually clean atmospheric conditions. Furthermore, ozone is not the only oxidant responsible for oxidation of terpenes; OH and NO_3 also make a significant contribution [40]. This brings up the following question: are the photodegradation processes observed in this study bear any relevance to the photochemical processes occurring in realistic organic aerosols?

One can argue that the mechanism of photodegradation of SOA prepared in a NO_x-free environment will be similar to that for SOA prepared by oxidation of terpenes in the presence of NO. The RO_2+NO reaction generates RO radical, which eventually becomes a carbonyl species that is similar or even identical to the carbonyls produced by the RO_2+RO_2 reactions. For the large RO_2 species generated by monoterpene ozonolysis, the yield of organic nitrates $RONO_2$ produced by the RO_2+NO reaction can be substantial (~25%) but the -ONO_2 is not expected to be photochemically active at λ>300 nm, the actinic wavelengths capable of reaching the lower troposphere. The OH-initiated oxidation of terpenes will give a different distribution of SOA constituents, with a considerably reduced fraction of peroxides amongst the final products compared to the ozone-initiated case. However, carbonyl products are expected to be just as important in photochemically produced SOA as in SOA derived from the ozone+olefin chemistry. We conclude that photodegradation processes taking place in our "idealized" limonene SOA material should be representative of realistic biogenic SOA as long as carbonyl functional groups remain the dominant absorbers in the actinic range of the tropospheric solar radiation.

Chapter IV

Photochemistry of limonene/NO_3 SOA

4.1 Introduction

Atmospheric NO_3 is formed by the reaction of NO_2 with O_3. NO_3 is sensitive to solar radiation and easily photodissociates into NO_2 + O or NO+O_2 [3]. The nighttime concentration of NO_3 in troposphere can reach 350 pptv, which makes NO_3 important at nighttime for chemistry of VOC [95, 96]. The formation of monoterpene SOA by NO_3 oxidation is the most important sink for monoterpenes at night. The generated SOA can stay in the atmosphere for up to one week. Photodegradation is potentially an important aging processes for NO_3 derived SOA, similarly to the O_3 derived SOA.

Previous research on reaction mechanism between NO_3 and limonene was described in Chapter II. This chapter will introduce preliminary results of the experiments on photochemical aging of limonene/NO_3 SOA.

4.2 Experimental

4.2.1 Limonene SOA generation and collection

NO_3 radicals were generated by thermal decomposition of N_2O_5 ($N_2O_5 \rightarrow NO_2 + NO_3$), which was synthesized by the reaction of NO_2 with O_3. Pure gas phase NO_2 (liquid phase in cylinder, Matheson tri-gas, CP grade 99.5%) was mixed with 1% O_3/O_2 mixture generated by an O_3 generator (Ozonetech OZ2SS). The mixture was at pressure of 680-730 Torr. The NO_2 flowrate was 0.8 L/minute and O_3/O_2 flowrate was 1.5 L/minute.

The produced N_2O_5 condensed into white powder in a glass container which was in liquid N_2/ethanol mixture trap at -80°C. The collected solid N_2O_5 powder was stored at - 70°C until use.

Organic particles were generated in a 250 L Teflon chamber at room temperature. The chamber was first filled with dry purified air to 250 L. Four μL Limonene was injected by a microsyringe. Although most limonene was evaporated during the injection, enough time was taken before introducing NO_3 so as not to have any remaining liquid limonene in the chamber. After limonene was injected, N_2O_5 was introduced into the chamber by flowing dry purified air through a N_2O_5 trap at a temperature under its melting point (-36°C). A NO_y monitor was connected to the chamber to monitor the total NO_y concentration during the reaction. Typical concentration of limonene injected in the chamber was usually 2-3 ppmv, and the initial total NO_y concentration was 5 – 10 ppmv. Mixing of limonene with NO_3 was conducted for 30 minutes at room temperature in the dark in order to avoid photolysis of NO_3. Particle generation was confirmed by a particle counter measurement. The particle formation was monitored by SMPS (TSI, model 3080) in selected experiments.

Particles were collected on glass fiber filters (Millipore APFF 04700, 0.7 μm pore) by pumping out the content through the filters at 2.5 litters per minute for 10 minutes. Six samples of filters were collected at the same time and all filtered samples were stored in darkness. The weight of collected SOA material was measured with Sartorius ME5-F filter balance with 1 μg readability.

Particles were also collected by impaction on 2.5 cm diameter CaF_2 windows in order to record UV/vis absorption spectra of SOA material with Shimadzu UV-2450

dual-beam spectrophotometer. A relatively uniform film of SOA material was prepared by compressing the collected particles between two CaF_2 windows and gently heating them as described in previous paper [52].

4.2.2 SOA photolysis measurement by CIMS

Photolysis products were carried by ultra high purity N_2 into the CIMS for detection. The setup was exactly same as the experimental setup described in chapter III. UV light from monochromator/Xe-lamp photolyzed the collected NO_3 oxidized limonene SOA. Most organic chemicals except alkane could be detected by the CIMS machine. Mass spectra were collected every two minutes during and after irradiation to have a time profile of products growth. The observed range was between *m/z* 10 and 400 with the resolution of 1 *m/z*. The spectra collected before irradiation were averaged and regarded as background.

4.3 Results

4.3.1 Particle size distribution

Particle size distribution and the concentrations of ozone and NO_y were measured by SMPS (TSI, model 3080), and the ozone and NO_y monitors during the oxidation reaction in the Teflon chamber. The result is shown in figure 4.1. The NO_y concentration constantly increased for 30 min after N_2O_5 injection into the chamber, reached to 7 ppm, and then started to decrease. The O_3 concentration started to increase as soon as N_2O_5 was introduced into the chamber as well. However this had a local maximum of 72 ppb at 8 minutes after the N_2O_5 injection and decreased for 4-6 min reaching to almost 0 ppb.

Then it started to increase gradually and took about 30 min to become constant at 75 ppb.

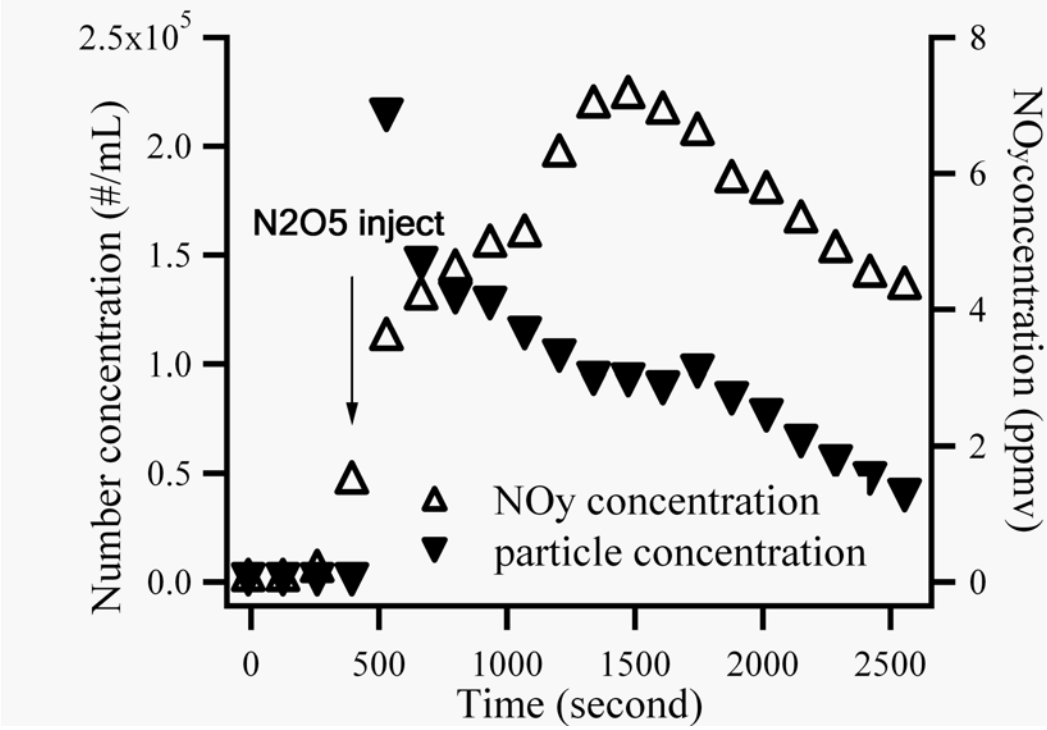

Figure 4.1 Particle concentration and NO_y concentration change with reaction time

The particle size distribution time profile is shown in Figure 4.2. The SMPS started to detect particles 3 min after the N_2O_5 injection, before O_3 concentration reached its first maximum. There were two maxima at 370 and 615 nm. The particle counts and the cumulative particle volume peaked early in the reaction (< 5 min) and started to decrease after that. The maximum at 370 nm never changed its position, while the maximum at 615 nm shifted to 685 nm during the next SMPS scan, and stayed there until the two maxima merged together.

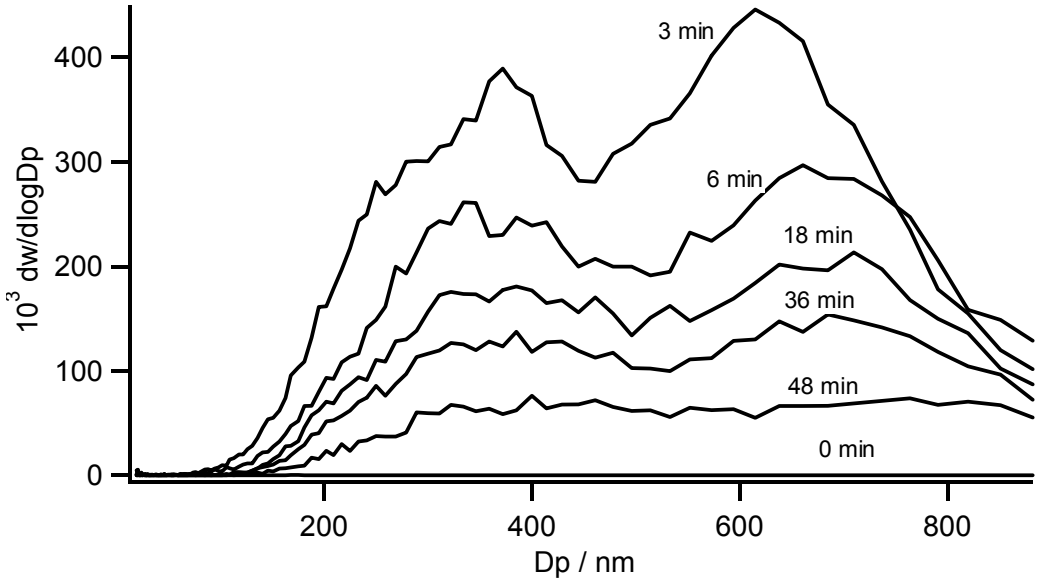

Figure 4.2 Particle mass distribution in NO_3 + limonene reaction as a function of time

4.3.2 UV absorption

Figure 4.3 shows the UV absorption spectrum of SOA particles collected on the CaF_2 window. The spectrum has a weak absorption at the atmospheric actinic region (> 295 nm). This absorption is likely due to aldehydes and ketones in the particles.

The absorption is relatively weak compared to the SOA generated from ozone initiated oxidation of limonene. Although the collected amount was same with the same procedure for the collection (1 SLM for 1 hour) the absorbance of limonene/NO_3 particles was less than 1/10 of that of limonene/O_3 particles.

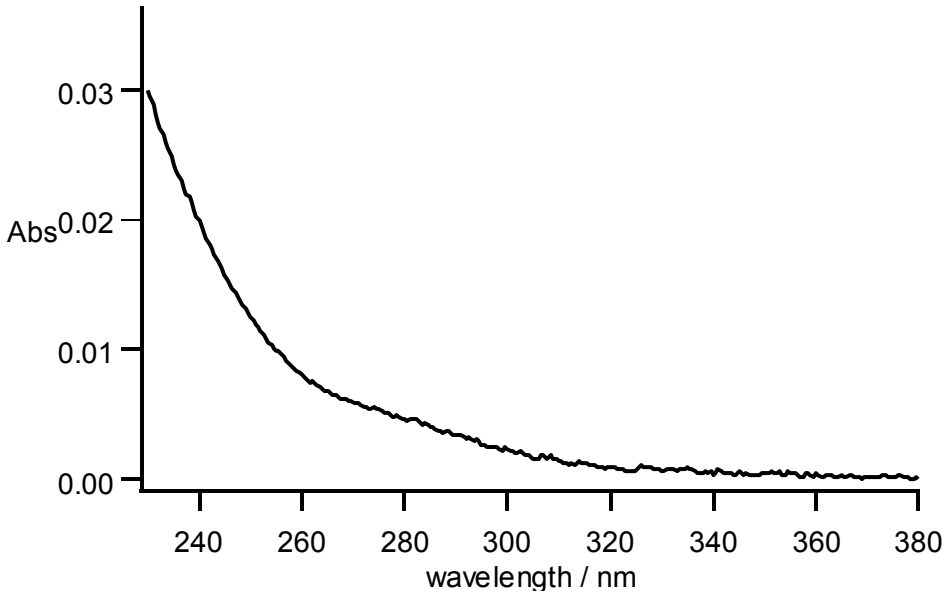

Figure 4.3 UV absorption spectrum of limonene/NO_3 SOA material

4.3.3 Time profile of photolysis products

Figure 4.4 shows selected mass spectra during and after irradiation of the collected particles of limonene/NO_3 SOA at 290 nm. When the irradiation started, some peaks immediately started to grow. The growth was usually saturated after 30 min irradiation. These peaks immediately decayed when the UV irradiation was turned off, implying that they were produced by photolysis.

In order to examine the photolysis products, the flow rate of the sample line was decreased to allow more concentrated samples sent into the ionization region. A mass spectrum with higher product peak intensity was obtained in this way. Figure 4.5 shows the resulting mass spectrum.

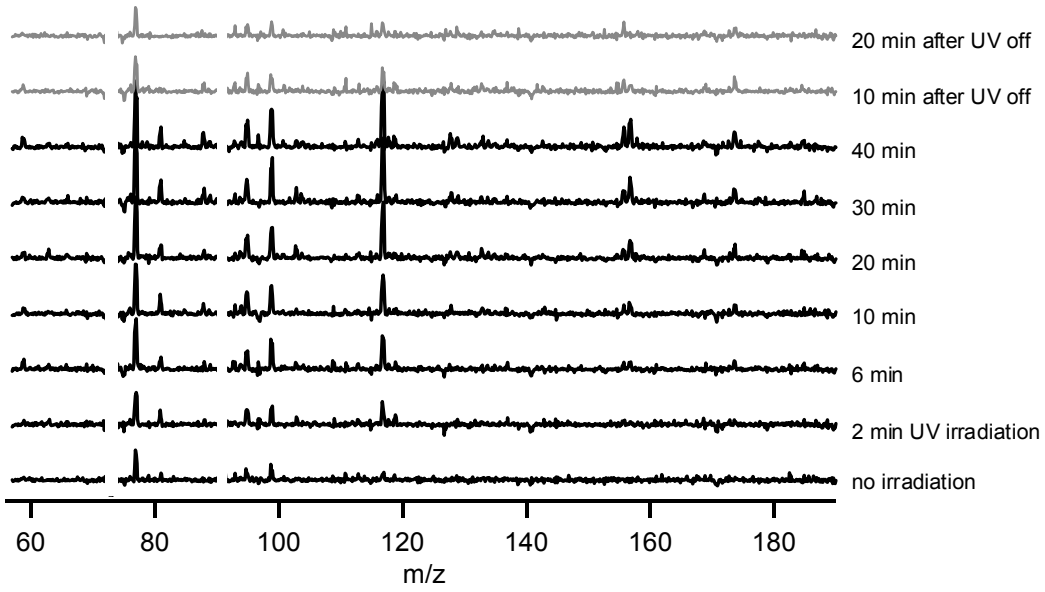

Figure 4.4 Time dependence CIMS spectra of gas phase photolysis products for limonene/NO_3 SOA

The existence of even *m/z* peaks implies that N atom is incorporated in the product molecules. The peaks at 48 and 66 *m/z* were initially believed to be $(HONO)H^+$ and $(HONO)(H_2O)H^+$ respectively, but a separate experiment proved that this instrument is insensitive to HONO. Peaks between 50 and 130 Dalton are small molecules, their dimers and their water clusters. Peaks at 59, 77, 95 and 113 *m/z* are believed to be acetone and its water cluster peaks. Peaks at 63, 81, 99, 117 *m/z* are $CH_3C(O)H$ water clusters. Peaks at 79, 97, 115 *m/z* are CH_3COOH water clusters. Most of the remaining peaks contain nitrogen atom which make them appear at even *m/z* values in the CIMS spectra. They are tentatively assigned to organonitrates ($RONO_2$) according to the possible mechanisms published by other researchers [3, 55, 79, 97, 98].

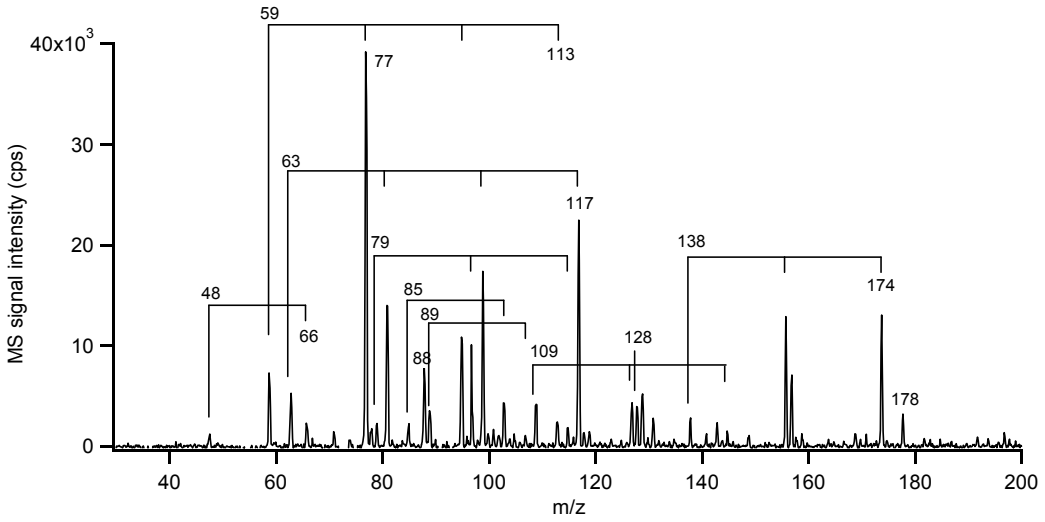

Figure 4.5 Sample mass spectrum of gas phase photolysis products of limonene/NO_3 SOA

The photoirradiation experiments were conducted at 270, 290, 310, 330, 350, and 370 nm. The observed ion peaks did not differ for these irradiation wavelengths. The relative amount of photolysis products were estimated by summing up the intensities of all peaks in the spectrum after the peak growth became stable, and was compared according to the wavelength. This method is exactly same as the method described in chapter III. For this comparison, the pressures of both sample flow line and water flow line, the condition of mass spectrometer were carefully maintained at the same levels for all experiments. The peak height of water cluster ions did not differ more than 10% and the total ion counts were within 5% for each set of experiment. The comparison is shown in Figure 4.6. The circles are the action spectrum and the line is the UV absorption spectrum.

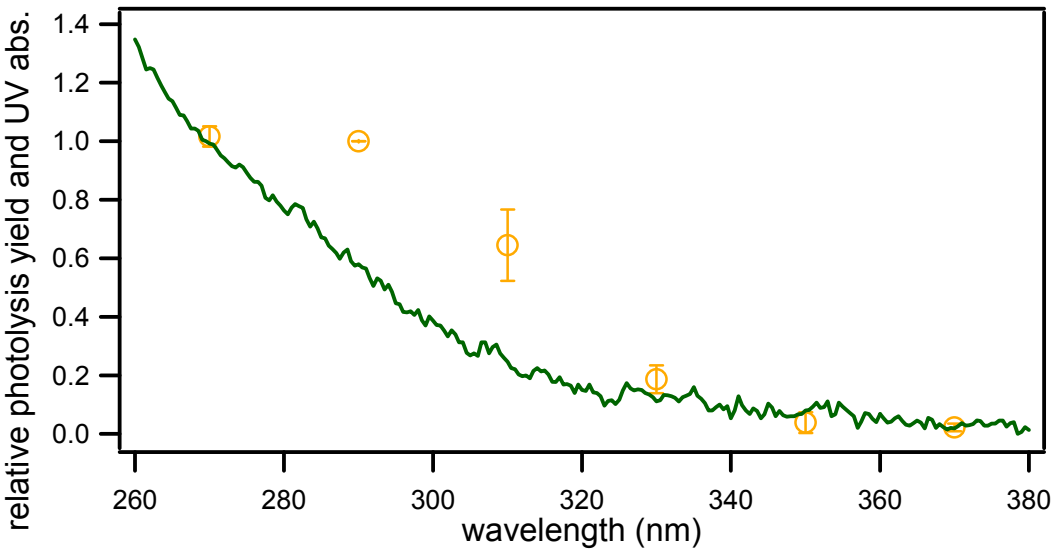

Figure 4.6 Action spectrum of photolysis of limonene/NO_3 SOA vs. its UV absorption spectrum

4.4 Discussion

4.4.1 Aerosol formation

The presence of O_3 in the chamber became a competative reaction to generate SOA, occurring in parallel to the reaction of limonene and NO_3. Although the reaction rate constant of limonene and NO_3 is higher than the reaction rate constant of limonene and O_3, and [NO_3] is higher than [O_3], the aerosol formation potentials are different. Two peaks in particle size distribution imply that a fraction of the particles were generated by the reaction of limonene and O_3. The peak around 370 nm in particle size distribution was likely produced by reaction of limonene and ozone; meanwhile the peak around 650 nm was likely produced by reaction of limonene and NO_3. The competition between NO_3 and O_3 in reaction with terpene was also seen in experiment in Ref. [43]. It means that the generated aerosol particles were actually a mixture of NO_3 and O_3 derived aerosol. The

peak around 650 nm is higher than the peak around 370 nm, which may imply that the NO_3 derived aerosol yield is higher than O_3 derived aerosol yield due to the much higher NO_3 concentration. The disappearance of peaks mean that the particles were coagulating and part of aerosol particles were lost on wall.

4.4.1 Mechanism of photolysis

All peaks in the mass spectra, except for the even *m/z* peaks, were the same as the ones in photolysis spectra of O_3 derived limonene SOA. This is not a surprise, not just because part of the aerosol particles were generated from reaction of limonene and O_3, but also because part of reaction products of limonene and NO_3 are same as reaction products of limonene and O_3. For example, one of the major products of limonene and NO_3 is endolim. Its yield was estimated from 28% to 69% [55, 79]. The exdo-cyclic double bond could also be attacked by NO_3. The ratio between endo and exdo is 65:35 [68]. So 4-acetyl-1-methylcyclohex-1ene is also a possible product. All of these products have a C=O functional group. They can undergo photolysis reaction via Norrish Type I and Norrish Type II mechanisms and form smaller molecules as products [52]. A simplified photolysis mechanism is shown in figure 4.7. Some of the possible products such as HCHO, CH_3CHO were indeed found in photodegradation mass spectra.

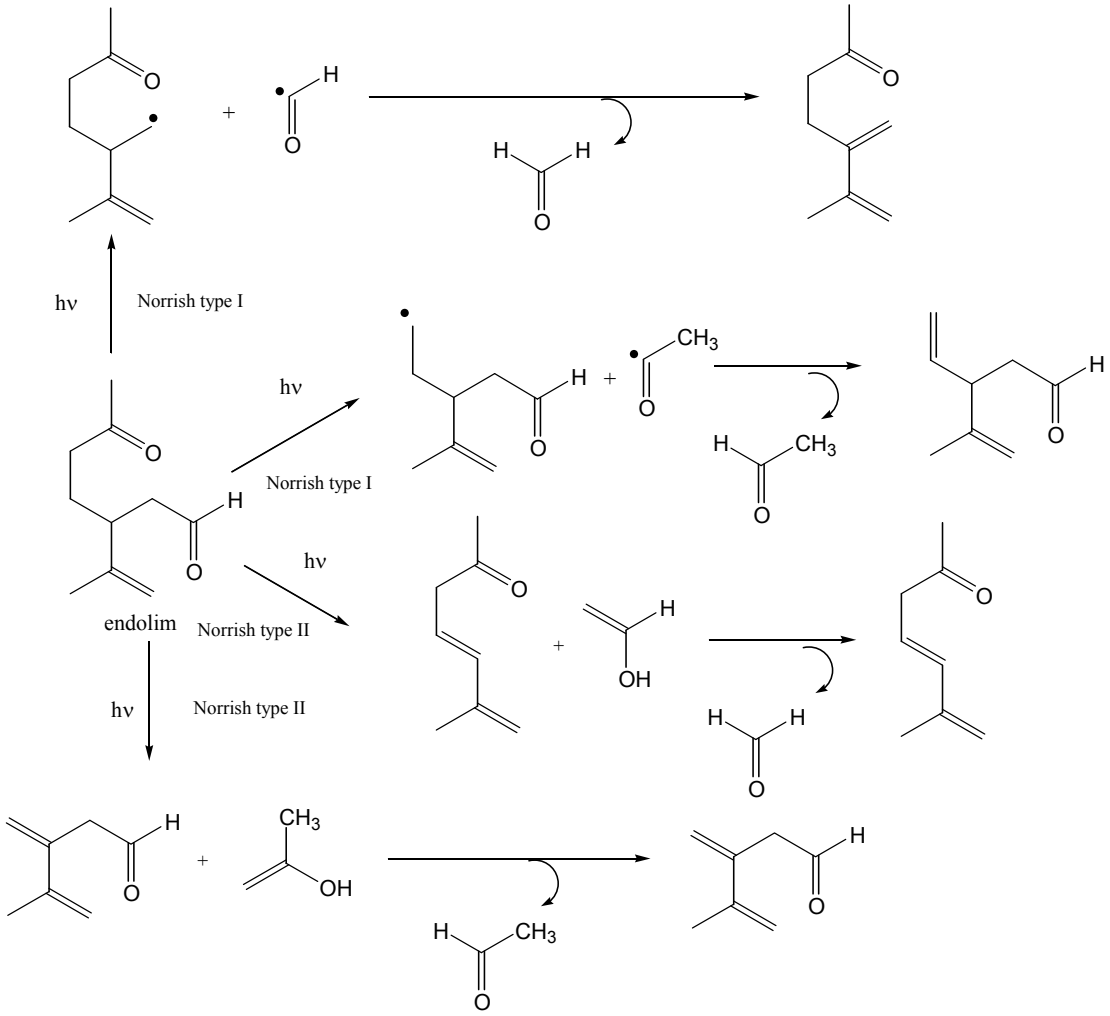

Figure 4.7 A simplified photolysis mechanism for endolimin an O_2–free environment

Another important functional group in the limonene/NO_3 SOA products is -ONO_2. The total $RONO_2$ production yield was estimated to be 67% [55] or 48% [79]. $RONO_2$ photolysis involves cleavage of the RO-NO_2 bond [99, 100].

$$RONO_2 + h\nu \rightarrow RO\cdot \ + \ NO_2$$

For generated RO radical, it can have decomposition, isomerization, and H-abstraction reactions, which lead to a "product explosion" with hundreds of chemically distinct species condensing in the limonene SOA matrix [78]. It has been discussed in

Chapter III.

Most even number peaks in photolysis mass spectra are relatively large, above 120 *m/z*. Since the molecular weight decrease and more double bonds present in photolysis products via Norrish type mechanism, the produced molecules could have higher volatility. those even number peaks might be C=O double bond photolysis products which still keep $RONO_2$ functional group.

In conclusion, there are no dramatic differences between gross details of photodegradation mechanism in limonene/O_3 and limonene/NO_3 aerosols. Both have photochemistry that is dominated by carbonyl absorptions.

Chapter V

ABB Extrel QMS

5.1 General Introduction to Mass Spectrometry

Mass spectrometers are powerful instruments designed to analyze various samples. A common mass spectrometer consists of four components: ion source, mass analyzer, detector and recorder [101].

When passing through an ion source, neutral molecules are ionized to positive ions or negative ions depending on ion source type. Electron impact ionization (EI) and chemical ionization (CI) are amongst the most common ionization techniques. Mass analyzers separate ions with different *m/z* ratios by different mechanisms. The most common mass analyzer is a quadrupole mass analyzer (QMS) described in section 5.2 in more details. Other commonly used mass analyzers are magnetic sector mass analyzer and time of flight mass analyzer *et al*. After mass analyzers, ions are detected by ion detectors and all signals are sent into recorders. The most common detector is an electron multiplier.

5.2 Description of ABB Extrel QMS platform (hardware)

For our research, we designed and constructed an Atmospheric Pressure Chemical Ionization Mass Spectrometer (AP-CIMS) consisting of a CI source, a QMS coupled with an axial molecular beam ionizer, a conversion dynode multiplier, and a 1MHz pulse amplifier. Since construction of this instrument took a significant fraction of my PhD

research, a detailed description of the instrument is included in this thesis. All components of the instrument except for the chemical ionization source are described in detail below. The arrangement of the whole system is also described in this part. The chemical ionization source is discussed in Chapter VI.

5.2.1 Axial molecular beam ionizer

An axial molecular beam ionizer is located in front of the quadrupole mass filter. The function of the axial molecular beam ionizer is to ionize neutral chemicals by electron impact and focus ions into the quadrupole mass filter. The sketch of the axial molecular beam ionizer used in this project is given below.

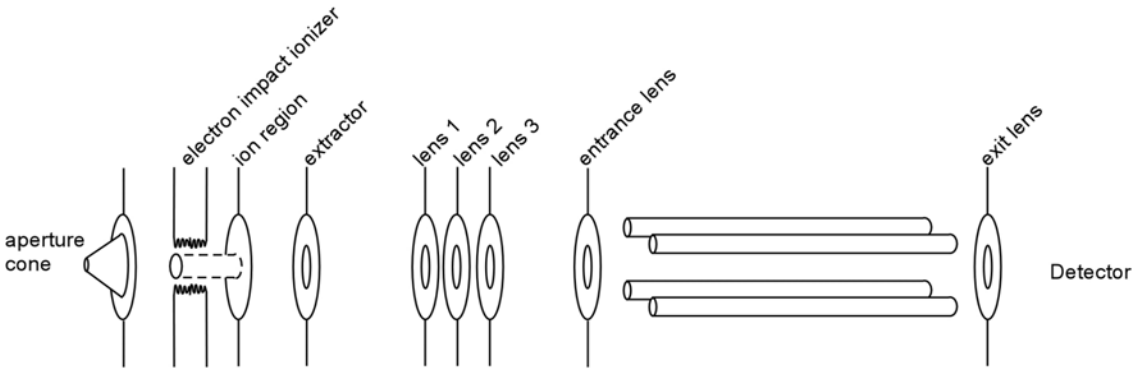

Figure 5.1 Axial molecular beam ionizer

The filament in the electron impact ionizer generates high energy electrons which hit molecules and form positive ions. The energies of the electrons depend on the voltage on the filament with respect to the voltage on the ion region electrostatic lens. The extractor pulls the ions out of the ion region. An Einzel lens helps focus ions in the QMS (lenses 1-3 in the Figure). Lens 1 and lens 3 have the same potential. The function of these three lenses is to focus ions into the quadrupole in order to increase the sensitivity

of the instrument. Entrance lens which sits before the quadrupole mass filter and exit lens which is after the quadrupole mass filter can help solve fringe field problem in the mass filter.

All voltages are provided by the optics supply module in the QMS controller. There are eight voltage generators (daughter boards) corresponding to all electrostatic optics described above in the optics supply module. The correspondence of board number, board and voltage range is listed in the table below.

Board #	Corresponding board	Voltage range	Typical Value for external ion transmission
1	Ion region	-100V to 100V	-50
2	Extractor	-100V to 100V	-80
3	Lens 1 and Lens 3	-400V to 400V	-150
4	Lens 2	-400V to 400V	-100
5	Entrance Lens	-400V to 400V	-20
6	Exit Lens	-400V to 400V	-300
7	Skimmer	-400V to 400V	-20
8	Pre- and post-Filters	-400V to 400V	-25

Table 5.1 Voltage range of daughter boards on optics supply module

One important modification of factory defaults needs to be mentioned. All voltages initially used to be referenced to the ion region potential; the ion region was the only voltage referenced to the ground. For example, if the ion region was set to 8 volts and extractor was set to -7 volts in the software, the actual voltage on the extractor was 1 volt. This referencing condition was changed in 2006 by cutting through a designated jumper on the control board. After this, all voltage settings have been referenced to instrument ground.

5.2.2 Mass filter

QMS consists of four 19 mm rods arranged as two parallel pairs as shown below. Two opposite rods form a pair, and each pair is electrically connected. A DC voltage U and a RF voltage Vcos(ωt) are applied to the two rod pairs. The total voltage on each pair is U+Vcos(ωt) and -U-Vcos(ωt). Changing the magnitudes of U and V without changing U/V ratio allows us to select certain *m/z* ratio ions. The unselected ions have unstable trajectory in the QMS and are neutralized and pumped eventually.

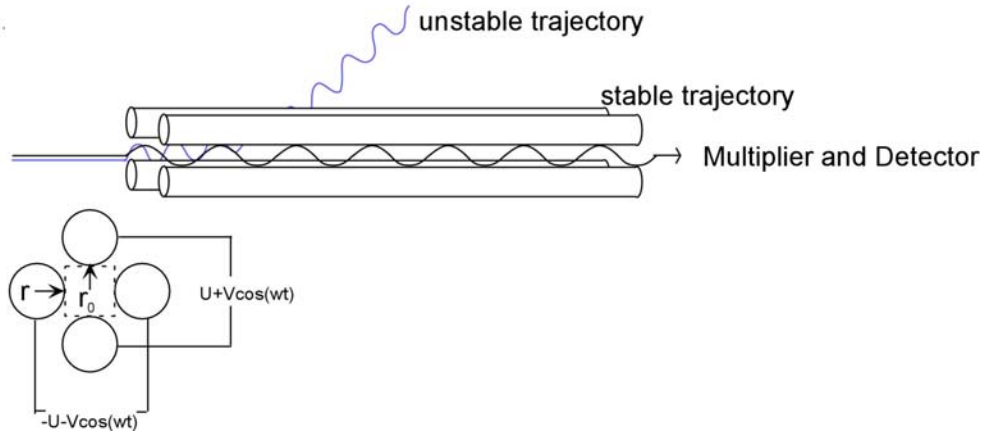

Figure 5.2, Quadrupole mass filter

5.2.3 Signal detection

After the mass selected ions pass through the quadrupole mass filter, the ion current is amplified in order to be measured. The detection part in our system is a conversion dynode multiplier. It includes a conventional channel multiplier and a conversion dynode (CD). The sketch below shows the conversion dynode multiplier and its typical settings.

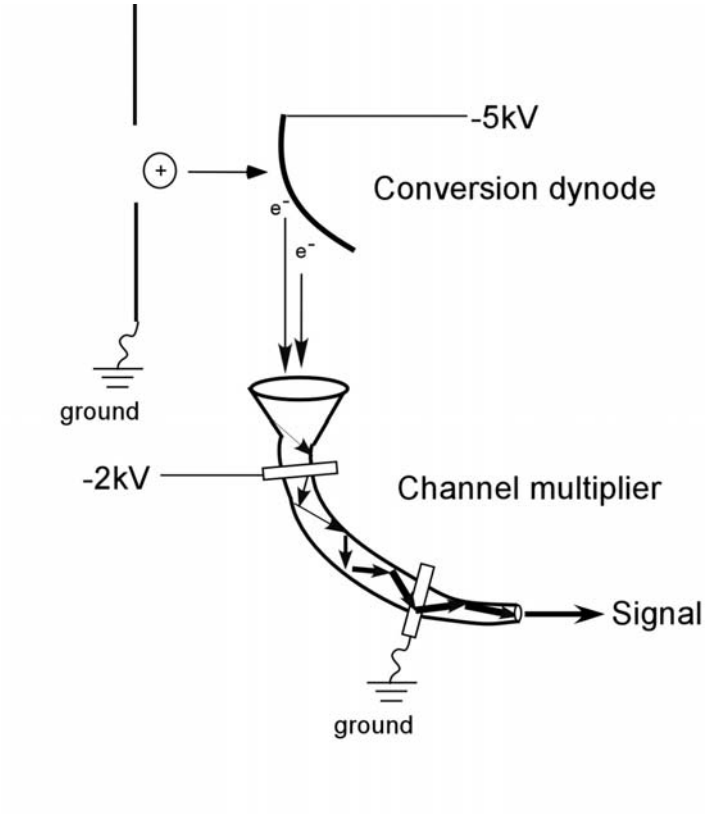

Figure 5.3 Ion detector configuration for positive ions

Ions pass an aperture in the ground shield and then hit the convention dynode which has more negative voltage than the multiplier. Secondary electrons are produced in the collisions between positive ions and the convention dynode. These secondary electrons are pushed into the channel multiplier by the high voltage between the dynode (-5 kV) and the channel multiplier funnel (-2 kV). In the channel multiplier funnel, the absolute value of voltage on the inner surface decreases along the funnel. When electrons go into the funnel, they hit the surface and generate more secondary electrons. The generated secondary electrons fly along the funnel, hit the surface more times. Each hit generates more electrons again. The process is repeated multiple times before all electrons fly out of the multiplier funnel. Then the electron current is multiplied at the

end of the channel multiplier, typically by a factor of 10^7-10^8, which is called "gain".

The following sketch shows the arrangement used for positive ion counting. The small box in the right hand side is the MTS-100 pulse amplifier. It can amplify minute pulses from electron multipliers to produce standard TTL pulse for counting applications.

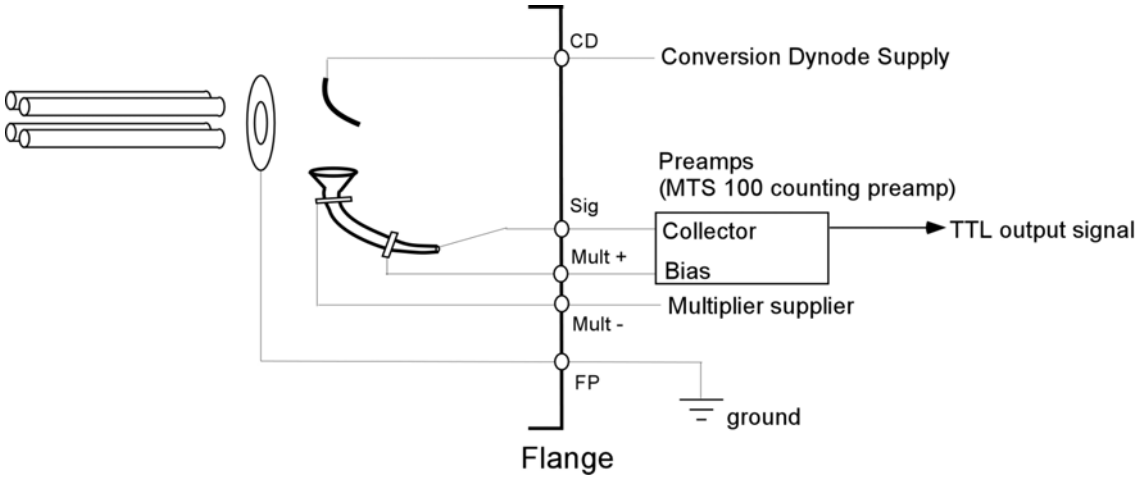

Figure 5.4 Arrangement for positive ion counting

5.3 Description of ABB Extrel QMS platform (software)

5.3.1 Problems in the software

The Merlin Automation Data System program is the user interface to set and monitor all voltages on electrostatic lenses, pole bias, dynode and multiplier *et al*. The software controls data collection, viewing and export, also it offers some data analysis tools. The problem that we have identified with the software is that it is not able to export data files correctly if the files have more than 10,000 data in every scan. If that happens, the program only exports the first 10,000 points in every data file. The second problem is that it does not export the corresponding mass information with data lists. This significantly complicates the data analysis. Yet another problem is that the software is only able to export up to 8 files every time. We often collect 300+ data files per day, so

the export of data files is quite tedious. If any mistake is made, it is difficult to trace the problem and then the entire export has to be redone. We decoded the file format and avoided these errors by writing our own data export program in Labview.

Before going further, it is useful to define the following parameters:

- Microscan scan time: the amount of time the system counts the ions at a given *m/z* value (fixed at 80 microseconds).
- Number of microscans: the number of microscans taking place over 1 amu unit. Typically, it is a number of the order of 10.
- Data point: the total ion count obtained for a given microscan.
- Scan: collection of data points for a given *m/z* range. The number of data points in a scan depends on the number of microscans and on the width of the *m/z* range.
- Scan time: the time it takes to complete one full mass range scan.
- Data file: file containing a certain number of repeated scans.

The number of microscans can be set in the software. The default setting is 50 microscans/amu. The Merlin automation has a microscan time of 80 μs/microscan which is unchangeable. For example, if we scan the mass range from 10 to 400 amu then the total scan time is $(400amu - 10amu) \times 50 \frac{microscan}{amu} \times 80 \frac{\mu s}{microscan} = 1.56s$

The scan time is the parameter that is usually changed in the software by the user. When the setting of scan time is shorter than 1.56 s in the above example, the actual number of microscans in every amu becomes lower than 50 microscans/amu. For example, if the scan time is set to be 0.3 s, then the number of microscans per amu is $\frac{(0.3s / 80\mu s / microscan)}{(400amu - 10amu)} = 9.6\ microscans / amu$. In this case, the software set the

sample per amu to be an integer, 9 microscans/amu automatically, although it still shows 50 microscans/amu in the software. Then the actual scan time is 0.28 s; it takes 0.28 s for the machine to scan from 10 amu to 400 amu once.

Usually we collect data for two minutes for each data file. In this particular case this would correspond to 2minutes/0.28s=428 scans in each data file. As the program runs, it calculates the cumulative average of a certain number of scans recorded previously (e.g., 1000) and stores all of them. The first segment of data contains the first scan. The second segment of data contains the average of the first and second scans, etc. A collection of all these averaged scans represent one data file, which is stored by the system in a binary format.

5.3.2 Data file structure

Although ABB QMS data files are not encrypted, the format of files is not open for software users to edit. Our request for the data file format was refused by the company's technical support. In order to export data files accurately and reliably, the understanding of file format and data storage was needed. A series of tests was designed in order to decipher the file structure. Specifically, many data files were collected by using Merlin automation data system software under controlled conditions. All of those data files had very small number of scans and each file only had a few non-zero data points. Some even had only one non-zero data point.

Files were read as strings in a Labview program written to read string/character from files. Every data file had several thousands of strings in the header. A large blank area with only a few non-blank strings followed the header. These non-blank strings were

believed to be data points; we converted them into numbers using different approaches until we found the approach that worked correctly.

The figure below shows the inferred structure of a Merlin (Version 0.9.4) automation data file. It has four parts. The left side shows the total size of each part, the right side shows the size of small section in some parts.

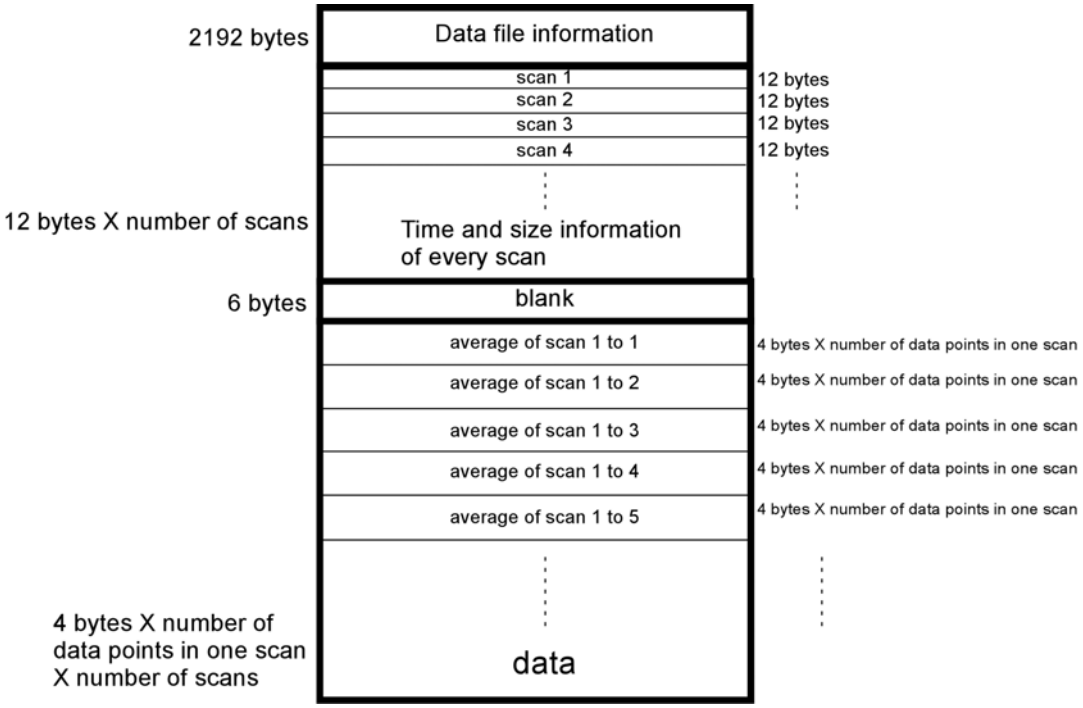

Figure 5.5 Data file structure

The first part is the header, in which some basic information is stored. The exact positions of key parameters are listed below. The total size of the header is 2192 bytes, which is constant regardless of the number of scans stored in the file. More information could be extracted from the file if needed.

The 9^{th} to 10^{th}	The number of total scans
The 757^{th} to 764^{th}	The exact time the file was created
The 1237^{th} to 1238^{th}	The number of points in every scans

The 1245th to 1252nd	Lower bound of mass range
The 1253rd to 1260th	Upper bound of mass range

Table 5.2 Critical bits containing important information in the Extrel data file

In the second part, every 12 successive bytes contain information about time and size of a corresponding scan during the collection time. The total length of this part is $the\ number\ of\ scans \times 12\ bytes$. This information can help us to find the position of data of a specific scan in the data file.

The third part is a blank with 6 bytes in length. Its function has not been identified. However, it does not affect exported data.

The last and also the most important part of the file is the actual stream of data. The number of sections in this part of the file is equal to the number of scans taken during the collection. Each section contains of the cumulative average of all the previous scans. Every data point is stored in 4 bytes, so the length of one section is data points in one scan × 4 bytes. The total size is the number of scans × data points in one scan × 4 bytes. There are no empty spaces between sections corresponding to the different scans.

The last question we need to address here is how to extract a numeric value of a data point from the 4 bytes used to store it. The method adopted by the software to transfer one four-byte bin data into decimal data is not common. It takes three steps to convert the stored information into numeric data.

The first step is to reverse the four bytes as shown in the following figure.

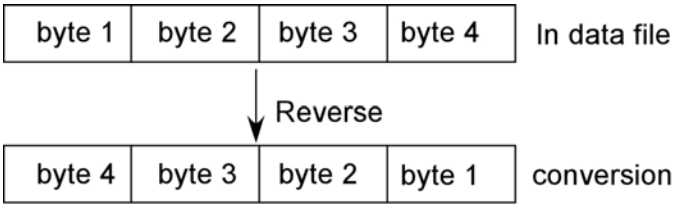

Figure 5.6, Binary data conversion

The second step is to convert the reversed bytes into a decimal number. Four bytes have 32 bits in total. The conversion requires reading 32 bits one by one and calculating the numeric value in the following way. $2^9 \times$ the value of the first bit + $2^8 \times$ the value of the second bit + $2^7 \times$ the value of the third bit+……+ $2^{-22} \times$ the value of the 32^{nd} bit. Every bit here only could be 1 or 0, because it is a binary bit.

In the final step, the number obtained in the last step is multiplied by 12,500 cps (count per second). This is necessary in order to account for the fact that the system spends 80 microseconds counting the ions at each data point. The conversion to continuous counting corresponds to $\frac{1}{80\mu s} = 12500$ cps .

5.3.1 Labview program to read data files

After painstakingly figuring out all this information, a Labview program was written to export data files. The interface is shown below.

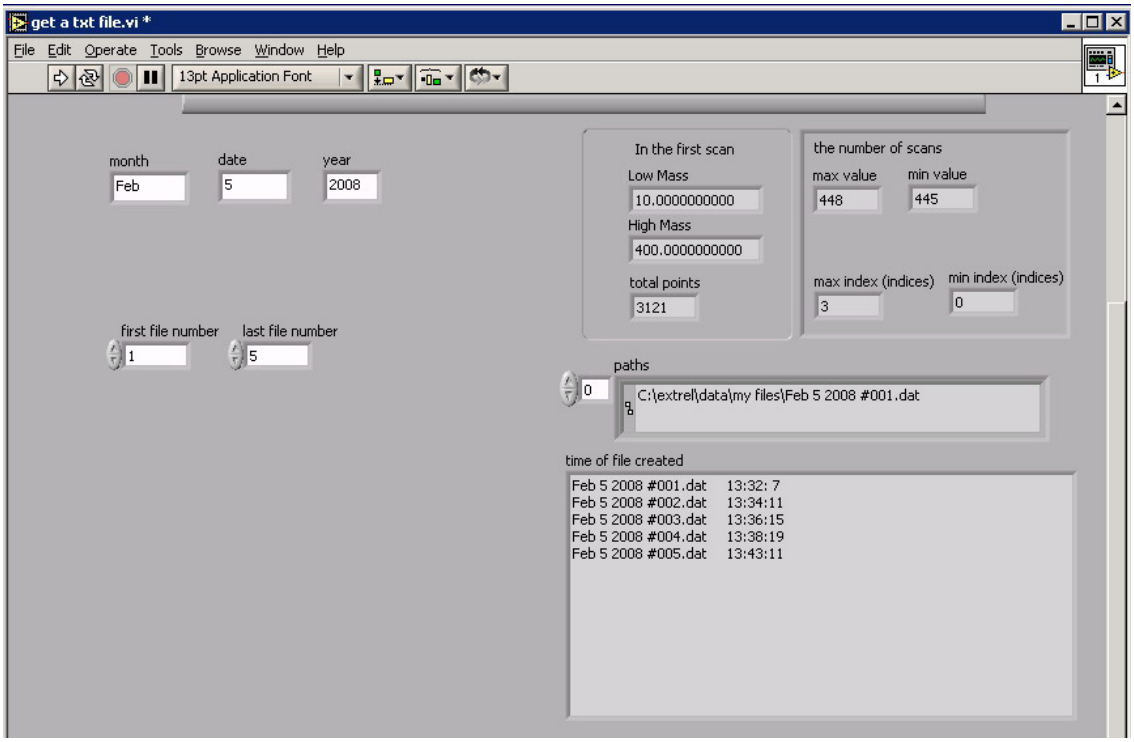

Figure 5.7 Program interface for exporting data files

On the left side, date and file information should be entered. After running, the program shows the mass range and the total number of data points in the first data file (usually all the files collected on the same day are identical). Also the program shows the maximum and minimum numbers of scans in all files and the corresponding file numbers. This information is important because the Merlin automation data system makes another kind of error that was not mentioned previously: it messes up data collection once every fifty to one hundred scans. For example, it may decide to takes 100 to 200 scans instead of 440 scans as we required, which effectively makes this file useless. The “the number of scans” could help us to locate the files having errors. Another very useful tool is the exact collection time of every data file. This information is directly coming from the data file, not from the operation system. They are listed in a box and are shown in the format

"file name+ time".

Data from all data files are written into a txt file named 'file name.txt' which is always stored on the desktop.

5.4 The arrangement of CIMS system

The following picture shows the arrangement of our CIMS system. A custom-build aluminum extrusion rack is used to install the CIMS system. The controller, Extrel QMS DC power supply and Extrel QMS power supply are installed in the lower part of the frame. The QMS is in three connected chambers which are named chamber 1, chamber 2 and chamber 3 in the sketch.

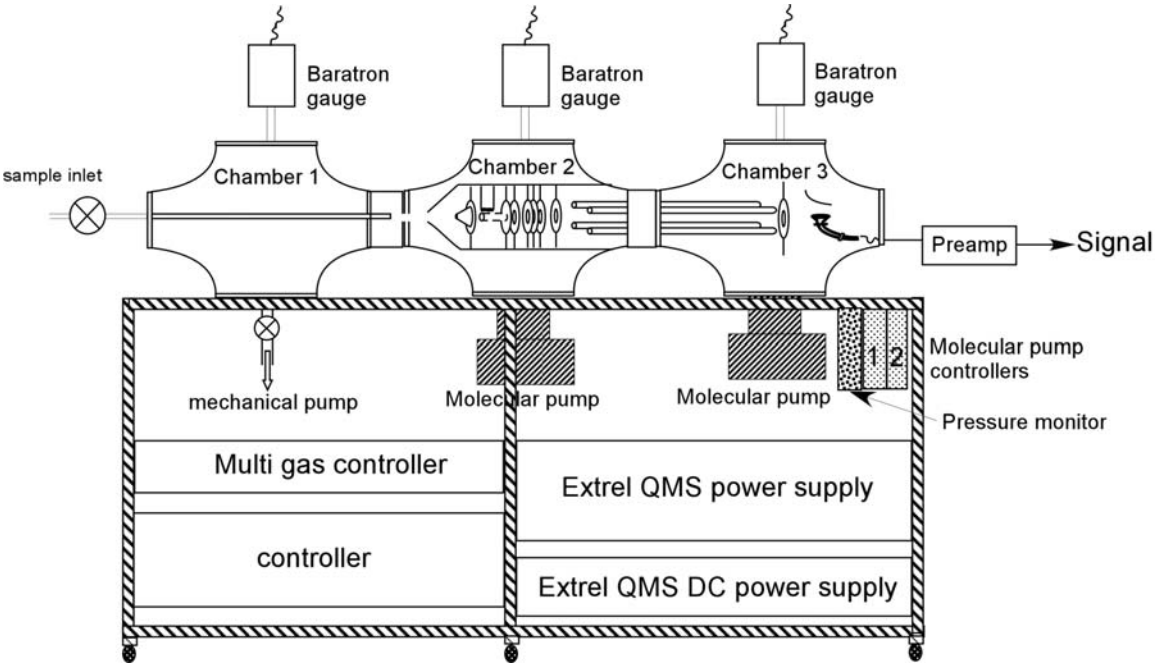

Figure 5.8 The arrangement of all components of CIMS system

A mechanical pump (Edwards Vacuum E2M80/EH500) is connected to Chamber 1. Between the mechanical pump and Chamber 1, there is a liquid N_2 trap (not shown) in

order to prevent pump oil from moving back from the pump to chamber. One 1-torr Baratron gauge (MKS) is used to measure the pressure in Chamber 1. A Baratron pressure monitor (MKS, PDR-5B, not shown) reads the pressure from the gauge. Because the external chemical ionizer is in Chamber 1, most modification on sample delivery and the ionizer were done in Chamber 1.

One molecular pump (Pfeiffer Vacuum, TC 600) is beneath Chamber 2 and another molecular pump (Pfeiffer Vacuum, TC 100) is beneath Chamber 3. The molecular pump controllers (Pfeiffer Vacuum, DCU 100 and DCU 300) installed in the right side of the rack control the settings of molecular pumps. The rotational speeds of molecular pumps are set to be 833 Hz and 1000Hz, respectively. Two diaphragm pumps (Pfeiffer Vacuum, MVP 035-2, not shown) provide the primary vacuum for the molecular pumps. Cooling circulator prevents the molecular pumps from overheating. Two pressure gauges (Pfeiffer Vacuum, PKR 261) are measuring pressures in Chamber 2 and Chamber 3. These two pressure values are displayed on the pressure monitor (Pfeiffer Vacuum, TPG262).

A 0.5 mm pinhole is installed between Chamber 1 and 2; a 0.5 mm skimmer is installed between Chambers 2 and 3. The pinhole, the skimmer, and the axial beam ionizer of the QMS system are aligned to be on the same axis. The distances are: 2 mm from the first pinhole to the skimmer and 5 mm from the skimmer orifice of the axial beam analyzer. These pinholes limit gas flows going into Chamber 2 and Chamber 3. Without any gas going into the system, the pressure in Chamber 1 is in the range between 0.02 Torr to 0.08 Torr; the pressures in Chamber 2 and Chamber 3 are 3×10^{-3} Torr and 2×10^{-7} Torr, respectively. A pressure protection was set for QMS power supply. The upper

limit for the pressure is 2×10^{-5} Torr in Chamber 3. If the pressure is higher than 2×10^{-5} Torr, the QMS power supply is turned off automatically. This limit can be changed in the molecular pump controller if needed.

Chapter VI

Development of the AP-CIMS system

6.1 Introduction

In order to explore chemistry occurring on/in aerosol particles, we first configured the mass spectrometer as a Laser Desorption-Chemical Ionization Mass Spectrometer (LD-CIMS). Later, the configuration was changed to a Thermal Desorption Chemical Ionization Mass Spectrometer (TD-CIMS). Both instrument configurations were used for investigating the mechanism of PAH/soot + ozone reactions.

Later, we shifted our focus to studying organic aerosol photochemistry, particularly on terpene-derived aerosol. For these experiments, the instrument was re-configured as an Atmospheric Pressure-Chemical Ionization Mass Spectrometer (AP-CIMS). Two different configurations of AP-CIMS were developed. In the early design, one-inlet AP-CIMS, the sample and reagent flow were mixed first, and then the mixed flow passed the radioactivity source ionizer where ions were generated. In a later (and final) design, two-inlet AP-CIMS, the sample and reagent flows were separated. More details will be given later in this chapter.

The chapter is arranged in the following way. First, we introduce the technique and explain why we choose AP-CIMS. Then, the different configurations mentioned here are discussed with examples of their applications.

6.2 Atmospheric Pressure-Chemical Ionization (APCI)

6.2.1 General introduction

The technique of chemical ionization was first introduced by Munson and Field in 1966 [102]. Now it is a common technique used to ionize neutral molecules without significant fragmentation. The chemical ionization technique evolved into several different variants including atmosphere pressure chemical ionization (APCI), which was developed first by Horning etc [103, 104].

In APCI, proton transfer reaction is the charge transfer mechanism. Usually this mechanism involves two molecules: reagent ion RH^+ acting as a proton donor and analyte M acting as a proton acceptor. Reagent precursor R, for example H_2O, can be converted to a proton donor RH^+ by various mechanisms including exposure to a radioactive source (α, β or γ particle source), electron impact or corona discharge. Then RH^+ ionizes the analyte molecule M by the proton transfer reaction.

$$RH^+ + M \rightarrow R + MH^+$$

Protons are transferred from the proton donors with lower proton affinity (PA) to proton acceptors with higher PA. The commonly used chemical reagent precursors are H_2O, NH_3 and CH_4. The choice of chemical reagents affects the selectivity of chemical ionization. For example, H_3O^+ will ionize most organic molecules except for saturated hydrocarbons. On the contrary, NH_4^+ is much more selective because of the considerably higher PA of NH_3 (854 kJ/mol) relative to H_2O (691 kJ/mol) [105]. So NH_4^+ is often used to ionize nitrogen-containing compound which usually have higher proton affinity than oxygen-containing compound.

In our AP-CIMS configurations of the mass spectrometer, a ^{63}Ni-based β source is used as the ionizer, and gaseous H_2O is used as the chemical reagent precursor. The

mechanism of ionization in this source is described below.

6.2.2 Mechanism of ionization for Ni-63 sources

The production of ions in the radioactive ionization source is relatively well understood. H_2O molecules are converted into $(H_2O)_nH_3O^+$ ions by a series of ion-molecule reactions initialized by beta particles from the ^{63}Ni element.

The radioactive half-life of ^{63}Ni is 100.1 years. The energy of the electrons emitted by ^{63}Ni ranges from 0 to 65.9 keV with an average value of 17 keV [106]. An electron emitted by ^{63}Ni collides with a carrier gas molecule, usually N_2, and forms a positive N_2^+ ion and a secondary electron. The primary electron still has high enough energy to ionize several other N_2 molecules and the secondary electrons also can ionize additional N_2 molecules. A rule of thumb is that one positive ion- thermal electron pair is produced for approximately 35 eV of the primary β-particle energy [105, 107]. An electron with 17 keV energy can produce some 500 nitrogen ions.

The formation of H_3O^+ and its clusters in N_2 and O_2 has been explored by Good et al. [108, 109] They proposed the following simplified mechanism of ionization:

$$N_2 + e^- \rightarrow N_2^+ + 2\,e^-$$

$$N_2^+ + 2N_2 \rightarrow N_4^+ + N_2$$

$$N_4^+ + H_2O \rightarrow H_2O^+ + 2N_2$$

$$H_2O + H_2O^+ \rightarrow H_3O^+ + OH$$

$$H_2O + H_3O^+ + N_2 \rightarrow (H_2O)H_3O^+ + N_2$$

$$(H_2O)_{n-1}H_3O^+ + N_2 + H_2O \rightarrow (H_2O)_n\,H_3O^+ + N_2$$

The hydrated hydronium ion $(H_2O)_nH_3O^+$ clusters are the main reagent ions in this source. At room temperature, n=2, 3, 4 are all observed, with $(H_2O)_3H_3O^+$ having the highest intensity under normal conditions. A typical background spectrum taken from our APCI-MS is shown below.

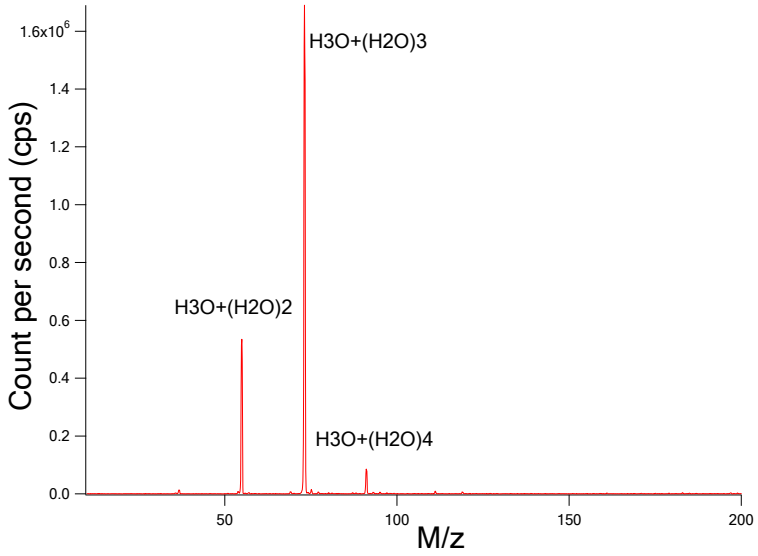

Figure 6.1 Typical background mass spectrum

Most organic chemicals, with the exception of saturated hydrocarbons, have higher proton affinities (PAs) than H_2O. For example, the PA of H_2O is 691 kJ/mole; the PA of benzene is 750.4 kJ/mole and the PA of 2-petanone is 832.7kJ/mole. Therefore, protons can be transferred from reagent ions (H_3O^+ and its clusters) to all analyte molecules including alcohols, ketones, aldehydes, carboxylic acids, and unsaturated hydrocarbons.

6.3 Mark I: Aerosol laser desorption – chemical ionization mass spectrometer

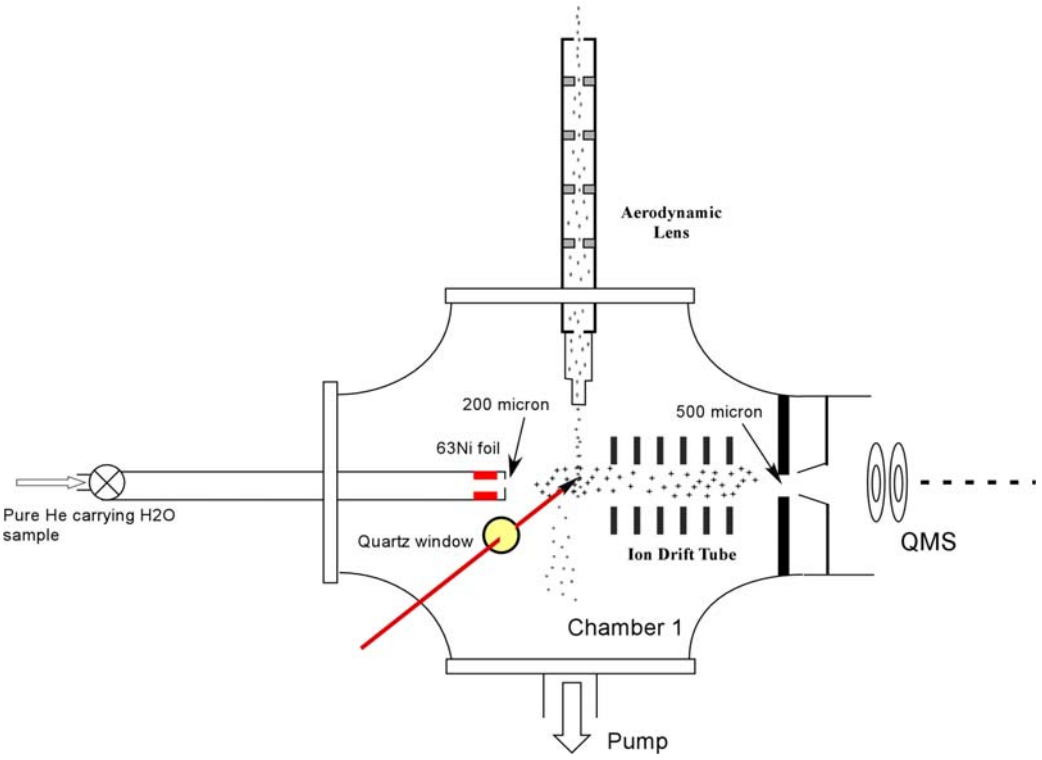

Figure 6.2 Laser desorption chemical ionization mass spectrometer

This design was used to explore the reaction between PAHs and O_3 on soot particles. The H_2O ions were generated in the ^{63}Ni ion source in the left tube and passed a 200 μm pinhole. Soot particles carrying PAHs and their oxidation products were focused by an aerodynamic lens and injected into Chamber 1. Pulsed IR light passed through a quartz window and heated the soot particles. Chemicals on soot particles were vaporized and reacted with H_3O^+ ions. The protonated organic chemicals were injected into QMS with the help from the ion drift tube. This design was abandoned because of the poor signal to noise ratio.

6.4 Mark II: Thermal desorption – chemical ionization mass spectrometer

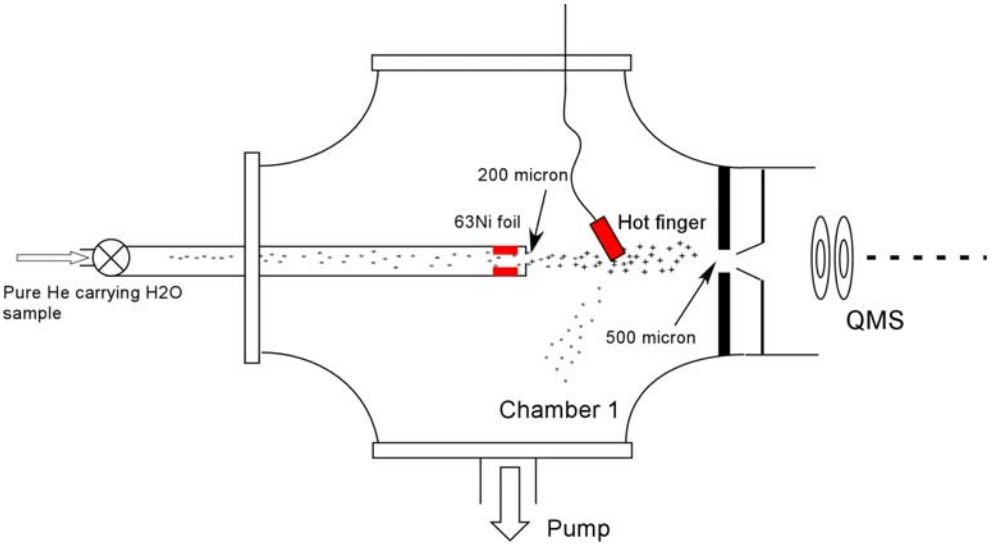

Figure 6.3 Thermal desorption chemical ionization mass spectrometer

This design was also used to explore the reaction between PAHs and O_3 on soot particles. The H_3O^+ ions were generated in the ^{63}Ni ion source in the left tube and passed a 200 μm pinhole. Soot particles carrying PAHs and their oxidation products also passed through the same 200 μm pinhole. Instead of being heated by IR radiation, soot particles were heated with a "hot finger". The evaporated organic chemicals were protonated by H_3O^+ ions. Then they went into QMS and were analyzed. This setup worked well but it had lower S/N than the in-line ionizer system described below.

6.5 Mark III: CIMS with in-line ionizer

6.5.1 Configuration

The sketch of the CIMS with in-line ionizer is shown in the following picture.

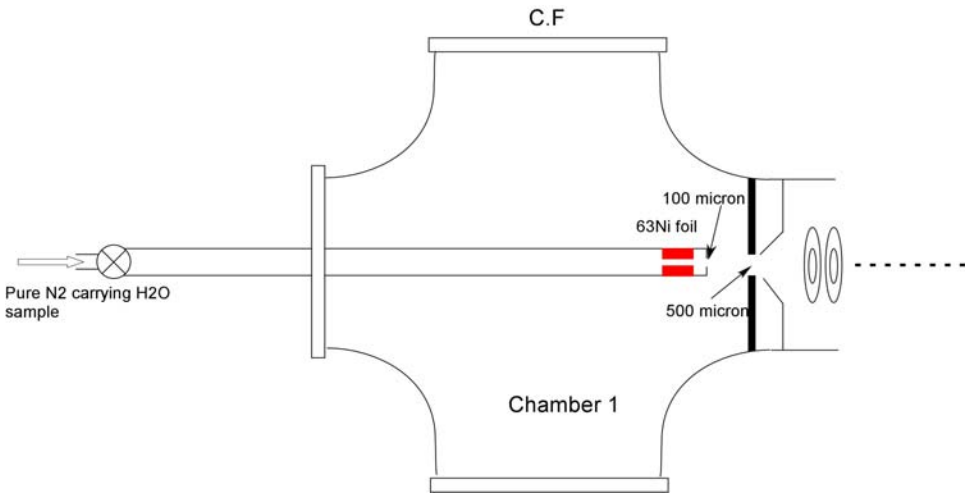

Figure 6.4 One-inlet APCI-MS configuration

Pure N_2 containing trace of water from UHP (ultra-high purity) N_2 cylinder (Airgas) mix with the sample flow first and then the mixed flow goes through the ^{63}Ni source ionizer. The sample tube is 0.5" in diameter and 50 cm in length. $(H_2O)_nH^+$ ions (n=2 to 5) are produced in the ionizer after a series of reactions initialed by the electron impact on N_2. At the same time, the proton transfer reactions are also happening in the same region. Protons are transferred from $(H_2O)_nH^+$ to analyte molecules. After the proton transfer reactions, cluster reactions may also happen. If the analyte molecule is A, then the final products might be $A_m(H_2O)_nH^+$, where m and n are small integers. Then all molecules and ions pass a calibrated 100 μm pinhole to go into chamber one. After several mm of travel, ions are guided into the QMS through a 500 μm orifice by the voltage on the skimmer behind the orifice. The opening on the skimmer is 500 μm.

Under typical operation condition, the flow rate is between 50 and 80 sccm, corresponding to 450 to 750 Torr in the tube. The pressure in the main chamber is between 0.35 Torr and 0.48 Torr and the pressure in chamber 3 is between 3.5×10^{-6} Torr

and 5×10^{-6} Torr.

I should mention that after being used for four years, the ^{63}Ni ring expanded a little bit and now it cannot be taken off from the source holder. The sketch is shown below. The red part is the ^{63}Ni ring.

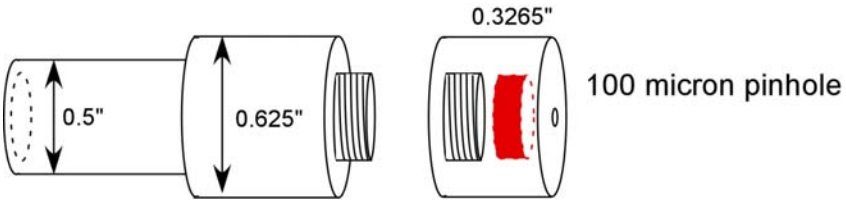

Figure 6.5 β-source in a stainless steel holder

6.5.2 Kinetics in the in-line ionizer

In this section, ionization chemistry in the source is simulated in order to understand sensitivity, selectivity, and dynamic range of this source.

6.5.2.1 Production of $(H_2O)_nH^+$ ions in the in-line ionizer

The inner diameter of the ^{63}Ni ring is D= 0.235 inch and the length is L= 0.165 inch. So the inner volume of the source is V= 0.117 cm^3. The initial radioactivity is 15 mCi (1 mCi = 3.7×10^7 Bq). The average energy of electrons emitted from ^{63}Ni is W= 17 keV, as mentioned above. One positive ion-thermal electron pair is produced per each 35 eV of the electron energy. We estimate that the upper limit for the ion pair production rate is

$$S= \frac{15\ \text{mCi}\times17\ \text{keV}}{35\ \text{eV}} = 2.2\times10^{12}\ \#/\text{cm}^3 .$$

Electrons hit N_2 and form N_2^+ ions, then N_3^+ and N_4^+ are formed. Since the

formation of N_3^+ and N_4^+ is very fast at atmospheric pressure [110], they could be treated as the direct products of ionization. When O_2 is present in the carrier gas, the situation is much more complicated because negative ions O_2^- could be formed [111]. Since we do not use air or O_2 as carrier gas, the negative ions except for thermal electrons are not considered in the following discussion.

The loss mechanism for the ions is complicated. Only three major factors are considered here similarly to what other researchers did [107, 112]. The major loss pathways are recombination of positive ions and thermal electrons, loss of ions on walls by diffusion, and ions physically leaving the source with the gas flow. The recombination rate is in the order of 10^{-7} $cm^3s^{-1}molecule^{-1}$ for non-cluster ions and 10^{-6} $cm^3s^{-1}molecule^{-1}$ for cluster ions. The recombination rates are assumed to 2×10^{-6} $cm^3s^{-1}molecule^{-1}$ for N_4^+ and thermal electrons [113] and 6.5×10^{-6} $cm^3s^{-1}molecule^{-1}$ for $H^+(H_2O)_n$ and thermal electrons [114].

The loss on the walls by diffusion for ion $X^{\pm}$ is $\frac{D}{<r^2>}[X^{\pm}]$ [107]. D is the diffusion coefficient of $X^{\pm}$. $<r^2>$ depends on the ionizer geometry [115]; it is equal to $0.092r^2$ in our cylindrically symmetric case. In the one-inlet AP-CIMS, due to the high production rate of thermal electrons, the gas in the ionizer is in plasma condition, which means the total concentration of positive ions is equal to the total concentration of negative ions and thermal electrons (see discussion in [115]). The thermal electron diffusion coefficient is 50 cm^2s^{-1} at the atmospheric pressure. But under the plasma condition, this coefficient decreases dramatically due to the force between positive ions and thermal electrons [107]. On the contrary, the diffusion coefficients of positive ions increase for the same reason. The result is that the effective diffusion coefficient of

positive ions and thermal electrons are same under plasma condition [112]. The diffusion coefficients for all ions are taken to be 0.1 cm^2s^{-1} as other researcher commonly assumed [112].

The last major loss is ions physically leaving the tube through the exit pinhole. It is equal to $\frac{F}{V}[X^{\pm}]$, in which F is flow rate, V is ionizer volume. It is same for all ions and thermal electrons.

The other assumption we need to make is the H_2O concentration (it cannot be easily measured inside the ionizer). Based on the equilibrium ratio between $(H_2O)_4H^+$ and $(H_2O)_3H^+$ in our mass spectra, H_2O concentration is estimated to be 1.5×10^{14} #/cm^3. The exact amount of water vapor is hard to control in this instrument; fortunately it is not too important as long as it is constant.

In the presence of water vapor, all positive charges are transferred from N_3^+ and N_4^+ to H_2O. H_3O^+ ions are formed in the following reactions. The reaction rates are close to ion-molecule collision rates [116]. OH radical byproducts are lost on the walls.

$$N_4^+ + H_2O \rightarrow H_2O^+ + N_2 + N_2 \qquad k = 2\times10^{-9}\,cm^3s^{-1}molecule^{-1}$$
$$H_2O^+ + H_2O \rightarrow H_3O^+ + OH \qquad k = 1.8\times10^{-9}\,cm^3s^{-1}molecule^{-1}$$

It is assumed that H_3O^+ ions are generated from N_4^+ directly and the reaction rate is 2×10^{-9} $cm^3s^{-1}molecule^{-1}$.

The steady state equations for the concentrations of reactive species in the ionizer are

$$\frac{d[N_4^+]}{dt} = 0 = S - k_1[N_4^+][e^-] - k_2[H_2O][N_4^+] - \frac{D_{N_4^+}}{<r^2>}[N_4^+] - \frac{F}{V}[N_4^+] \quad (1)$$

$$\frac{d[e^-]}{dt} = 0 = S - k_1[N_4^+][e^-] - k_3[(H_2O)H^+][e^-] - \frac{D_{e^-}}{<r^2>}[e^-] - \frac{F}{V}[e^-] \quad (2)$$

$$\frac{d[(H_2O)H^+]}{dt} = 0 = k_2[H_2O][N_4^+] - k_3[(H_2O)H^+][e^-] - \frac{D_{(H_2O)H^+}}{<r^2>}[(H_2O)H^+] - \frac{F}{V}[(H_2O)H^+] \quad (3)$$

k_1, k_2 and k_3 are the bimolecular reaction rate constants between species standing next to them. As discussed above, $k_1=2\times10^{-6}$ $cm^3s^{-1}molecule^{-1}$, $k_2= 2\times10^{-9}$ $cm^3s^{-1}molecule^{-1}$ and $k_3=6.5\times10^{-6}$ $cm^3s^{-1}molecule^{-1}$

Calculations were done with Mathematica v6.0. The calculation results show that both of H_3O^+ and thermal electron concentrations are around 5.5×10^8 #/cm^3 and N_4^+ concentration decreases to less than 5% of H_3O^+ at all relevant values of N_2 flow rates. Based on this result, the total number of H_3O^+ ions leaving the tube, $\frac{F}{V}[(H_3O)^+]$, is directly proportional to the flow rate F.

To verify this prediction, the following experiment was done. With increasing N_2 flow rate from 10 mL/minute to 50 mL/minute, the pressure in the ionizer increased from 146 Torr to 548 Torr. The water signal in mass spectra also increased. The result is shown in Fig 6.6

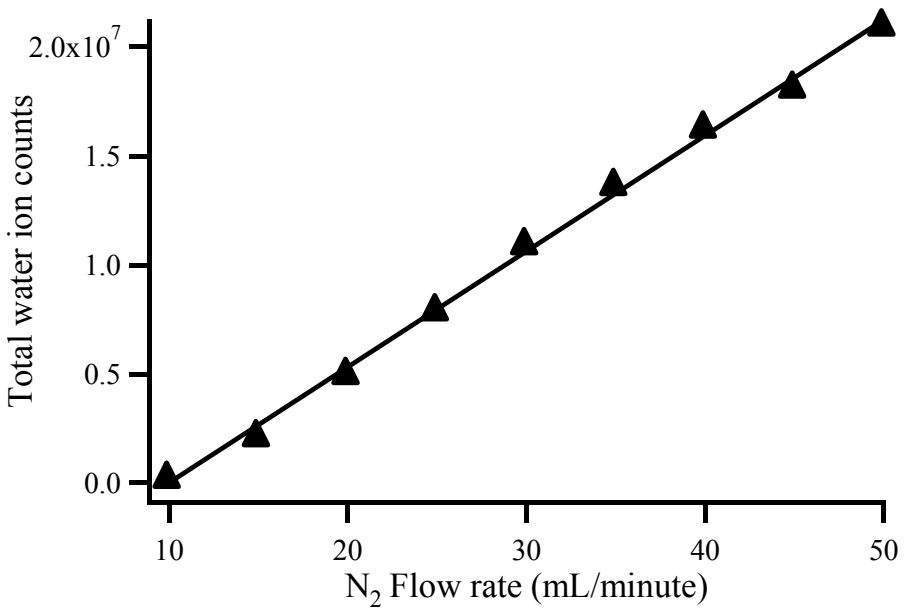

Figure 6.6 total water ion counts vs. N_2 flow rate

It shows that the total water ion count is proportional to the N_2 flow rate. This result is consistent with the conclusion from the kinetic simulation.

6.5.2.2 Proton transfer reaction in the ionizer

Let us assume that an analyte molecule A is sent into the ionizing volume and the proton transfer reaction is $(H_2O)H^+ + A \rightleftarrows AH^+ + H_2O$. The steady state equation for AH^+ is

$$\frac{d[AH^+]}{dt} = 0 = k_4[(H_2O)H^+][A] - \frac{k_4}{K}[H_2O][AH^+] - k_5[AH^+][e^-] - \frac{D_{H^+A}}{< r^2 >}[AH^+] - \frac{F}{V}[AH^+] \quad (4)$$

So $$\frac{[AH^+]}{[(H_2O)H^+]} = \frac{k_4[A]}{k_5[e^-] + \frac{D_{AH^+}}{< r^2 >} + \frac{F}{V} + \frac{k_4}{K}[H_2O]} \quad (5)$$

k_4 is the reaction rate constant between $(H_2O)H^+$ and A, and k_5 is the reaction rate constant between $[AH^+]$ and $[e]$. K is the equilibrium constant for reaction $(H_2O)H^+ + A \rightleftarrows AH^+ + H_2O$. The terms $k_5[e^-], \frac{D_{AH^+}}{<r^2>}, \frac{F}{V}, \frac{k_4}{K}[H_2O]$ represent the AH^+ loss due to recombination with thermal electrons, diffusion on the wall, exiting the tube and reverse reaction with H_2O respectively. The relative magnitude of these terms decides which physical process controls the instrument sensitivity and linear range.

Estimated K values for several small chemicals are shown in the following table. They are calculated from $K = e^{-\Delta G/RT}$. K1, K2, K3 and K4 correspond to n=1, 2, 3, 4 in the reactions $(H_2O)_n H^+ + A \rightleftarrows A(H_2O)_{n-1}H^+ + H_2O$. The necessary thermodynamics data come from [117].

A	K1	K2	K3	K4	K5
CH_3OH	1.19E+11	9.28E+06	2.67E+05	7.71E+03	6.51E+03
C_2H_5OH	9.16E+14	1.47E+09	5.59E+06	6.93E+04	3.53E+04
n-C_3H_7OH	5.27E+16	2.60E+10	2.56E+07	9.13E+03	5.17E+02
CH_3CHO	3.70E+13	1.38E+08	4.17E+04	2.98E+04	2.51E+04
$(CH_3)_2O$	4.73E+17	1.00E+11	6.22E+05	6.51E+03	2.36E+03
$(CH3)_2CO$	1.57E+21	6.84E+12	2.16E+07	2.26E+05	6.93E+04
CH_3COOH	1.62E+16	2.30E+08	2.26E+05	1.69E+03	1.02E+03

Table 6.1 Calculated equilibrium constants (in unit of atm^2/atm^2 = dimensionless)

Table 6.1 shows that all *K1* values are much higher than 1000. So in equation (5), $k_5[e^-] >> \frac{D_{AH^+}}{<r^2>}$, $\frac{F}{V}$ and $\frac{k_4}{K}[H_2O]$. This physically means that the recombination reaction dominates the loss of AH^+ ions. This results in $\frac{[AH^+]}{[(H_2O)H^+]} \approx \frac{k_4[A]}{k_5[e^-]}$ from equation (5).

Under the plasma condition, [positive ions] = [negative ions], or

$$[AH^+]+[(H_2O)H^+]=[e^-] \qquad (6)$$

Combining these results together gives $\frac{[AH^+]}{[(H_2O)H^+]} \approx \frac{k_4}{k_5}\frac{[A]}{[AH^+]+[(H_2O)H^+]}$.

Therefore, when $[AH^+] < 0.1[(H_2O)H^+]$, we can get

$$[AH^+] \approx \frac{k_4}{k_5}[A] \qquad (7)$$

Equation (7) shows that the ratio $[AH^+]$ is approximately linear with respect to the analyte molecule concentration $[A]$ when $[AH^+] < 0.1[(H_2O)H^+]$. The sensitivity highly depends on the recombination rate constant of the reaction between $[AH^+]$ and thermal electrons. For molecules which do not form clusters with H_2O or itself at room temperature, the recombination rates are usually ten times slower than the corresponding rates for clusters. This improves the detection sensitivity.

6.5.2.3 Proton transfer reaction including H_2O cluster formation in the ionizer

In reality, both of H_2O molecule and A molecules can form water clusters, which can not be neglected.

$$(H_2O)_{n-1}H^+ + H_2O \overset{M}{\rightleftarrows} (H_2O)_n H^+ \qquad (8)$$

The forward three-body reaction rate constant is of the order of 10^{-27} $cm^6 molecules^{-2} s^{-1}$ [108]. It is close to ternary ion-molecule collision rate at atmosphere pressure. That implies that water clusters are always in an equilibrium state since $[H_2O]$ is always much higher than the thermal electron concentration. Suppose K_{water_n} is the equilibrium constant.

$$\frac{[(H_2O)_n H^+]}{[(H_2O)_{n-1} H^+]} = K_{water\_n}[H_2O] \qquad (9)$$

Equation (9) shows that the ratio between $[(H_2O)_nH^+]$ and $[(H_2O)_{n-1}H^+]$ only depends on $[H_2O]$. Therefore, we can write

$$[(H_2O)_n H^+] = C_n \times \sum_n [(H_2O)_n H^+] \qquad (10)$$

Where C_n is a coefficient depending on $[H_2O]$ and equilibrium constants between H_2O clusters. Since $[H_2O]$ is constant under typical operation condition and all K_{water_n} are constants, the values of C_n can be viewed as constants. Then Equation (10) means the ratio between $[(H_2O)_nH^+]$ and total H_2O ion cluster concentration $\sum_n[(H_2O)_nH^+]$ is constant.

For an analyte molecule A which can form clusters with several H_2O molecules, the reactions are similar:

$$A(H_2O)_{n-1}H^+ + H_2O \rightleftarrows A(H_2O)_n H^+ \qquad (11)$$

The equilibrium between clusters is likely to always exist in the ionizer per above discussion. So $[(H_2O)_n AH^+] = b_n \times \sum_n [(H_2O)_n AH^+]$, where b_n is a constant for a given set of the experimental conditions. Figure 6.7 shows the generation and removal of ion $A(H_2O)_{n-1}H^+$. Because of the unchanged ratios between the A ion clusters, the generation and removal of $A(H_2O)_{n-1}H^+$ via $A(H_2O)_{n-1}H^+$ and $A(H_2O)_{n-1}H^+$ reactions can be neglected. They will not be included in the following discussion.

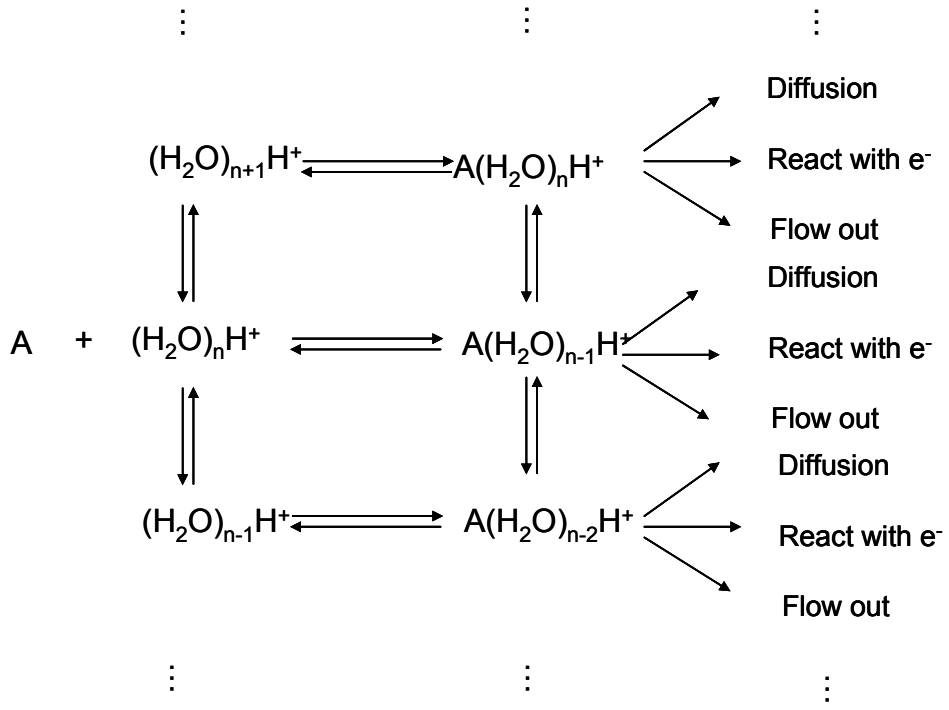

Figure 6.7 The generation and removal routes of A ion clusters

Now consider the related reaction

$$(H_2O)_n H^+ + A \rightleftarrows (H_2O)_{n-1} AH^+ + H_2O \qquad (12)$$

Suppose k_{4_n} is the forward reaction rate constant, K_n is the equilibrium constant for the equation (12) and k_{5_n} is the recombination rate coefficient of reaction between $[(H_2O)_{n-1} AH^+]$ and $[e^-]$. So the steady state equation for ion $(H_2O)_{n-1} AH^+$ is

$$\frac{d[(H_2O)_{n-1} AH^+]}{dt} = 0 = k_{4\_n}[(H_2O)_n H^+][A] - \frac{k_{4\_n}}{K_n}[H_2O][(H_2O)_{n-1} AH^+] - k_{5\_n}[(H_2O)_{n-1} AH^+][e^-]$$
$$- \frac{D_{(H_2O)_{n-1} AH^+}}{< r^2 >}[(H_2O)_{n-1} AH^+] - \frac{F}{V}[(H_2O)_{n-1} AH^+] \qquad (13)$$

The dominant process for the $(H_2O)_{n-1} AH^+$ loss is still the recombination between $(H_2O)_{n-1} AH^+$ and thermal electrons. Therefore,

$$\frac{\sum_n [(H_2O)_n AH^+]}{[A]} \approx \sum_n \frac{k_{4\_n}[(H_2O)_n H^+]}{k_{5\_n}[e^-]} \qquad (14)$$

Now the sensitivity is:

$$\sum_n [(H_2O)_n AH^+] \approx \sum_n \frac{k_{4\_n}[H^+(H_2O)_n][A]}{k_{5\_n}[e^-]} = \sum_n \left(\frac{k_{4\_n}C_n}{k_{5\_n}} \times \frac{\sum_n [H^+(H_2O)_n][A]}{[e^-]}\right)$$
$$= C\frac{\sum_n [H^+(H_2O)_n][A]}{[e^-]} \qquad (15)$$

Coefficient C= $\sum_n \left(\frac{k_{4\_n}}{k_{5\_n}} C_n\right)$, which is constant when [H_2O] is constant.

Under plasma condition, we have [positive ions]=[negative ions], so

$$\frac{\sum_n [(H_2O)_n AH^+]}{\sum_n [(H_2O)_n H^+]} \approx C \times \frac{[A]}{\sum_n [H^+(H_2O)_n] + \sum_n [H^+A(H_2O)]} \qquad (16)$$

This result is consistent with the case that no water cluster is formed, which is discussed in the previous section. When $\sum_n [H^+A(H_2O)] < 0.1 \sum_n [H^+(H_2O)_n]$, $\sum_n [A(H_2O)_n H^+] \approx C \times [A]$. In other words, if the analyte concentration is not too large, the total intensity for sum of all ions derived from A is directly proportional to the concentration of A. This proportionality breaks down when the analyte concentration is so high that it efficiently competes with H_2O for the available protons.

6.5.2.4 Proton transfer reaction including A cluster formation in the ionizer

Now we consider a scenario when the analyte molecule A is capable of forming

dimer ions A_2H^+. Then, for reaction $A + AH^+ \rightleftarrows A_2H^+$, let k_d be the forward reaction rate constant, K_d be the equilibrium constant and k_{de} be the recombination reaction coefficient. The steady state equation is:

$$\frac{d[A_2H^+]}{dt} = 0 = k_d[AH^+][A] - \frac{k_d}{K_d}[A_2H^+] - k_{de}[A_2H^+][e^-] - \frac{D_{A_2H^+}}{< r^2 >}[A_2H^+] - \frac{F}{V}[A_2H^+]$$

(17)

$$\frac{d[AH^+]}{dt} = 0 = k_4[(H_2O)H^+][A] + \frac{k_d}{K_d}[A_2H^+] - k_d[AH^+][A] - \frac{k_4}{K}[H_2O][AH^+] - k_5[AH^+][e^-] - \frac{D_{H^+A}}{< r^2 >}[AH^+] - \frac{F}{V}[AH^+]$$

(18)

So
$$\frac{k_{de}[A_2H^+] + k_5[AH^+]}{[A]} \approx \frac{k_4[(H_2O)H^+][A]}{[(H_2O)H^+] + [(H_2O)AH^+] + [(H_2O)A_2H^+]}$$

(19)

This result shows that when A forms dimer ions, the sensitivity is highly dependant on the recombination rate constants of reactions between thermal electron and A monomer and dimer. When the recombination rates are very different for dimer and monomer, the linearity of detection would suffer. The linearity of monomer exists when dimer concentration is much lower than monomer concentration.

6.5.3 Instrument calibration

To investigate the linearity of detection experimentally, this AP-CIMS was calibrated by using ^{13}C labeled acetone (molecular weight = 61 g/mol) mixed in UHP N_2. The reason that we chose acetone as the calibration molecule is that acetone is one of known products of limonene SOA photolysis. The experimental setup is shown below.

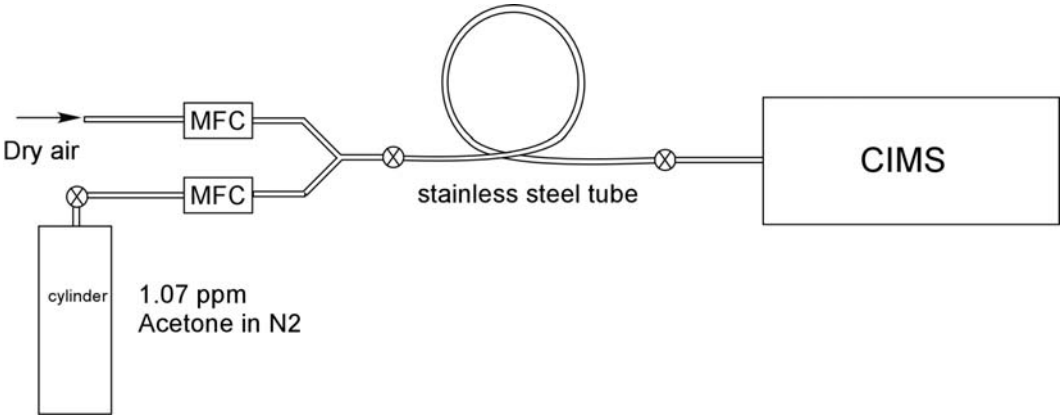

Figure 6.8 Experiment setup for the AP-CIMS instrument calibration

^{13}Acetone was mixed with UHP (Ultra-High Purity) N_2 (AirGas) in a cylinder. The concentration of ^{13}Acetone was 1.07 ppm. The flow was mixed with a dry air flow in a stainless steel tube. The acetone flow rate was from 2 sccm to 100 sccm and the dry air flow was 20 L/min. Then the mixed flow went into the CIMS instrument. Two flows were controlled by mass flow controllers precisely so that accurate acetone concentrations could be known.

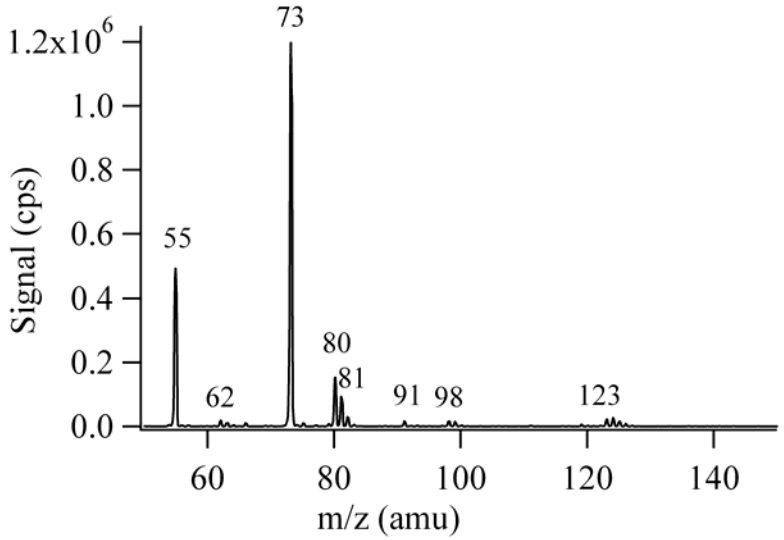

Figure 6.9 Sample spectrum of acetone

One of the sample spectra is shown in figure 6.9. The acetone concentration was 1.2 ppb. Peaks at 55, 73 and 91 *m/z* are water clusters $H^+(H_2O)_n$, n=3,4,5. Peaks at 62 and 80 and 98 m/a are ^{13}acetone monomers AcH^+, $Ac(H_2O)H^+$ and $Ac(H_2O)_2H^+$ respectively; peak at 123 *m/z* is protonated ^{13}acetone dimer $(Ac)_2H^+$. No peaks above 150 *m/z* were found. The remaining peaks (63, 81, 99, 125 *m/z*) belong to impurity Dimethyl Sulfide (DMS, MW: 62). The existence of this impurity does not affect the overall conclusions of this linearity test.

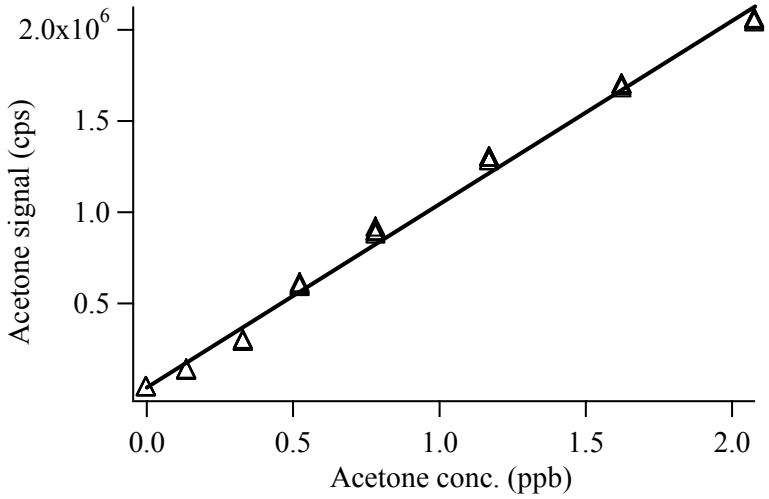

Figure 6.10 Sample calibration for C-13 acetone

The calibration result is shown in the above figure. The y axis is the total acetone monomer signal including $(Ac)(H_2O)_nH^+$, n=0, 1, 2, 3. The line is a linear fit to the acetone signal/water signal ratio. When acetone concentration was 2 ppb, the total water ion signal dropped by as much as 40%. However, the acetone ion signal/water ion signal ratio remained linear with respect to the acetone concentration, which is consistent with our kinetics simulations. Above 2 ppb, the acetone dimer yield became substantial, and the signal linearity broke down. The detection limit in this particular case is 1 ppt. (this

corresponds to the mixing ratio at which the observed signal is equal to 3 times the root mean square deviation for the background noise). This detection limit is better than or comparable to that in the CIMS research literature.

6.5.4 Issues with the one-inlet AP-CIMS

From the above discussion, the linearity and sensitivity of the instrument are strongly affected by the formation of dimer ions in a one-inlet source configuration. Also, in one-inlet AP-CIMS the 100μm pinhole was very easy to clog with organic deposits from the analyte flow. In earlier designs of AP-CIMS by [104, 118], heating tape was used to maintain the whole ion source at high temperature between 250°C to 400°C. Heating the source also helped to reduce cluster formation. But we do not take this approach as it might lead to ^{63}Ni source damage [119], especially in experiments when O_3 is present in the analyte flow. Also N_2^+ ions can attack sample molecules and transfer positive charge to sample molecules directly causing fragmentation. For these reasons, the AP-CIMS was modified to a two-inlet configuration in order to avoid these problems.

6.6 Mark IV: CIMS with in-line ionizer

6.6.1 Configuration

The sketch of the two-inlet AP-CIMS is shown in Fig. 6.11. The layout of the two-inlet AP-CIMS is very similar to that of the one-inlet AP-CIMS except that the sample line and reagent line are now separated.

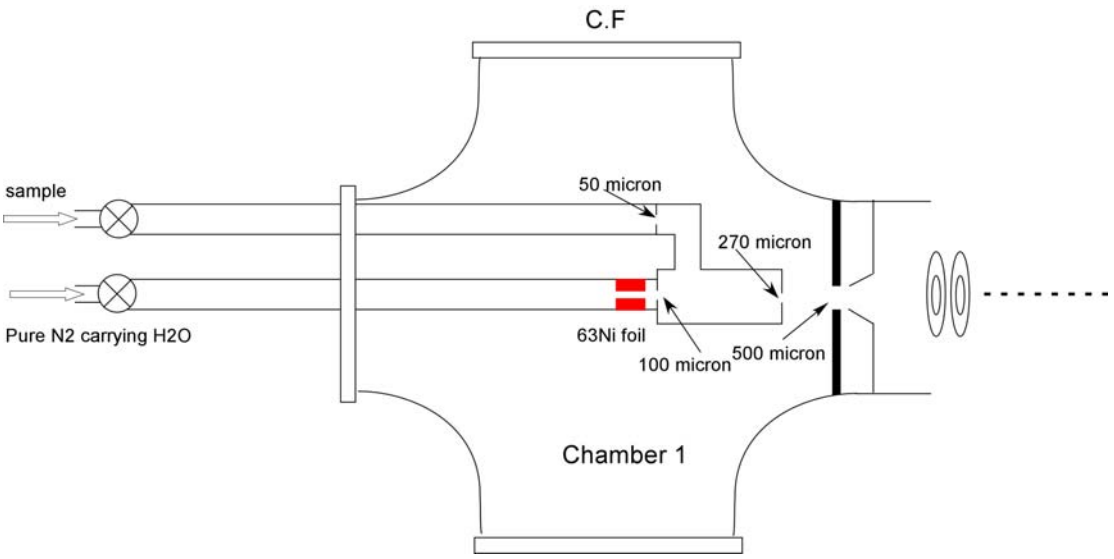

Figure 6.11 Two-inlet APCIMS

Trace H_2O molecules in UHP N_2 are ionized in the ^{63}Ni ion source and all water cluster ions pass through a 100 μm pinhole. The sample flow goes through a parallel tube and passes through a 50 μm pinhole. The small size of this pinhole allows direct sampling from an atmospheric pressure. Proton transfer reactions happen in a short tube where these two flows mix. It is 5 cm in length and its inner diameter is 0.5 cm. After the reactions, all molecules and ions exit through a 270 μm pinhole and then pass through a 500 μm orifice into the QMS.

Under normal operation conditions, the N_2/H_2O flow ranges from 20 to 30 sccm, corresponding to 250 to 350 Torr in the tube; the sample flow is 20 sccm and the pressure in the sample line is 750 Torr. The pressure in the ion region is not measured directly but it can be estimated. It ranges from 47 Torr to 58 Torr for N_2/H_2O flow is from 20 to 30 sccm. The residence time in the ionization region is 0.35 s, which is relatively independent of the N_2 and sample flow are. The pressure in Chamber 1 is between 0.25 to 0.35 Torr under typical conditions of operation. The resulting pressure in Chamber 3 is

2.5×10^{-6} to 3×10^{-6} Torr.

6.6.2 Kinetics in the proton transfer region

6.6.2.1 Proton transfer reaction in the ionizer

Since the ion source is the same as in one-inlet configuration, the initial water cluster ion concentration injected in the ionization region is same as the previous part. The concentration is about 5×10^{8} ions/cm^3 and the flow rate is 0.7 cm^3/s (referenced to the standard conditions). The amount of H_2O ions going into the proton transfer tube is a constant. Because the plasma condition no longer applies in the proton transfer tube, the electron diffusion coefficient is several hundred times larger than that for positive ions. This means that thermal electrons are lost very quickly. For simplicity, thermal electron concentration in the proton transfer region can be assumed to be zero. The other assumptions are all same as the ones in section 6.5.2.1.

Let K be the equilibrium constant for reaction $(H_2O)H^+ + A \leftrightarrow AH^+ + H_2O$; k_1 be the rate constant of reaction between $(H_2O)H^+$ and A; the reverse reaction rate constant is then k_1/K. The steady state equations for $[AH^+]$ and $[(H_2O)H^+]$ are:

$$\frac{d[AH^+]}{dt} = 0 = k_1[(H_2O)H^+][A] - \frac{k_1}{K}[H_2O][AH^+] - \frac{D_{AH^+}}{<r^2>}[AH^+] - \frac{F}{V}[AH^+] \quad (20)$$

$$\frac{d[(H_2O)H^+]}{dt} = 0 = S - k_1[(H_2O)H^+][A] + \frac{k_1}{K}[H_2O][AH^+] - \frac{D_{(H_2O)H^+}}{<r^2>}[(H_2O)H^+] - \frac{F}{V}[(H_2O)H^+] \quad (21)$$

In these equations, D_{AH^+} and $D_{(H_2O)H^+}$ are diffusion coefficient of two ions in the proton transfer tube; $<r^2>$ is the geometric factor for diffusion, $<r^2> = \frac{1}{(\frac{2.405}{r})^2 + (\frac{\pi}{L})^2} = 0.17r^2$ [115]; V is volume; F is the flow rate in the proton

transfer tube. Taking D_{HA^+} =0.05 cm^2/s at atmospheric pressure, the following values are obtained at 47 Torr: $\frac{D_{HA^+}}{< r^2 >} \approx \frac{0.05}{0.17 \times 0.5^2} \times \frac{760}{47} = 19$, and $\frac{F}{V} \approx \frac{10.8}{3.6} = 3$.

According to the kinetic theory, diffusion coefficients for ions in N_2 are proportional to $(\frac{1}{m_{N_2}} + \frac{1}{m_{ion}})^{1/2}$, $\frac{1}{collision\ cross\ section}$ and $\frac{1}{pressure}$ [115]. When molecular (or ionic) weights are much larger than that for N_2, the diffusion coefficients are all similar. We assume that all ion diffusion coefficients are about 0.05cm^2/s at one atmosphere pressure.

From the above equations, we can get $\frac{[AH^+]}{[(H_2O)H^+]} = \frac{k_1[A]}{\frac{k_1}{K}[H_2O] + \frac{D_{HA^+}}{< r^2 >} + \frac{F}{V}}$. We conclude that the ratio of [AH^+] to [H_3O^+] should be directly proportional to the concentration of analyte A under our experimental conditions.

6.6.2.2 Proton transfer reaction including H_2O cluster formation in the ionizer

Now let us complicate the situation somewhat by taking into account the fact that both A and H_2O ions can form protonated clusters with H_2O.

$$(H_2O)_{n-1}H^+ + H_2O \rightleftarrows (H_2O)_n H^+ . \qquad (22)$$

Once again, the equilibrium constant is K_{w_n}, and it is cluster size dependent. Since the reverse reaction rate is high relative to the physical removal of ions by the flow, an equilibrium quickly establishes in the proton transfer tube, $K_{w\_n} = \frac{[(H_2O)_n H^+]}{[(H_2O)_{n-1}H^+][H_2O]}$.

If there are no sample molecules present, and only H_2O ions exist in the proton transfer tube we can write:

$$\frac{d[(H_2O)_nH^+]}{dt} = 0 = S - k_{n-1}[(H_2O)_{n-1}H^+][H_2O] + \frac{k_{n-1}}{K_{w\_n}}[(H_2O)_nH^+]$$
$$- \frac{D_{(H_2O)_nH^+}}{< r^2 >}[(H_2O)_nH^+] - \frac{F}{V}[(H_2O)_nH^+] \qquad (23)$$

$$\sum_n \frac{d[(H_2O)_nH^+]}{dt} = 0 = S - (\frac{D_{H_2O\ ion}}{< r^2 >} + \frac{F}{V})\sum_n [(H_2O)_nH^+] \qquad (24)$$

S is the total H_2O ions supply from the ionizer. Equation (24) can be rearranged as follows:

$$\sum_n [(H_2O)_nH^+] = \frac{S}{(\frac{D_{H_2O\ ion}}{< r^2 >} + \frac{F}{V})}. \qquad (25)$$

In addition, $[(H_2O)_nH^+] = f_n \sum_n [(H_2O)_nH^+]$ where f_n is a constant depending only on experimental conditions. The distribution of relative $(H_2O)_nH^+$ intensities depends only on $[H_2O]$.

If sample molecules A are present in the proton transfer tube, the equilibrium condition also exists for reactions $(H_2O)_{n-1}AH^+ + H_2O \rightleftarrows (H_2O)_nAH^+$. Similarly to the case of with the protonated H_2O clusters, we can write $[(H_2O)_nAH^+] = p_n \sum_n [(H_2O)_nAH^+]$, where p_n is also a constant depending on experimental conditions.

If we consider proton transfer reaction:

$$(H_2O)_nH^+ + A \rightleftarrows (H_2O)_{n-1}AH^+ + H_2O. \qquad (26)$$

we arrive at the following steady state $(H_2O)_{n-1}AH^+$

$$\frac{d[(H_2O)_{n-1}AH^+]}{dt} = 0 = k_{4\_n}[(H_2O)_nH^+][A] - \frac{k_{4\_n}}{K_n}[H_2O][(H_2O)_{n-1}AH^+] - \frac{D_{(H_2O)_{n-1}AH^+}}{<r^2>}[(H_2O)_{n-1}AH^+]$$
$$- \frac{F}{V}[(H_2O)_{n-1}AH^+] + PR([(H_2O)_{n-1}AH^+]) - DR([(H_2O)_{n-1}AH^+]) \quad (27)$$

Here, k_{4_n} is the forward reaction rate coefficient of the above reaction, $k_{4\_n} \approx 2\times10^{-9}\,\mathrm{cm^3/s}$ at room temperature; K_n is the equilibrium constant; the ratio $\frac{k_{4\_n}}{K_n}$ is the reverse reaction rate coefficient; $PR([(H_2O)_{n-1}AH^+])$ and $DR([(H_2O)_{n-1}AH^+]$ are $(H_2O)_{n-1}AH^+$ production rate and consumption rate in the reaction $(H_2O)_{n-1}AH^+ + H_2O \rightleftarrows (H_2O)_nAH^+$. They are related as follows:

$$\sum_n PR([(H_2O)_{n-1}AH^+]) = \sum_n DR([(H_2O)_{n-1}AH^+]) \quad (28)$$

Since all molecules are much larger than N_2, the diffusion coefficients for all ions are about same, = $D_{A\,ion}$. Combining all these equations together, gives the following result:

$$\frac{\sum_n[(H_2O)_nAH^+]}{[A]} = \sum_n \frac{k_{4\_n}[(H_2O)_nH^+]}{\frac{k_{4\_n}}{K_{4\_n}}[H_2O] + \frac{D_{A\,ion}}{<r^2>} + \frac{F}{V}} \quad (29)$$

From table (1), we see that all molecules that we are interested in have fairly large values of K_2 and K_3 which correspond to $(H_2O)_3H^+$ and $(H_2O)_4H^+$ proton transfer reactions. That means $\frac{k_{4\_n}}{K_{4\_n}}[H_2O] << \frac{D_{A\,ion}}{<r^2>} + \frac{F}{V}$. Eq. (29) can be simplified as follows:

$$\frac{\sum_n[A(H_2O)_nH^+]}{[A]} \approx \sum_n \frac{k_{4\_n}[H^+(H_2O)_n]}{\frac{D_{A\,ion}}{<r^2>} + \frac{F}{V}}$$
$$= \sum_n \left(\frac{k_{4\_n}}{\frac{D_{A\,ion}}{<r^2>} + \frac{F}{V}} \times f_n \sum_n [H^+(H_2O)_n]\right) = F \times \sum_n [H^+(H_2O)_n] \quad (30)$$

Here,

$$F = \sum_n \left(\frac{k_{4\_n}}{\frac{D_{A\ ion}}{< r^2 >} + \frac{F}{V}} \times f_n\right) \quad \text{So} \quad \frac{\sum_n [A(H_2O)_n H^+]}{\sum_n [H^+(H_2O)_n]} \approx F \times [A] \tag{31}$$

The main conclusion from equation (31) is that the ratio between the total analyte ion concentration and the total H_2O ion concentration should be directly proportional to the analyte concentration, even if clustering reactions are present. This equation forms the basis of the quantitative analysis with this AP-CIMS. The sensitivity depends on constant F, which in turn depends on the diffusion coefficient of ions derived from A and the reaction rate of reaction between $(H_2O)_n H^+$ and A.

6.6.2.3 Proton transfer reaction including A cluster formation in the ionizer

Finally, we have to consider the scenario involving significant dimer formation in reaction $A + AH^+ \rightleftarrows A_2H^+$. Using a similar approach, we can write:

$$\frac{d[AH^+]}{dt} = 0 = k_4[(H_2O)H^+][A] + \frac{k_d}{K_d}[A_2H^+] - k_d[AH^+][A] - \frac{k_4}{K_4}[H_2O][AH^+] - \frac{D_{HA^+}}{< r^2 >}[AH^+] - \frac{F}{V}[AH^+] \tag{32}$$

$$\frac{d[(H_2O)H^+]}{dt} = 0 = S - k_4[(H_2O)H^+][A] + \frac{k_4}{K_4}[H_2O][AH^+] - \frac{D_{(H_2O)H^+}}{< r^2 >}[(H_2O)H^+] - \frac{F}{V}[(H_2O)H^+] \tag{33}$$

$$\frac{d[A_2H^+]}{dt} = 0 = k_d[AH^+][A] - \frac{k_d}{K_d}[A_2H^+] - \frac{D_{A_2H^+}}{< r^2 >}[A_2H^+] - \frac{F}{V}[A_2H^+] \tag{34}$$

From all equations above,

$$\frac{[A_2H^+]}{[A]} = \frac{k_d[AH^+]}{\frac{k_d}{K_d} + \frac{D_{A_2H^+}}{< r^2 >} + \frac{F}{V}} = \frac{k_d[AH^+]}{b} \tag{35}$$

where $b = \frac{k_d}{K_d} + \frac{D_{A_2H^+}}{< r^2 >} + \frac{F}{V}$, a constant for a given set of experimental conditions.

Suppose $a=\frac{k_1}{K_1}[H_2O]+\frac{D_{HA^+}}{<r^2>}+\frac{F}{V}$

$$[HA^+]=\frac{k_1[H^+(H_2O)][A]+\frac{k_2}{K_2}[H^+A_2]}{k_2[A]+\frac{k_1}{K_1}[H_2O]+\frac{D_{HA^+}}{<r^2>}+\frac{F}{V}}=\frac{k_1[H^+(H_2O)][A]+\frac{k_2}{K_2}[H^+A_2]}{k_2[A]+a} \qquad (36)$$

So we can get

$$\frac{[HA^+]}{[A]}=\frac{k_1[H^+(H_2O)]}{k_2[A](1-\frac{k_2}{K_2b})+a} \qquad (37)$$

$$\frac{[HA^+]+[HA_2^+]}{[A]}=\frac{k_1[H^+(H_2O)]}{k_2[A](1-\frac{k_2}{K_2b})+a}(1+\frac{k_2}{b}[A])=\frac{k_1[H^+(H_2O)]}{\frac{k_2[A]}{b}(b-\frac{k_2}{K_2})+a}(1+\frac{k_2}{b}[A]) \qquad (38)$$

When the diffusion coefficients are close to each other, then $b-\frac{k_2}{K_2}\approx a$.

$$\frac{[HA^+]+[HA_2^+]}{[A]}=\frac{k_1[H^+(H_2O)]}{\frac{k_2[A]}{b}a+a}(1+\frac{k_2}{b}[A])\approx\frac{k_1[H^+(H_2O)]}{a} \qquad (39)$$

The result can be extended to A cluster ions.

$$\frac{\sum_n[(H_2O)_nAH^+]+\sum_n[(H_2O)_nA_2H^+]}{[A]}\approx\frac{\sum_n k_{4\_n}f_n}{a}\sum_n[H^+(H_2O)_n] \qquad (40)$$

This result demonstrates that when A forms dimers, the ratio of the total A signal including the monomeric and dimeric ions, normalized to the total H_2O ion signal, is directly proportional to [A].

When sample molecule A has low proton affinity, the assumption $\frac{k_{4\_n}}{K_{4\_n}}[H_2O]<<\frac{D_{A\ ion}}{<r^2>}+\frac{F}{V}$ no longer holds. In this case, the sensitivity drops significantly, and it strongly depends on $[H_2O]$.

6.6.3 Instrument calibration in the two-inlet mode

The calibration setup was similar with the one used for the one-inlet AP-CIMS calibration.

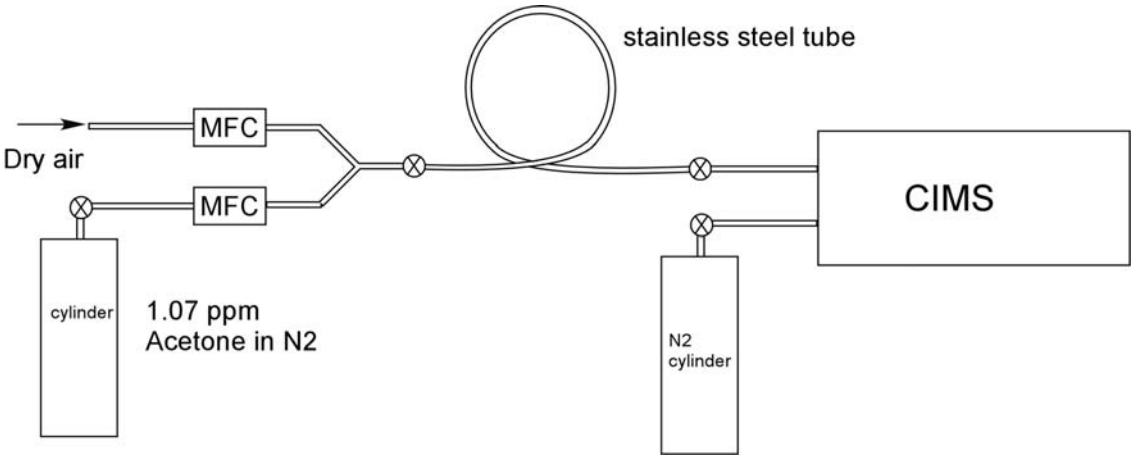

Figure 6.12 Calibration experiment setup

The 1.07 ppm ^{13}acetone cylinder and dry air were exactly same as the ones in the calibration experiment for the one-inlet AP-CIMS. Acetone/N_2 mixed with dry air in a long 1/2" stainless steel tube first. Then the mixed flow went into the sample line. The acetone flow rate ranged from 2 sccm to 100 sccm and the dry air flow ranged from 5 L/min to 20 L/min. The N_2/H_2O reagent flow was set to be 20 sccm, a setting that have the highest $H^+(H_2O)_n$ signal. All flows were controlled by calibrated mass flow controllers.

Observed peaks were the same as the ones shown in section 6.5.3, but the relative peak heights were different. The result of acetone ion concentration/acetone concentration ratio is shown in Fig. 6.13. The x axis is the acetone mixing ratio in ppb; y axis is the sum of all acetone ions including monomeric and dimeric ones.

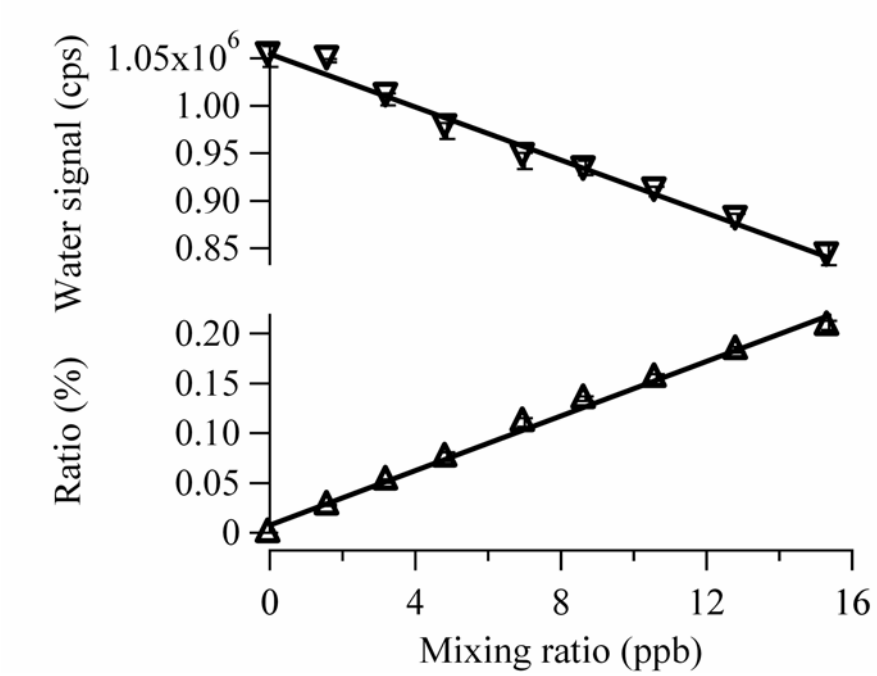

Figure 6.13 Total acetone signal and water signal change with acetone concentration

The linearity from this calibration experiment is close to what is predicted in the theoretical kinetic calculation. Below 6 ppb, the degree of linearity is deemed acceptable.

6.6.4 Comparative summary of the one-inlet and two-inlet configurations

Both one-inlet and two-inlet configurations are based on proton transfer reaction between H_2O ions and sample molecules. The H_2O ion production mechanism is same in the two systems. But that does not necessary mean that they work in exactly same way.

The kinetic simulations of the one-inlet system showed that the linearity is limited by the dimer formation. The sensitivity of the one-inlet AP-CIMS depends on the rate constants for the proton transfer reactions and recombination rate constants of reaction between cluster ions of A and thermal electrons.

In the two-inlet AP-CIMS, the situation is somewhat different because the

positive and negative ion concentrations in the proton-transfer region are no longer balanced. Dimer formation does not strongly affect the linearity. Sensitivity and linearity depend on the proton transfer reaction rates and also on diffusion coefficients of A cluster ions. The sensitivity is somewhat lower in the two-inlet configuration because more possibilities for the loss of ions exist.

The main advantage of the two-inlet design is that the pinhole clogging problems plaguing the one-inlet design could be avoided. The proton transfer tube in the two-inlet configuration could be heated to high temperature without having to worry about damage the ^{63}Ni source. When the proton transfer region was heated to 200°C, the ^{63}Ni source was below 45°C. This is very helpful when the system is used in the thermal desorption aerosol mass spectrometer mode.

One more important benefit of the two-inlet design is that it helps avoid N_2^+ attacking sample molecules directly. Ionization of sample molecules by N_2^+ leads to serious fragmentation in the one-inlet system, which limits its usefulness.

References

1. Hinds, W.C., *Aerosol Technology*. 1999, New York: John Wiley & Sons.
2. Baron, P.A. and K. Willeke, *Aerosol measurement*. 2001: John Wiley and Sons, Inc.
3. Finlayson-Pitts, B.J. and J.N. Pitts, *Chemistry of the Upper and Lower Atmosphere: Theory, Experiments, and Applications*. 2000: Academic Press. 1040 pp.
4. Seinfeld, J.H., Pandis S. N., *atmospheric chemistry and physics*. 1998.
5. Penner, J.E., R.E. Dickinson, and C.A. Oneill, *Effects of Aerosol from Biomass Burning on the Global Radiation Budget.* Science, 1992. **256**(5062): p. 1432-1434.
6. Lohmann, U. and J. Feichter, *Global indirect aerosol effects: a review.* Atmospheric Chemistry and Physics, 2005. **5**: p. 715-737.
7. Twomey, S., *Influence of Pollution on Shortwave Albedo of Clouds.* Journal of the Atmospheric Sciences, 1977. **34**(7): p. 1149-1152.
8. Albrecht, B.A., *Aerosols, Cloud Microphysics, and Fractional Cloudiness.* Science, 1989. **245**(4923): p. 1227-1230.
9. Charlson, R.J., et al., *Climate Forcing by Anthropogenic Aerosols.* Science, 1992. **255**(5043): p. 423-430.
10. Dockery, D.W., et al., *An Association between Air-Pollution and Mortality in 6 United-States Cities.* New England Journal of Medicine, 1993. **329**(24): p. 1753-1759.
11. Katsouyanni, K., et al., *Short term effects of ambient sulphur dioxide and particulate matter on mortality in 12 European cities: Results from time series data from the APHEA project.* British Medical Journal, 1997. **314**(7095): p. 1658-1663.
12. Samet, J.M., et al., *Fine particulate air pollution and mortality in 20 US Cities, 1987-1994.* New England Journal of Medicine, 2000. **343**(24): p. 1742-1749.
13. Pope, C.A., et al., *Lung cancer, cardiopulmonary mortality, and long-term exposure to fine particulate air pollution.* Jama-Journal of the American Medical Association, 2002. **287**(9): p. 1132-1141.
14. Davidson, C.I., R.F. Phalen, and P.A. Solomon, *Airborne particulate matter and human health: A review.* Aerosol Science and Technology, 2005. **39**(8): p. 737-749.
15. Oberdorster, G., *Pulmonary effects of inhaled ultrafine particles.* International Archives of Occupational and Environmental Health, 2001. **74**(1): p. 1-8.
16. Oberdorster, G., et al., *Translocation of inhaled ultrafine particles to the brain.* Inhalation Toxicology, 2004. **16**(6-7): p. 437-445.
17. Roberts, G.C., et al., *Sensitivity of CCN spectra on chemical and physical properties of aerosol: A case study from the Amazon Basin.* Journal of Geophysical Research-Atmospheres, 2002. **107**(D20).
18. Andreae, M.O. and P.J. Crutzen, *Atmospheric aerosols: Biogeochemical sources and role in atmospheric chemistry.* Science, 1997. **276**(5315): p. 1052-1058.
19. Lamb, B., et al., *A National Inventory of Biogenic Hydrocarbon Emissions.* Atmospheric Environment, 1987. **21**(8): p. 1695-1705.

20. Guenther, A., et al., *A Global-Model of Natural Volatile Organic-Compound Emissions.* Journal of Geophysical Research-Atmospheres, 1995. **100**(D5): p. 8873-8892.
21. Muller, J.F., *Geographical-Distribution and Seasonal-Variation of Surface Emissions and Deposition Velocities of Atmospheric Trace Gases.* Journal of Geophysical Research-Atmospheres, 1992. **97**(D4): p. 3787-3804.
22. Guenther, A., P. Zimmerman, and M. Wildermuth, *Natural Volatile Organic-Compound Emission Rate Estimates for United-States Woodland Landscapes.* Atmospheric Environment, 1994. **28**(6): p. 1197-1210.
23. Guenther, A., et al., *Natural emissions of non-methane volatile organic compounds; carbon monoxide, and oxides of nitrogen from North America.* Atmospheric Environment, 2000. **34**(12-14): p. 2205-2230.
24. Ellison, G.B., A.F. Tuck, and V. Vaida, *Atmospheric processing of organic aerosols.* Journal of Geophysical Research-Atmospheres, 1999. **104**(D9): p. 11633-11641.
25. Rudich, Y., *Laboratory perspectives on the chemical transformations of organic matter in atmospheric particles.* Chemical Reviews, 2003. **103**(12): p. 5097-5124.
26. Rudich, Y., N.M. Donahue, and T.F. Mentel, *Aging of organic aerosol: Bridging the gap between laboratory and field studies.* Annual Review of Physical Chemistry, 2007. **58**: p. 321-352.
27. Walser, M.L., et al., *Photochemical aging of secondary organic aerosol particles generated from the oxidation of d-limonene.* Journal of Physical Chemistry A, 2007. **111**(10): p. 1907-1913.
28. Robinson, A.L., et al., *Rethinking organic aerosols: Semivolatile emissions and photochemical aging.* Science, 2007. **315**(5816): p. 1259-1262.
29. VanReken, T.M., et al., *Cloud condensation nucleus activation properties of biogenic secondary organic aerosol.* Journal of Geophysical Research-Atmospheres, 2005. **110**(D7).
30. Geron, C., et al., *A review and synthesis of monoterpene speciation from forests in the United States.* Atmospheric Environment, 2000. **34**(11): p. 1761-1781.
31. Andersson-Skold, Y. and D. Simpson, *Secondary organic aerosol formation in northern Europe: A model study.* Journal of Geophysical Research-Atmospheres, 2001. **106**(D7): p. 7357-7374.
32. Arey, J., et al., *Hydrocarbon Emissions from Natural Vegetation in California South-Coast-Air-Basin.* Atmospheric Environment, 1995. **29**(21): p. 2977-2988.
33. Guenther, A., et al., *Leaf, branch, stand and landscape scale measurements of volatile organic compound fluxes from US woodlands.* Tree Physiology, 1996. **16**(1-2): p. 17-24.
34. Tingey, D.T., et al., *Influence of Light and Temperature on Monoterpene Emission Rates from Slash Pine.* Plant Physiology, 1980. **65**(5): p. 797-801.
35. Guenther, A.B., R.K. Monson, and R. Fall, *Isoprene and Monoterpene Emission Rate Variability - Observations with Eucalyptus and Emission Rate Algorithm Development.* Journal of Geophysical Research-Atmospheres, 1991. **96**(D6): p. 10799-10808.
36. Yokouchi, Y. and Y. Ambe, *Factors Affecting the Emission of Monoterpenes from Red Pine (Pinus-Densiflora).* Plant Physiology, 1984. **75**(4): p. 1009-1012.

37. Staudt, M., et al., *Seasonal and diurnal patterns of monoterpene emissions from Pinus pinea (L.) under field conditions.* Atmospheric Environment, 1997. **31**: p. 145-156.
38. Kesselmeier, J. and M. Staudt, *Biogenic volatile organic compounds (VOC): An overview on emission, physiology and ecology.* Journal of Atmospheric Chemistry, 1999. **33**(1): p. 23-88.
39. Went, F.W., *Blue Hazes in the Atmosphere.* Nature, 1960. **187**(4738): p. 641-643.
40. Atkinson, R. and J. Arey, *Gas-phase tropospheric chemistry of biogenic volatile organic compounds: a review.* Atmospheric Environment, 2003. **37**: p. S197-S219.
41. Calogirou, A., B.R. Larsen, and D. Kotzias, *Gas-phase terpene oxidation products: a review.* Atmospheric Environment, 1999. **33**(9): p. 1423-1439.
42. Criegee, R. and G. Wenner, **Die Ozonisierung Des 9,10-Oktalins.* Annalen Der Chemie-Justus Liebig, 1949. **564**(1): p. 9-15.
43. Hoffmann, T., et al., *Formation of organic aerosols from the oxidation of biogenic hydrocarbons.* Journal of Atmospheric Chemistry, 1997. **26**(2): p. 189-222.
44. Lee, A., et al., *Gas-phase products and secondary aerosol yields from the ozonolysis of ten different terpenes.* Journal of Geophysical Research-Atmospheres, 2006. **111**(D7).
45. Jonsson, S.M., M. Hallquist, and E. Ljungstroem, *Impact of Humidity on the Ozone Initiated Oxidation of Limonene, D3-Carene, and a-Pinene.* Environmental Science and Technology, 2006. **40**(1): p. 188-194.
46. Presto, A.A., K.E.H. Hartz, and N.M. Donahue, *Secondary organic aerosol production from terpene ozonolysis. 1. Effect of UV radiation.* Environmental Science & Technology, 2005. **39**(18): p. 7036-7045.
47. Pathak, R.K., et al., *Ozonolysis of alpha-pinene at atmospherically relevant concentrations: Temperature dependence of aerosol mass fractions (yields).* Journal of Geophysical Research-Atmospheres, 2007. **112**(D3).
48. Northcross, A.L. and M. Jang, *Heterogeneous SOA yield from ozonolysis of monoterpenes in the presence of inorganic acid.* Atmospheric Environment, 2007. **41**(7): p. 1483-1493.
49. Donahue, N.M., et al., *Critical factors determining the variation in SOA yields from terpene ozonolysis: A combined experimental and computational study.* Faraday Discussions, 2005. **130**: p. 295-309.
50. Claeys, M., et al., *Formation of secondary organic aerosols through photooxidation of isoprene.* Science, 2004. **303**(5661): p. 1173-1176.
51. Zhang, J., et al., *Secondary Organic Aerosol Formation from Limonene Ozonolysis: Homogeneous and Heterogeneous Influences as a Function of NOx* Journal of Physical Chemistry A, 2006. **110**(38): p. 11053-11063.
52. Mang, S.A., et al., *Contribution of carbonyl photochemistry to aging of atmospheric secondary organic aerosol.* Journal of Physical Chemistry A, 2008. **112**(36): p. 8337-8344.
53. Wolkoff, P., et al., *Formation of strong airway irritants in terpene/ozone mixtures.* Indoor Air, 2000. **10**(2): p. 82-91.
54. He, C.R., F. Murray, and T. Lyons, *Monoterpene and isoprene emissions from 15 Eucalyptus species in Australia.* Atmospheric Environment, 2000. **34**(4): p.

645-655.
55. Spittler, M., et al., *Reactions of NO3 radicals with limonene and alpha-pinene: Product and SOA formation.* Atmospheric Environment, 2006. **40**: p. S116-S127.
56. Kanakidou, M., et al., *Organic aerosol and global climate modelling: a review.* Atmospheric Chemistry and Physics, 2005. **5**: p. 1053-1123.
57. Griffin, R.J., et al., *Estimate of global atmospheric organic aerosol from oxidation of biogenic hydrocarbons.* Geophysical Research Letters, 1999. **26**(17): p. 2721-2724.
58. Weschler, C.J., H.C. Shields, and D.V. Naik, *Indoor Ozone Exposures.* Japca-the Journal of the Air & Waste Management Association, 1989. **39**(12): p. 1562-1568.
59. Nazaroff, W.W. and C.J. Weschler, *Cleaning products and air fresheners: exposure to primary and secondary air pollutants.* Atmospheric Environment, 2004. **38**(18): p. 2841-2865.
60. Singer, B.C., et al., *Cleaning products and air fresheners: emissions and resulting concentrations of glycol ethers and terpenoids.* Indoor Air, 2006. **16**(3): p. 179-191.
61. Sexton, K., et al., *Comparison of personal, indoor, and outdoor exposures to hazardous air pollutants in three urban communities.* Environmental Science & Technology, 2004. **38**(2): p. 423-430.
62. Wolkoff, P., et al., *Acute airway effects of ozone-initiated d-limonene chemistry: Importance of gaseous products.* Toxicology Letters, 2008. **181**(3): p. 171-176.
63. Haag, J.D., M.J. Lindstrom, and M.N. Gould, *Limonene-Induced Regression of Mammary Carcinomas.* Cancer Research, 1992. **52**(14): p. 4021-4026.
64. Shu, Y.G. and R. Atkinson, *Rate Constants for the Gas-Phase Reactions of O-3 with a Series of Terpenes and Oh Radical Formation from the O-3 Reactions with Sesquiterpenes at 296+/-2-K.* International Journal of Chemical Kinetics, 1994. **26**(12): p. 1193-1205.
65. Bailey, P.S., *Ozonation of organic chemistry*. Organic chemistry, ed. A.T. Blomquist and H.H. Wasserman. Vol. 39. 1978: Academic Press.
66. Khamaganov, V.G. and R.A. Hites, *Rate constants for the gas-phase reactions of ozone with isoprene, alpha- and beta-pinene, and limonene as a function of temperature.* Journal of Physical Chemistry A, 2001. **105**(5): p. 815-822.
67. Leungsakul, S., M. Jaoui, and R.M. Kamens, *Kinetic mechanism for predicting secondary organic aerosol formation from the reaction of d-limonene with ozone.* Environmental Science & Technology, 2005. **39**(24): p. 9583-9594.
68. Leungsakul, S., H.E. Jeffries, and R.M. Kamens, *A kinetic mechanism for predicting secondary aerosol formation from the reactions of d-limonene in the presence of oxides of nitrogen and natural sunlight.* Atmospheric Environment, 2005. **39**(37): p. 7063-7082.
69. Hewitt, C.N. and G.L. Kok, *Formation and occurrence of organic hydroperoxides in the troposphere: laboratory and field observations.* Journal of Atmospheric Chemistry, 1991. **12**(2): p. 181-94.
70. Grosjean, D., et al., *Atmospheric oxidation of biogenic hydrocarbons: reaction of ozone with b-pinene, D-limonene and trans-caryophyllene.* Environmental Science and Technology, 1993. **27**(13): p. 2754-8.
71. Hakola, H., et al., *Product Formation from the Gas-Phase Reactions of Oh*

Radicals and O3 with a Series of Monoterpenes. Journal of Atmospheric Chemistry, 1994. **18**(1): p. 75-102.
72. Feltham, E.J., et al., *Reactions of alkenes with ozone in the gas phase: a matrix-isolation study of secondary ozonides and carbonyl-containing reaction products.* Spectrochimica Acta, Part A: Molecular and Biomolecular Spectroscopy, 2000. **56A**(13): p. 2605-2616.
73. Glasius, M., et al., *Carboxylic acids in secondary aerosols from oxidation of cyclic monoterpenes by ozone.* Environmental Science & Technology, 2000. **34**(6): p. 1001-1010.
74. Koch, S., et al., *Formation of new particles in the gas-phase ozonolysis of monoterpenes.* Atmospheric Environment, 2000. **34**(23): p. 4031-4042.
75. Norgaard, A.W., et al., *Secondary limonene endo-ozonide: A major product from gas-phase ozonolysis of R-(+)-limonene at ambient temperature.* Atmospheric Environment, 2006. **40**(19): p. 3460-3466.
76. Heaton, K.J., et al., *Oligomers in the early stage of biogenic secondary organic aerosol formation and growth.* Environmental Science & Technology, 2007. **41**(17): p. 6129-6136.
77. Iinuma, Y., et al., *The formation of organic sulfate esters in the limonene ozonolysis secondary organic aerosol (SOA) under acidic conditions.* Atmospheric Environment, 2007. **41**(27): p. 5571-5583.
78. Walser, M.L., et al., *High-resolution mass spectrometric analysis of secondary organic aerosol produced by ozonation of limonene.* Physical Chemistry Chemical Physics, 2008. **10**(7): p. 1009-1022.
79. Hallquist, M., et al., *Aerosol and product yields from NO3 radical-initiated oxidation of selected monoterpenes.* Environmental Science & Technology, 1999. **33**(4): p. 553-559.
80. Harrision, A.G., *Chemical ionization mass spectrometry*. 1992, Boston: CRC Press.
81. Hearn, J.D. and G.D. Smith, *Reactions and mass spectra of complex particles using Aerosol CIMS.* International Journal of Mass Spectrometry, 2006. **258**(1-3): p. 95-103.
82. Donahue, N.M., et al., *Secondary organic aerosol from limona ketone: insights into terpene ozonolysis via synthesis of key intermediates.* Physical Chemistry Chemical Physics, 2007. **9**(23): p. 2991-2998.
83. Johnson, D. and G. Marston, *The gas-phase ozonolysis of unsaturated volatile organic compounds in the troposphere.* Chemical Society Reviews, 2008. **37**(4): p. 699-716.
84. Li, Q.F., et al., *Large outdoor chamber experiments and computer simulations: (I) Secondary organic aerosol formation from the oxidation of a mixture of d-limonene and alpha-pinene.* Atmospheric Environment, 2007. **41**(40): p. 9341-9352.
85. Nizkorodov, S.A., et al., *Temperature dependent kinetics of the OH/HO2/O3 chain reaction by time-resolved IR laser absorption spectroscopy.* Journal of Physical Chemistry A, 2000. **104**(17): p. 3964-3973.
86. Tolocka, M.P., et al., *Chemistry of particle inception and growth during alpha-pinene ozonolysis.* Environmental Science & Technology, 2006. **40**(6): p.

1843-1848.
87. Ng, N.L., et al., *Contribution of First- versus Second-Generation Products to Secondary Organic Aerosols Formed in the Oxidation of Biogenic Hydrocarbons.* Environmental Science & Technology, 2006. **40**(7): p. 2283-2297.
88. Gomez, A.L., et al., *UV photodissociation spectroscopy of oxidized undecylenic acid films.* Journal of Physical Chemistry A, 2006. **110**(10): p. 3584-3592.
89. Presto, A.A. and N.M. Donahue, *Investigation of alpha-pinene plus ozone secondary organic aerosol formation at low total aerosol mass.* Environmental Science & Technology, 2006. **40**(11): p. 3536-3543.
90. Shilling, J.E., et al., *Particle mass yield in secondary organic aerosol formed by the dark ozonolysis of alpha-pinene.* Atmospheric Chemistry and Physics, 2008. **8**(7): p. 2073-2088.
91. Pathak, R.K., et al., *Ozonolysis of alpha-pinene: parameterization of secondary organic aerosol mass fraction.* Atmospheric Chemistry and Physics, 2007. **7**(14): p. 3811-3821.
92. Donahue, N.M., et al., *Competitive oxidation in atmospheric aerosols: The case for relative kinetics.* Geophysical Research Letters, 2005. **32**(16).
93. Jaoui, M., et al., *Analysis of secondary organic aerosol compounds from the photooxidation of d-limonene in the presence of NOX and their detection in ambient PM2.5.* Environmental Science & Technology, 2006. **40**(12): p. 3819-3828.
94. Yu, Y., et al., *Photooxidation of alpha-pinene at high relative humidity in the presence of increasing concentrations of NOx.* Atmospheric Environment, 2008. **42**(20): p. 5044-5060.
95. Martinez, E., et al., *Kinetics of the reactions of NO3 radical with selected monoterpenes: A temperature dependence study.* Environmental Science & Technology, 1998. **32**(23): p. 3730-3734.
96. Wayne, R.P., et al., *The Nitrate Radical - Physics, Chemistry, and the Atmosphere.* Atmospheric Environment Part a-General Topics, 1991. **25**(1): p. 1-203.
97. Atkinson, R., *Atmospheric chemistry of VOCs and NOx.* Atmospheric Environment, 2000. **34**(12-14): p. 2063-2101.
98. Gross, S. and A.K. Bertram, *Products and kinetics of the reactions of an alkane monolayer and a terminal alkene monolayer with NO3 radicals.* Journal of Geophysical Research-Atmospheres, 2009. **114**.
99. Roberts, J.M., *The Atmospheric Chemistry of Organic Nitrates.* Atmospheric Environment Part a-General Topics, 1990. **24**(2): p. 243-287.
100. Atkinson, R., et al., *Evaluated kinetic and photochemical data for atmospheric chemistry, organic species: Supplement VII.* Journal of Physical and Chemical Reference Data, 1999. **28**(2): p. 191-393.
101. Davis, R., *Mass Spectrometry*. 1987.
102. Munson, M.S.B. and F.H. Field, *Chemical Ionization Mass Spectrometry .I. General Introduction.* Journal of the American Chemical Society, 1966. **88**(12): p. 2621-&.
103. Carroll, D.I., et al., *Subpicogram Detection System for Gas-Phase Analysis Based Upon Atmospheric-Pressure Ionization (Api) Mass-Spectrometry.* Analytical Chemistry, 1974. **46**(6): p. 706-710.

104. Horning, E.C., et al., *New Picogram Detection System Based on a Mass-Spectrometer with an External Ionization Source at Atmospheric-Pressure.* Analytical Chemistry, 1973. **45**(6): p. 936-943.
105. Lias, S.G., et al., *Gas-Phase Ion and Neutral Thermochemistry.* Journal of Physical and Chemical Reference Data, 1988. **17**: p. 1-861.
106. Gray, D.E., *AIP Handbook*. 1972, New York: McGraw-Hill. 296.
107. Carr, T.W., *Plasma Chromatography* 1984: Plenum Pub Corp.
108. Good, A., D.A. Durden, and P. Kebarle, *Ion-molecule reactions in pure nitrogen and nitrogen containing traces of water at total pressures 0.5-4 torr. kinetics of clustering reactions forming H+(H2O)n.* Journal of Chemical Physics, 1970. **52**(1): p. 212-21.
109. Good, A., D.A. Durden, and P. Kebarle, *Mechanism and rate constants of ion-molecule reactions leading to formation of H+(H2O)n in moist oxygen and air.* Journal of Chemical Physics, 1970. **52**(1): p. 222-9.
110. Moseley, J.T., et al., *Mobilities Diffusion Coefficients and Reaction Rates of Mass-Indentified Nitrogen Ions in Nitrogen.* Physical Review, 1969. **178**(1): p. 240-&.
111. Siegel, M.W. and W.L. Fite, *Terminal Ions in Weak Atmospheric-Pressure Plasmas - Applications of Atmospheric-Pressure Ionization to Trace Impurity Analysis in Gases.* Journal of Physical Chemistry, 1976. **80**(26): p. 2871-2881.
112. Siegel, M.W. and M.C. McKeown, *Ions and Electrons in Electron-Capture Detector - Quantitative Identification by Atmospheric-Pressure Ionization Mass-Spectrometry.* Journal of Chromatography, 1976. **122**(JUL7): p. 397-413.
113. Aleksandrov, N.L., et al., *Plasma decay in N-2, CO2 and H2O excited by high-voltage nanosecond discharge.* Journal of Physics D-Applied Physics, 2007. **40**(15): p. 4493-4502.
114. Johnsen, R., *Electron-Temperature Dependence of the Recombination of H3o+(H2o)N Ions with Electrons.* Journal of Chemical Physics, 1993. **98**(7): p. 5390-5395.
115. McDaniel, E.W. and E.A. Mason, *The mobility and diffusion of ions in gases*. Wiley series in plasma physics. 1972: John wiley & Sons.
116. Miller, T.M., et al., *Reactions of H+ in H2 and D+ in D2 - Mobilities of Hydrogen and Alkali Ions in H2 and D2 Gases.* Physical Review, 1968. **173**(1): p. 115-&.
117. Meot-Ner, M., *The ionic hydrogen bond.* Chemical Reviews, 2005. **105**(1): p. 213-284.
118. Dzidic, I., et al., *Comparison of Positive-Ions Formed in Nickel-63 and Corona Discharge Ion Sources Using Nitrogen, Argon, Isobutane, Ammonia and Nitric-Oxide as Reagents in Atmospheric-Pressure Ionization Mass-Spectrometry.* Analytical Chemistry, 1976. **48**(12): p. 1763-1768.
119. Eiceman, G. and K. Z., *Ion mobility spectrometry*. 2005.